POLITECNICO DI TORINO

Master's Degree in Aerospace Engineering

Master's Degree Thesis

SIMULATIONS OF CONVECTIVE PHENOMENA WITH THE LIMITED AREA VERSION OF THE ICON PREDICTION MODEL AND COMPARISON WITH WEATHER RADAR OBSERVATIONS

Supervisors

Prof.ssa Daniela TORDELLA

Dott. Roberto CREMONINI

Dott.ssa Virginia POLI

Dott.ssa Valeria GARBERO

Dott. Alessio GOLZIO

Candidate

Riccardo NEGRO

July 2025

Abstract

The aim of this thesis is to evaluate the performance of the regional version of the numerical weather prediction model ICON in simulating severe convective storms. Observations from weather radars, complemented by radio soundings and ground weather stations, provide the target for the performance evaluation. The motivation for this analysis stems from the difficulties encountered by high-resolution weather forecast models in detecting convective cells, especially those producing severe thunderstorms, which prevents the timely issue of weather warnings to the public. The supercell thunderstorm that occurred over central Piedmont in the afternoon hours of 6 July 2023 has been selected as case study. Four forecasts of this event were considered, each one differing by the combination of microphysical parameterisation scheme and assimilation technique used. The first run mimics the operational settings implementing a bulk-moment microphysics scheme and no assimilation; the second one adopts a double-moment microphysics scheme without assimilation, while the third and fourth experimental sets run the Latent heat Nudging (LHN) data assimilation on a bulk and double-moment scheme, respectively.

Table of Contents

Acronyms

NWP Numerical Weather Prediction

CAPPI Constant Altitude Plane Position Indicator

PPI Plane Position Indicator

CAPE Convective Available Potential Energy

CIN Convective Inhibition

MUCAPE Most Unstable CAPE

MUCIN Most Unstable CIN

SBCAPE Surface Based CAPE

SBCIN Surface Based CIN

MLCAPE Mixed Layer CAPE

MLCIN Mixed Layer CIN

LAM Limited Area Model

BC Boundary Conditions

LFC Level of Free Convection

LCL Lifting Condensation Level

ML Mixed Layer

EL Equilibrium Level

SCP Supercell Composite Parameter

CCN Cloud Condensation Nuclei

FFD Forward Flank Downdraft

RFD Rearward Flank Downdraft

WER Weak Echo Region

BWER Bounded Weak Echo Region

eSCP effective Supercell Composite Parameter

ICON ICOsahedral Nonhydrostatic

DWD Deutscher WetterDienst

MPI-M Max Planck Institute for Meteorology

DKRZ Deutsches KlimaRechenZentrum

KIT Karlsruhe Institute of Technology

LES Large Eddie Simulation

Arpae Agenzia Regonale Protezione Ambiente Energia Emilia-Romagna

ARPA Regional Environmental Protection Agency

SLEVE Smooth LEvel VErtical

HPC High Performance Computing

EnVar Hybrid Ensemble Variational

LETKF Localised Ensemble Transform Kalman Filter

KENDA Kilometre ENsemble Data Assimilation

LHN Latent heat Nudging

PSD Particle Size Distribution

MCS Mesoscale Convective Systems

IC1M ICON Single-Moment

IC1M-LHN ICON Single-Moment with LHN

IC2M ICON Double-Moment

IC2M-LHN ICON Double-Moment with LHN

CINECA Consorzio Interuniversitario del Nord-Est per il Calcolo Automatico

SLE Cuneo-Levaldigi Airport

LIMN Cameri Airport

SPC San Pietro Capofiume

SRH Storm Relative Helicity

ESRH Effective Storm Relative Helicity

EBWD Effective Bulk Wind Difference

EM Electro Magnetic

Z_H Horizontal Reflectivity

Z_V Vertical Reflectivity

Z_{DR} Differential Reflectivity

ρ_{hv} Cross Correlation Coefficient

Φ_{DP} Total Differential Phase

K_{DP} Specific Differential Phase

δ Backscatter Differential Phase

LDR Linear Depolarisation Ratio

CDR Circular Depolarisation Ratio

$A_{h,v}$ Specific Attenuation

A_{DP} Specific Differential Attenuation

RHI Range-Height Indicator

S Scattering Matrix

Z Equivalent Reflectivity Factor

FSS Fraction Skill Score

NO-NO NeighbOurhood-NeighbOurhood

MSE Mean Squared Error

RMSE Root Mean Squared Error

PID Particle IDentification

MBF MemBership Function

EMVORADO Efficient Modular VOlume scan RADar Operator

PBL Planetary Boundary Layer

ASL Above Sea Level

DGR Dendritic Growth Regime

DPC Italian Civil Protection Department

Chapter 1

Introduction

The 6th of July 2023 a violent thunderstorm hit the provinces of Torino, Asti and Cuneo in Piedmont, a region located in the northeast of Italy, with intense hailfalls, strong wind gusts and flash floods that brought several damages to infrastructures and agricolture. Due to climate changes, such destructive phenomena are becoming more and more frequent and destructive. Estimates by [1] and [2] attribute to severe convective storms more than $10 billion USD of damages in the United States, with a likewise estimate for global losses, each year. With the aim of better predicting these events, research activity is being conducted to improve numerical weather prediction models, which is a challenging endeavour due to the extremely varying spatial and temporal scales that characterize the spectrum of weather phenomena, ranging from hurricanes and fronts to mesoscale circulations down to the smallest scales of turbulence and microphysical processes. The direct numerical simulation of the full atmosphere is prohibitive because, even with state-of-the-art High Performance Computing (HPC), the computing time and the memory storage required are excessively high for operational needs, which

urge the forecast to be released in the shortest possible time. Reduction of the grid resolution while adopting parametrisation schemes to describe sub-grid processes, as function of large scale variables, is the only feasible option to produce weather forecasts. The downside of reducing the grid resolution is represented by a loss of informations on the small scales, which inevitably affect the larger ones and rapidly lead to a deterioration of results and to model biases [3]. The choice of the horizontal grid resolution requires a trade-off between the objectives of the weather simulation and the computing costs. To simulate the entire atmosphere, current global models employ spatial resolutions on the order of tens of kilometers, which necessitate a full parameterization of convection, turbulence and microphysical processes. To simulate meso-γ[1] meteorological systems such as the thunderstorm here investigated, the horizontal spatial grid must be refined to achieve kilometer-scale resolution, where deep-convection usually takes place [4]. Eventually, the computing domain can be clipped to include only the selected area of interest and reduce the computational burden, as done by regional Numerical Weather Prediction (NWP) models. Horizontal grids at this resolution are considered convective-permitting, since they capture deep, but not shallow, convection types. This grid resolution range is often referred to as the Grey Zone, to remark the lack of a full description of atmospheric convection processes. Among others, the choice of the paramtrization scheme adopted to describe microphysical processes occurring inside the cloud is one of the aspects to be faced by

[1]Mesoscale meteorological systems are divided into three main classes according to size: meso-α scale: 200-2000 km including fronts, squall lines and Mesoscale Convective Systems (MCS); meso-β scale: 20-200 km for mesocyclones, sea breezes and lake effect snow; meso-γ scale: 2-20 km for thunderstorm convection and complex terrain flows

the NWP models. Despite involving processes occurring up to micron-sized scales they have great impact on the global energy budget and on the water cycle. These processes are, indeed, characterized by inherent physical and dynamical nonlinearities, with multiple and simultaneous interacting paths between bi-phase substances which make their accurate characterization difficult. Among the various parametrisation approaches developed in order to simulate microphysics processes, bulk-moment schemes are, to date, the most adopted thanks to the low computing power they require. They describe the evolution of hydrometeors inside the cloud environment in terms of bulk quantities related to the hydrometeors such as their total mass and/or total number density rather than considering each particle as a separate entity in function of its size, as it's done by spectral schemes. Bulk microphysics schemes are termed after the number of bulk quantities predicted such that a single-moment scheme predicts only one bulk property, whereas a double-moment scheme predicts two.

The present thesis follows a previous work on the Weather Research and Forecasting (WRF) model and it aims at analyzing a deep-convection event that the operative limited area model was not able to correctly predict at that time. The simulations, performed on the Consorzio Interuniversitario del Nord-Est per il Calcolo Automatico (CINECA)'s Galileo100 supercomputer, located at Bologna Technopolo, Bologna (Italy), consider the state-of-the art ICOsahedral Nonhydrostatic (ICON)-Limited Area Model (LAM), here tested on different configurations with a focus on microphysics and assimilation aspects.

Due to unavailability of the ensemble members, operatively adopted in the assimilation phase to produce boundary conditions, a first attempt is made to seize the model's ability in triggering deep-convection without any

assimilation cycle, uniquely relying on the atmospheric estimate produced by the ICON-EU model, having a 6.5 km grid resolution nest over Europe. Impact on the choice of the bulk microphysics parametrisation scheme is also evaluated in this case. Later, a LHN assimilation technique, specifically developed to deal with high-resolution models, is regularly applied as an external forcing to the model by exploiting the potentialities of the weather radar in estimating the rainfall intensity with great spatial and temporal resolution. Again, the performances of the two microphysics scheme are evaluated. The model results are verified against observations of the event obtained from various sources distributed in northern Italy. These include radiounsounding stations, located at Cuneo-Levaldigi Airport (SLE), Cameri Airport (LIMN) and San Pietro Capofiume (SPC), ground weather stations, belonging to the Regional Environmental Protection Agency (ARPA) Piemonte network, and Monte Settepani and Bric della Croce weather radars, located in Piedmont, Italy.

1.1 Case study

The case study selected is represented by the supercell thunderstorm that occurred in Piedmont, a region in northwestern Italy, during the afternoon of 6 July 2023. This meteorological event was selected because of the severity of the hazards produced, including damaging large hail, locally heavy rainfall rates, and strong wind gusts. This section provides a synoptic overview of the event, integrated with data from radio soundings, weather radars and images taken by observers on the ground.

On 6 July 2023, Italy was under the edge of the African Ridge from the south, which brought high pressure, and a deep cyclonic circulation with a

minimum of 500 hPa halfway between Iceland and the British Isles. A jet streak resulting from the interaction of these two structures established itself over Piedmont, leading to strong currents aloft as shown in Fig. 1.1a and an intensification of the vorticity.

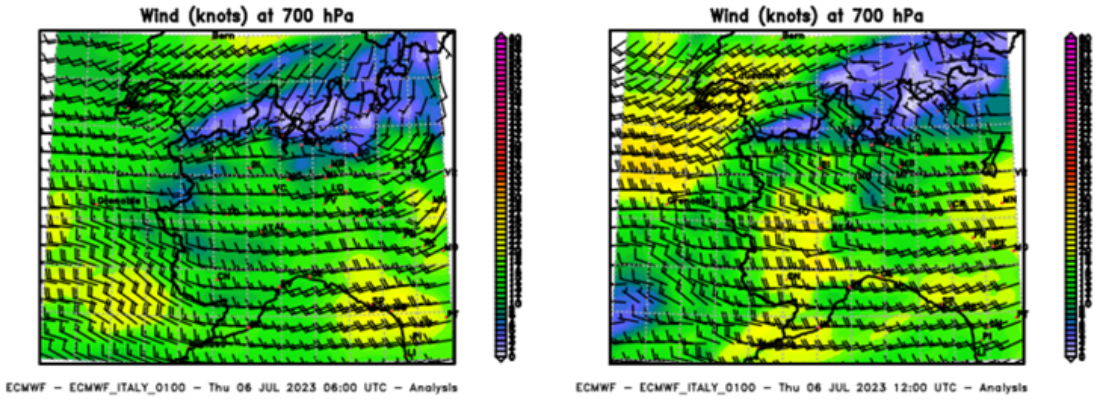

(a) Analysis produced by the ECMWF - IFS model at 06 UTC (left) and at 12 UTC (right) on July 06 2023 showing the vector field of horizontal wind at 700 hPa. ARPA Piemonte processing on ECMWF data.

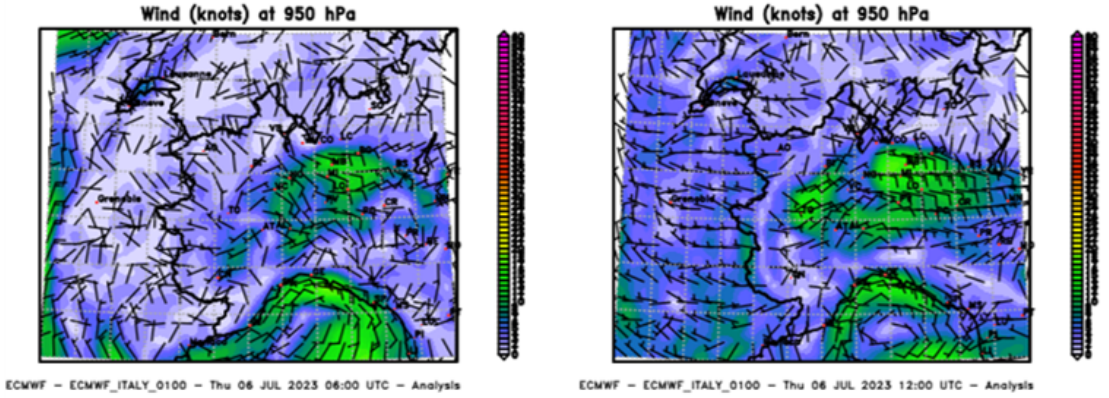

(b) Analysis produced by the ECMWF - IFS model at 06 UTC (left) and at 12 UTC (right) on July 06 2023 showing the vector field of horizontal wind at 950 hPa. ARPA Piemonte processing on ECMWF data.

Intense solar heating throughout the morning and afternoon hours allowed for the accumulation of large amounts of energy, in the form of heat stored in the atmospheric layers close to the surface, described physically by the Convective Available Potential Energy (CAPE), which is

discussed in details in section 2.2.2. Indeed, a peak value of 2994 J/kg was recorded by the Cuneo Levaldigi radiosounding station at 1200 UTC shown in Fig. 1.2. This suggests a highly unstable atmosphere, with the potential for intense convective activity.

In the lower atmospheric layers, a weak pressure minimum over the Ligurian Sea created a north-northeasterly circulation over Piedmont, conveyed in Fig. 1.1b, facilitating the orographic lifting of air masses over the foothills of the Southern Cottian and Maritime Alps, where cumulus clouds began to form and moved rapidly eastwards due to the strong clockwise wind shear with height.

In the central hours, a convective cell formed near Pinerolo and moved towards the sectors south of Turin, from where it continued to move towards southwest, taking on the characteristics of a supercell. The path of the supercell was of interest to the provinces of Turin, Asti and Cuneo, where an intensification of thunderstorm activity was observed. It began to dissipate at the border with the Liguria region and ended its course in the province of Savona. Its evolution, recorded by both Bric della Croce and Monte Settepani weather radars, is conveyed in Fig. 1.3, with a red circle to track the position over time.

It can be seen that the cell, which formed at 1045 UTC to the South of Turin, intensified over the next 40 – 50 minutes while moving South-East and reached Alba at 1245 UTC. It then moved southwest towards the Ligurian border, dissipating around 1430 UTC. The track of the supercell affected only a specific set of the uniformly distributed ARPA Piemonte's ground weather stations on the Piedmont region. For a clear description of the spatial distribution of the ground weather stations considered in this analysis the reader is directed to section 2.2.1.

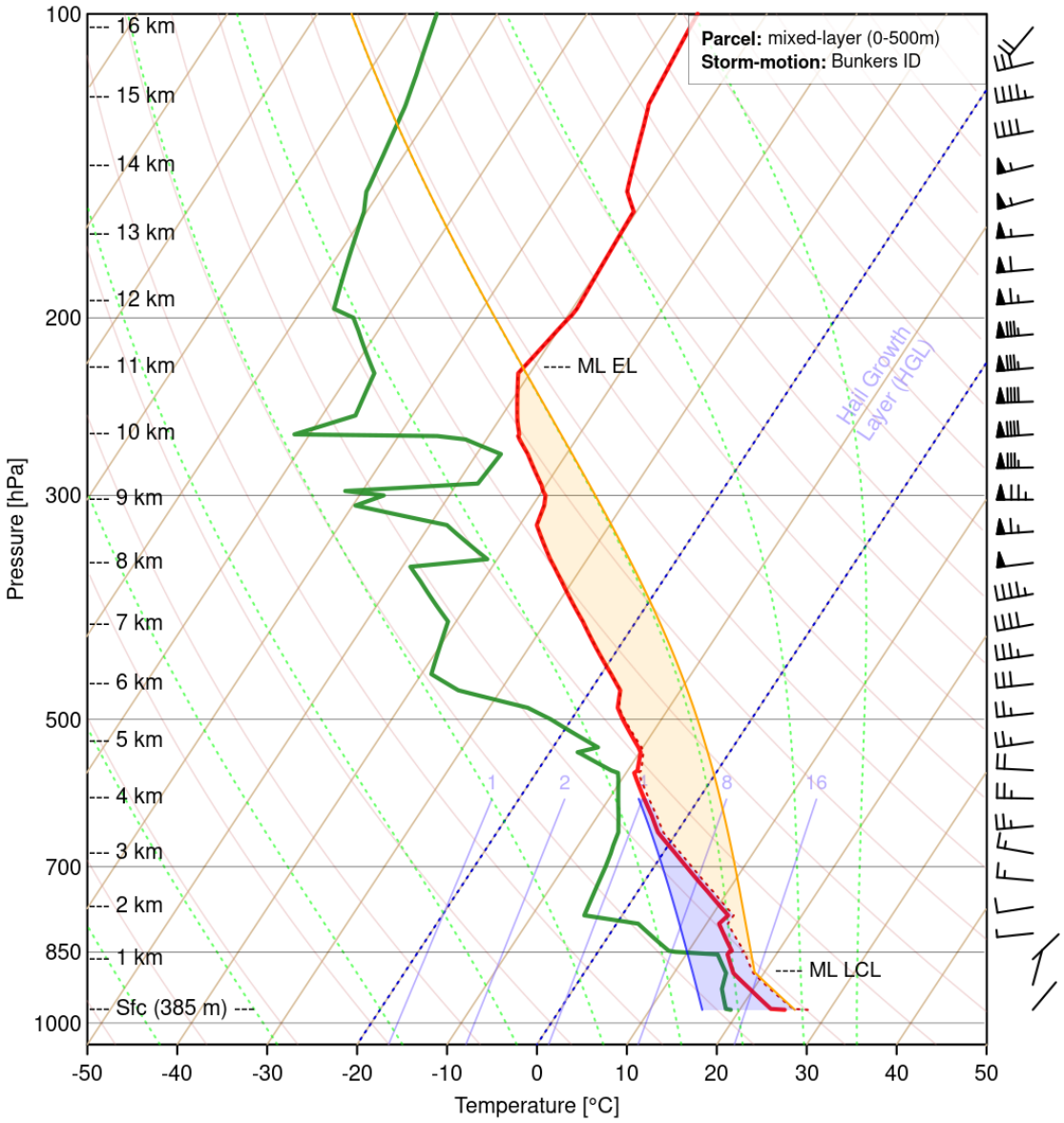

Figure 1.2: Vertical air (red curve), dew point (green curve) and mixed-layer lifted air parcel (orange curve) temperature profiles obtained from the Cuneo-Levaldigi (ARPA Piemonte, 385 m ASL) radiosounding station at 1200 UTC. The orange-shaded area represents the CAPE whereas the blue-shaded area represents the Convective Inhibition (CIN). On the right of the plot, wind barbs show wind direction and speed. Lifting Condensation Level (LCL) and Equilibrium Level (EL) are computed for the Mixed Layer (ML). Source: Thunder Rawinsonde package, $https://rawinsonde.com/thunder_app/$

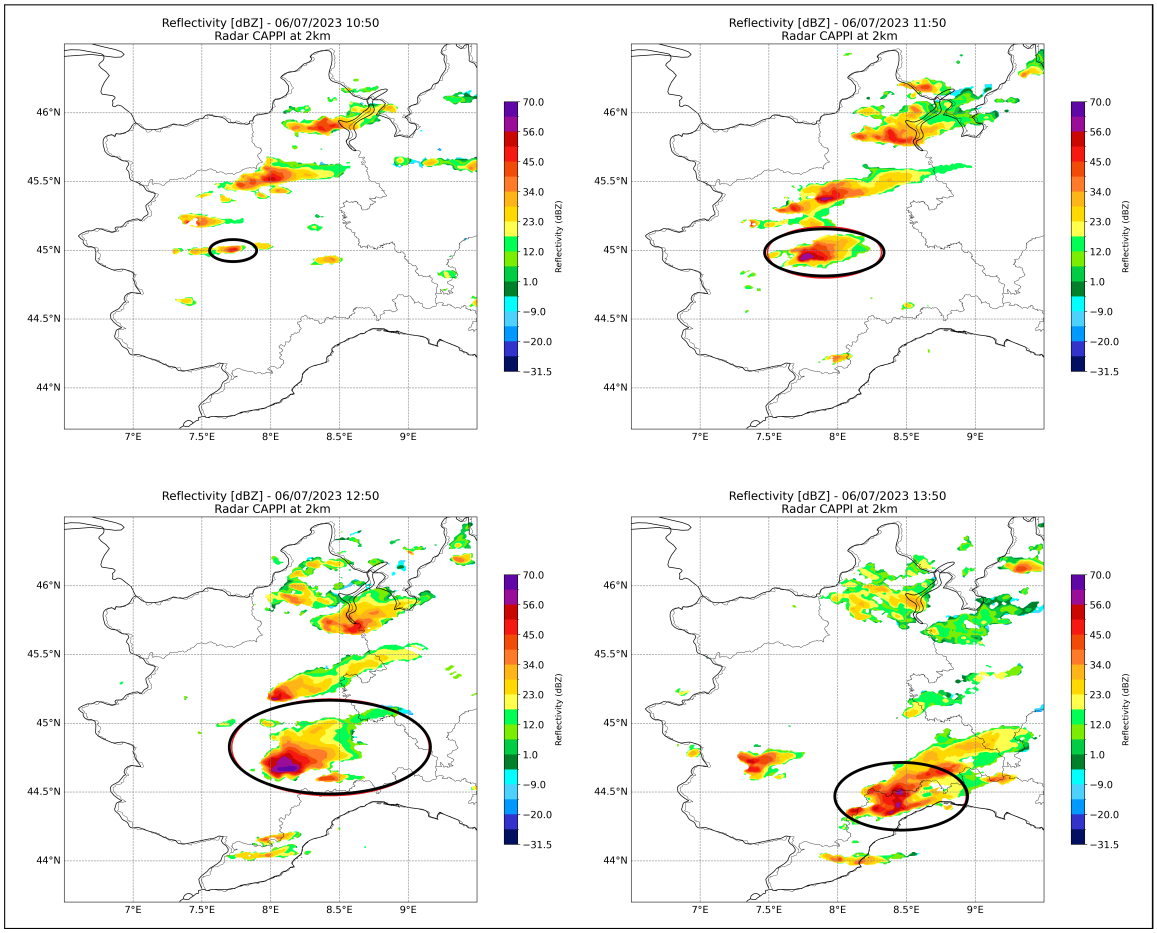

Figure 1.3: Radar composite maps of equivalent reflectivity factor obtained from Monte Settepani and Bric della Croce weather radars. The location of the supercell under investigation is highlighted with a red circle. Growing cumulus, mature and dissipation stages are captured in temporal sequence with instantaneous records at (a) 1050 UTC, (b) 1150 UTC, (c) 1250 UTC and (d) 1350 UTC.

Values of precipitation reached peaks of 40 mm cumulated over one hour in Cortemilia, where floodings occurred as documented by the picture in Fig. 1.4.

Figure 1.4: Flooding of a street in Cortemilia provoked by the supercell passage at 1256 UTC. Image sourced from the Telegram group "Dati Meteo Asti"

High wind gusts were also recorded by several ground stations managed by ARPA Piemonte, the most intense of which hit the Alba Tanaro and Baldissero stations with values of 76 km/h and 63 km/h, uprooting trees that fell on the streets.

The worst damage, however, was caused by the hailstorm which produced large hailstones up to 6 cm in diameter as reported in Fig. 1.5, hitting

vineyards and cornfields in the Langhe area and causing massive agriculture losses documented by the pictures shot after the supercell passage in Fig. 1.6.

Figure 1.5: Hailstones of 6 cm in diameter collected 1300 UTC in Perletto, Piedmont. Source: ESSL database https://eswd.eu/cgi-bin/eswd.cgi

Figure 1.6: Intense damages to cornfields (left) in the Uzzone valley, Piedmont (Italy) and vineyards (right) in the city of Guarene, Piedmont (Italy) documented the day after the supercell passage. Image sourced from the Telegram group "Dati Meteo Asti"

1.2 Supercells and microphysics

A thunderstorm is defined as a convective cloud often extending from the top of the planetary boundary layer up to the tropopause [5]. Atmospheric convection develops in the presence of thermodynamical instability, high moisture in the lower atmospheric layers, and a trigger. Vertical wind shear is responsible for the further organisation of the storm. Assuming that a trigger is present and the air is moist, the intensity of vertical wind shear and atmospheric instability characterize deep convection phenomena, allowing for their initial classification. Low levels of wind shear and instability give rise to single-cell storms, also known as pulse storms because of their pulsed behaviour. They arise from a convective updraft, usually promoted by weak vertical forcing, followed by a co-located, precipitation-laden, downdraft of cold air that promptly suppresses it. This process occurs within a lifetime of about 30 to 60 minutes.

Weak to moderate vertical wind shear acts to move the core of the

downdraft away from that of the updraft, reducing the likelihood of storm suppression and making the cell longer-lived. As the cold air of the downdraft (cold pool) reaches the surface, it spreads out, forcing any warm and moist boundary layer air to rise and condense to form a newborn cell. This mechanism produces a multicellular structure consisting of many individual cells at different stages of their life, each moving with the mean steering wind, although the overall storm propagation is at an angle to the respective mean wind direction. Both single-cell and multi-cell structures can originate from warm air blown towards a mountain slope in a process called orographic lifting. This mechanism is active in the formation of thunderstorms in the Po Valley, which is surrounded by the Alps.

1.2.1 Supercell

In the presence of strong wind shear and high atmospheric instability a convective cell organises itself to produce the most severe type of existing thunderstorm, the supercell. Strong wind shear is responsible for the generation of a horizontal vorticity tube in the lower layers of the atmosphere which, under the influence of the updraft, is tilted and stretched into the vertical, creating a pair of counter-rotating vortices called mesocyclones. These structures induce a vertical pressure gradient force, independent of their direction of rotation, with the result that the flanks of the original updraft intensify in strength. In such updrafts, the buoyancy of moist air is so strong that there is little time for the hydrometeors to grow significantly in size. This feature appears in the reflectivity cross section obtained from a vertical radar scan of the supercell as a Bounded Weak Echo Region (BWER), as conceptually schematised in Fig. 1.7. Intense vertical wind shear is also responsible for moving the downdraft

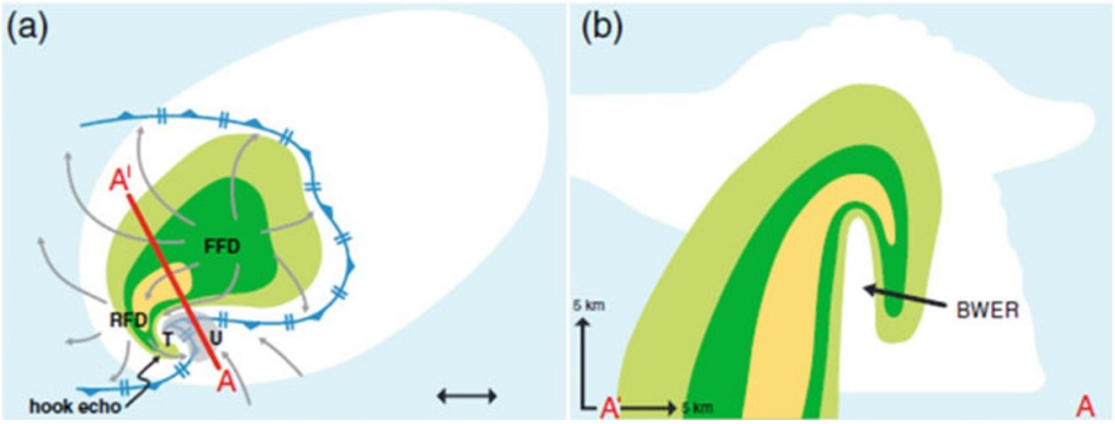

Figure 1.7: Conceptual drawing of the reflectivity field of a supercell tornadic storm. (a) View from above, (b) vertical cross-section along transect A'A. Source: Ryzhkov, Alexander V., and Dušan S. Zrnić. Radar polarimetry for weather observations. Vol. 486. Cham, Switzerland: Springer International Publishing, 2019.

away from the updraft core, reducing their interaction and promoting a persistent circulation pattern, generally lasting hours. These two factors ultimately favour the formation of large hailstones, which account for a large portion of the observed precipitation products of a supercell.

In the early stages of supercell development, as precipitation begins to form in response to the lifting and condensation of moist air in the updraft, the associated downdraft splits the vortex tube in half, creating a pair of new updrafts to the sides of the original one [6]. This process is represented in Fig. 1.8.

In response to the direction of propagation of the new updrafts, to the right and left of the mean wind, a left- and right-moving supercell are observed, respectively. Depending on the type of vertical wind shear, that could manifest in terms of speed or direction, one or two separate supercells may develop from the split. When vertical wind shear involves only changes in wind speed with height (without changes in direction), it generates a

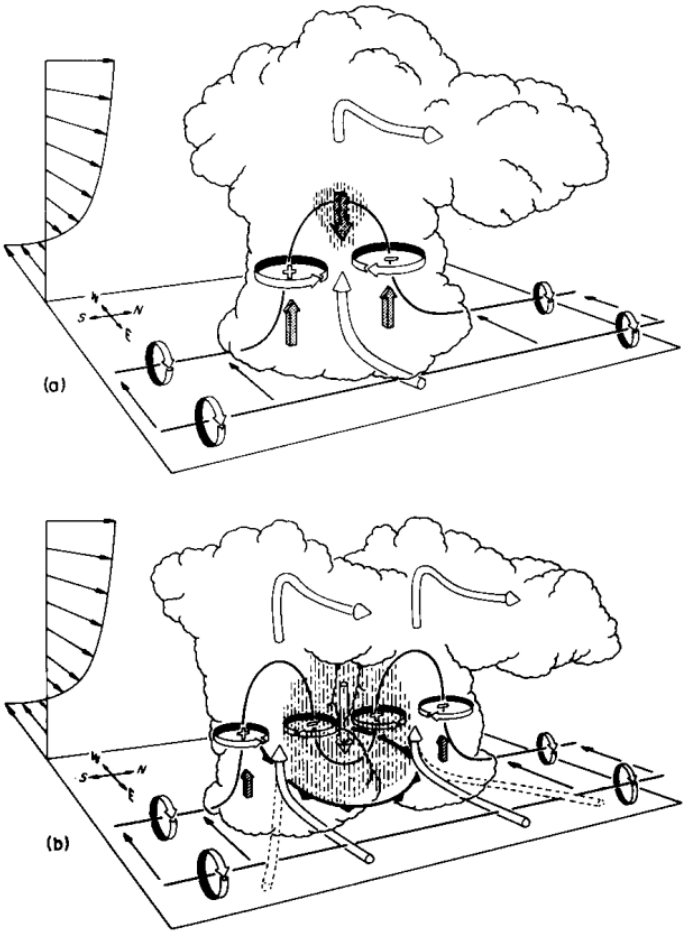

Figure 1.8: Stages in the formation of a supercell thunderstorm within a westerly mean sheared environment, indicated with storm relative wind arrows in the upper left of the images. Solid black lines represents vortex tubes, with circular arrows giving a sense of rotation, positive for cyclonical and negative for anticyclonical. Thick black shaded arrows represent storm's updrafts and downdrafts. Cylindrical arrows show the diresction of cloud relative air flow. Dashed lines represent precipitation. (a) Initial stage of supercell development, consisting of the tilting and stretching of horizontal vorticity tubes into the vertical and formation of precipitation aloft. (b) Splitting stage of the supercell development, with formation of a downdraft in between the new updraft cells. Source: Holton, James R., and Gregory J. Hakim. An introduction to dynamic meteorology. Vol. 88. Academic press, 2013.

pressure field that supports the development of both right-moving and left-moving supercells. However, if the wind shear also includes a directional component, the pressure field favors only one type of supercell, either right- or left-moving, while quickly suppressing the other. In the Northern Hemisphere, the directional shear more commonly involves veering winds, which turn clockwise with height, rather than backing winds turning counterclockwise. As a result, right-moving supercells tend to dominate, while left-moving ones are less frequent.

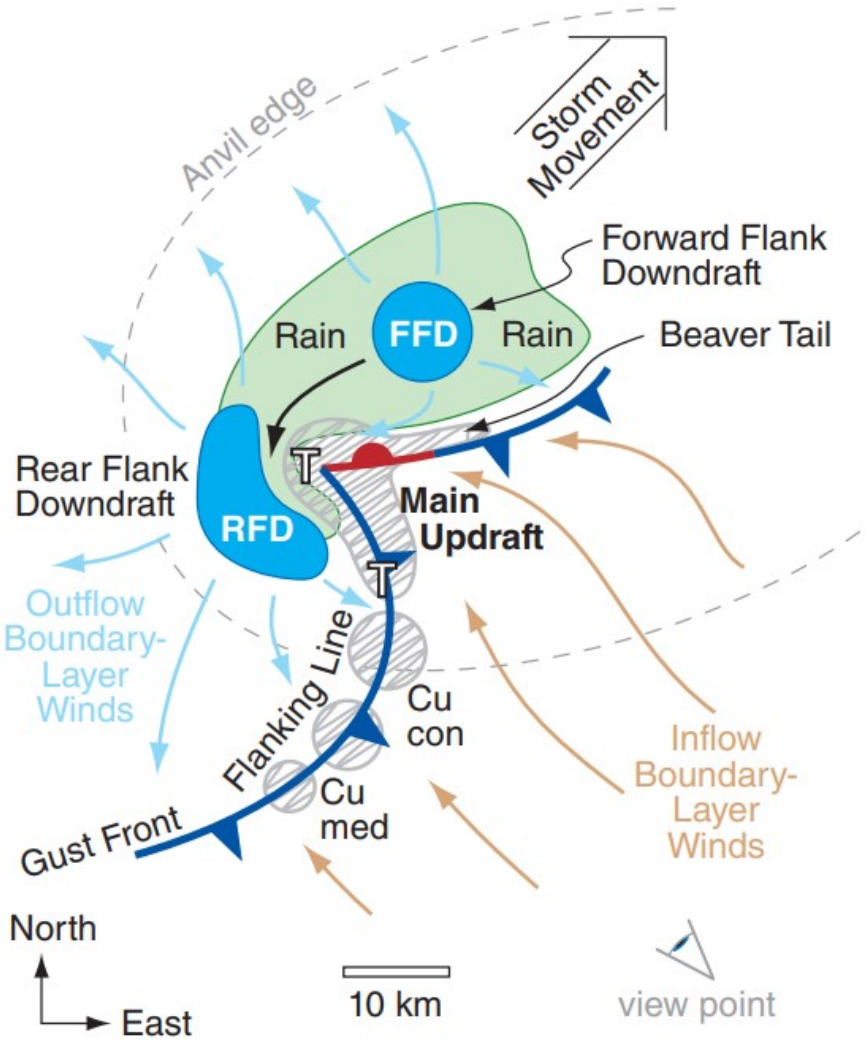

Figure 1.9: Conceptual drawing of a supercell tornadic storm. Source: Stull, Ronald B. Practical meteorology: an algebra-based survey of atmospheric science. University of British Columbia, 2015.

In such thunderstorms, precipitation is associated with two distinct downdraft regions, shown in Fig. 1.9. The main downdraft, namely the Forward Flank Downdraft (FFD), located downwind of the supercell updraft as its name suggests, carries the largest amounts of precipitation, inhomogeneously distributed in space due to the effects of an intense size

sorting. Moving from the proximity of the supercell's core to farther distances in the direction of the mean wind, hail and large raindrops are first encountered, followed by graupel and lighter raindrops until the precipitation eventually disappears.
As the rotating currents of the mesocyclone drag the FFD along, a second downdraft region is observed. From the radar echo signal, this downdraft appears in the shape of a hook surrounding the upwind side of the mesocyclone, in what is called Rearward Flank Downdraft (RFD). As the RFD descends towards the ground and cools by evaporation, its density and speed increase, creating a cold gust front at the ground capable of triggering convection near the main updraft in what is observed as a line of *cumulus* clouds, called the flanking line, which grows in size towards the updraft that later engulfs them, providing a continuous source of fuel for the thunderstorm. If the FFD completely surrounds the mesocyclone, an occluded front will form, cutting off the supply of warm air from below. This would cause a sudden intensification of the supercell before it dies. Eventually, the supercell dissipates as warm and moist air is no longer available.

1.2.2 Microphysics of supercells

Supercells are responsible for the majority of large hail events by providing the ideal conditions for their formation. A hailstone is defined as any regular or irregular piece of ice falling from a thunderstorm and exceeding a maximum diameter of 5 mm on any axis. The width of the supercell's updraft is thought to provide both a larger area for injection of hail embryos, which form the nucleus for further hailstone growth, and

a larger volume through which hail trajectories can pass, increasing the hail's growth potential. In addition, the rotating nature of the mesocyclone provides the necessary time for the slow growth of hydrometeors by curving their trajectories, and the necessary updraft strength to keep heavy hydrometeors from falling to the ground. This is particularly beneficial for the formation of large hailstones, which require considerable time, usually 10-15 minutes, in the growth region of the thunderstorm.

Another necessary ingredient for the production of large hail is an abundance of supercooled liquid water, which is found mainly in the temperature ranges between $-10°C$ and $-25°C$. Here, the majority of hail growth occurs [7]. During hail growth, the surface of the hailstone is heated and cooled as a result of thermodynamical processes. Heat is added during riming (Q_L) and is released via conduction (Q_v) and sublimation (Q_s). Two hail growth regimes have been defined by microphisicists depending on the equilibrium point, the liquid water content available for growth, the ambient temperature and the size of the hailstone. The dry regime is the slowest and occurs when both the ambient and hailstone surface temperatures are below freezing. The wet regime, on the other hand, is responsible for the rapid growth of hailstones. Wet growth is active in the case of extreme riming, which requires an abundance of supercooled liquid droplets, in very intense convective updrafts, such as those of a supercell. A hailstone is said to be in the wet growth regime when its surface reaches an equilibrium temperature either equal to or above $0°C$. The condition for wet growth to occur requires that the heating and cooling processes on the surface of a hailstone find their equilibrium point when the surface

temperature $T_s = 0°C$.

$$\frac{dQ_L}{dt} = \frac{dQv}{dt} + \frac{dQs}{dt}, \quad T_s = 0 \tag{1.1}$$

This condition, known as the Schuman-Ludlam threshold for wet growth, is met when the heating rates exceed the cooling rates in order to raise the surface temperature above the ambient temperature. This is only achieved for sufficiently large hail. In fact, heating and cooling rates show different dependencies on hailstone diameter; as it increases, cooling rates increase more slowly than heating rates and wet growth can occur. In this regime, a film of liquid water covers the surface, altering the hail growth characteristics by increasing the efficiency in the collection of frozen droplets.

Fig. 1.10 displays a typical supercell's vertical cross section oriented along the direction of storm propagation.

1.2.3 Polarimetric characteristics of supercells

When hydrometeors (e.g., raindrops, graupel, hail, ice crystals) inside a thunderstorm are illuminated by the Electro Magnetic (EM) wave produced by a polarimetric weather radar, whose working principle is described in Section 2.2.3, they produce a backscattered signal which is affected by the microphysical processes underway such as melting, evaporation or shedding to cite a few. For this reason, weather radars technology is implemented to analyse the morphology and composition of thunderstorms. Since the backscattered signal possesses specific energy, amplitude and phase, multiple informations, in the form of polarimetric variables (listed in Section 2.2.3), can be retrieved. The measure of the backscattered

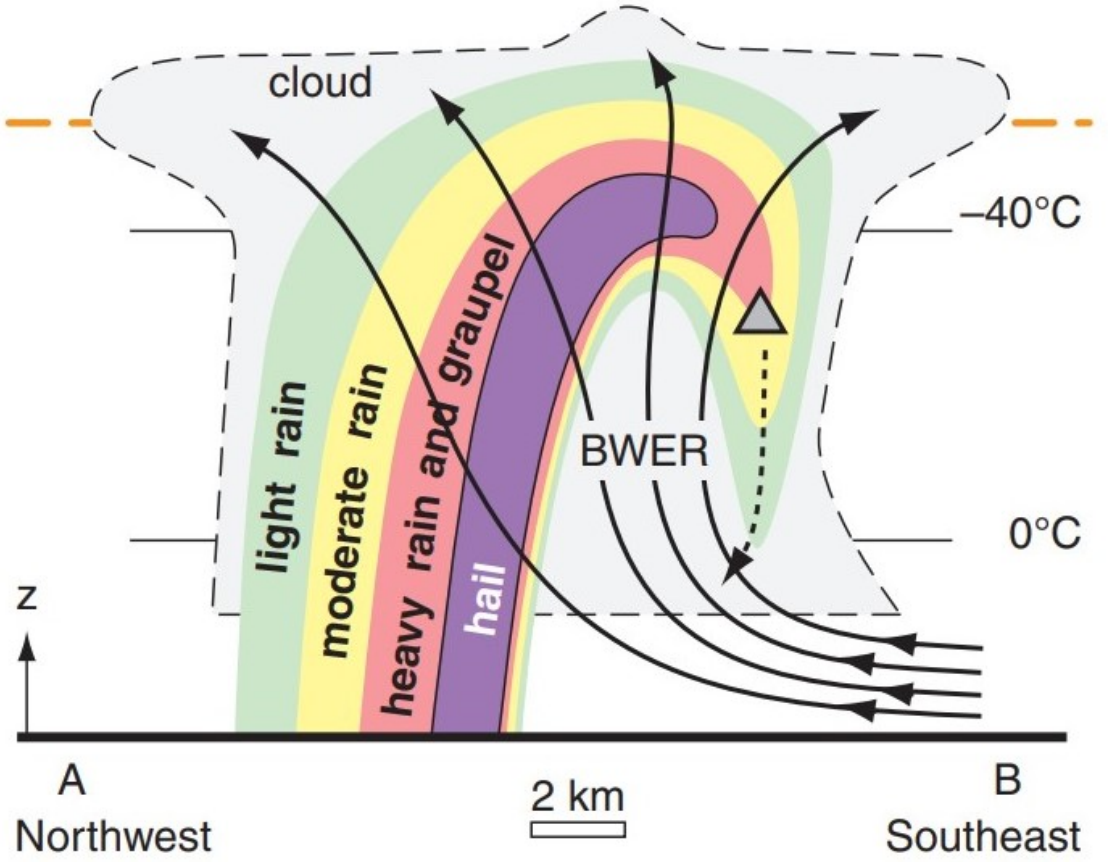

Figure 1.10: Conceptual drawing of the vertical cross-section of a classic supercell. The grey shaded area represents the visible extension of the cloud, whereas the precipitation region is coloured as function of the precipitation type. The BWER is indicated with. Black lines represent streamlines of the updraft (going up) and of the recirculating path of the graupel (hail embryos) particles belonging to the embryo curtain. Isotherms of 0°C and -40°C are drawn, as well as a reference line (in orange) to mark the height of the tropopause. Source: Stull, Ronald B. Practical meteorology: an algebra-based survey of atmospheric science. University of British Columbia, 2015.

energy as function of the emitted signal defines the reflectivity factor, to which are associated several features of thunderstorms and, in the specific of supercells hereafter described.

Hook echo signature

In the horizontal reflectivity field of a supercell at low layers, associated with the RFD feature, an hook echo signature is often observed separating the inflow from the downdraft region, located on the storm-relative northern flank of the mesocyclone, wrapping around it while advecting precipitation. The hook echo pattern manifests with moderate-to-high reflectivity values.

Weak Echo Region (WER)

A defining characteristic of supercells is the updraft-induced reflectivity feature known as the *vault*. This structure arises from the interplay between intense updraft speeds and the delayed development of microphysical processes. As updraft velocities intensify, rapid vertical ascent creates an adiabatic, particle-depleted zone where insufficient residence time prevents proper droplet growth and ice nucleation. These intense updrafts, which are characteristic of supercellular environments, are extremely inefficient in terms of hail production, with only a small proportion of the liquid water content in the column effectively converted into hail. At the same time, however, the abundance of small supercooled liquid water droplets stored in the updraft column creates the perfect conditions for the preferential formation of large hailstones. Radar imagery captures this phenomenon as a Weak Echo Region (WER), which, when fully encircled by mid-level reflectivity, it is classified as BWER.

Embryo curtain

The position of the stagnation point, defined as the point at which the storm's impinging middle levels airflow achieves zero net velocity relative

to the updraft, is governed by the interaction between the rotating updraft and environmental flow. These airflow patterns are associated with the formation of the overhang reflectivity core, also known as the embryo curtain. This consists of a mid-level reflectivity pattern that bounds the vault on the western flank of the updraft, in the direction of the storm's travel, and creates a corridor for the preferential injection of hail embryos into the updraft. This structure originates from mesocyclone erosion through the action of the external flow, creating a region of recirculating air with sub-adiabatic lapse rates and reduced moisture content, with significant implications for hail growth processes as documented in [8] and [9]. These conditions altogether promote a region of slow but effective hail embryos growth, including graupel, frozen drops and sleet, by shielding them from the intense updraft core speeds that would otherwise eject them out of the anvil. Hail embryos originating from the embryo curtain follow one of two primary pathways: either direct ingestion into the updraft or re-entry through the inflow base following initial precipitation. These embryos become advected by the mean wind, traversing the updraft while undergoing substantial growth via intense riming processes. The updraft's unique microphysical environment, characterized by undepleted liquid water content due to condensation inefficiency in strong vertical currents, creates ideal conditions for such growth. The development of large hail occurs through a time-dependent equilibrium between the particle's increasing weight (governed by its growth rate) and the spatiotemporal variations in updraft velocity. When this balance eventually breaks down, the hailstones descend to the surface, feeding into the FFD. A visualization of the BWER and of the embryo curtain is presented in the conceptual drawing of

Chapter 2

Physical modelling, observational and numerical simulation methodology

2.1 Model and Microphysical parametrisation schemes

2.1.1 ICON model

The NWP model examined in this thesis is the ICON model, developed by the Deutscher WetterDienst (DWD) in collaboration with the Max Planck Institute for Meteorology (MPI-M), the Deutsches KlimaRechenZentrum (DKRZ), and the Karlsruhe Institute of Technology (KIT). By adjusting

the horizontal mesh size, the ICON model can be configured to run global simulations at 13 km horizontal grid resolution (ICON-GLOBAL), with the possibility of a 6.5 km nest ever central Europe (ICON-EU), LAM, with regional nested grids on the order of the kilometre, up to Large Eddie Simulation (LES) for studies on the atmospheric turbulence. With reference to regional models, ICON-2I is the high-resolution model (with a horizontal grid resolution of 2.2 km) operating over the Italian domain (Fig. 2.1). It is mainteined and developed by the National Meteorological and Climate Service for Italy (*Agenzia ItaliaMeteo*), in collaboration with Agenzia Regonale Protezione Ambiente Energia Emilia-Romagna (Arpae). ICON-2I is a convection permitting model because the adopted grid resolution allows it to only partially solve for convection processes. In particular, deep convection is fully resolved; instead, shallow convection is parametrized. The LAM model only simulates a portion of the Earth that is inevitably interconnected with the rest of the atmospheric domain. The feedbacks from the outside atmospheric evolution is regularly provided to the edges of the LAM domain in the form of Boundary Conditions (BC). Accurate BC ensure that errors within the model remain contained.

Generalities on the ICON model The ICON model is composed of discretised thermo-hydrodynamical partial differential budget equations formulated in a terrain-following coordinate system, employed to describe a non-hydrostatic bi-phase system consisting of dry air and water in its vapour, liquid and solid forms. The fundamental equations describing the evolution of the prognostic atmospheric variables are grouped into a dynamical core, encompassing the dry Navier-Stokes equations for the conservation of momentum and mass (Eqs. 2.1 and 2.2) and a physical core, for processes related to hydrometeor formation and development

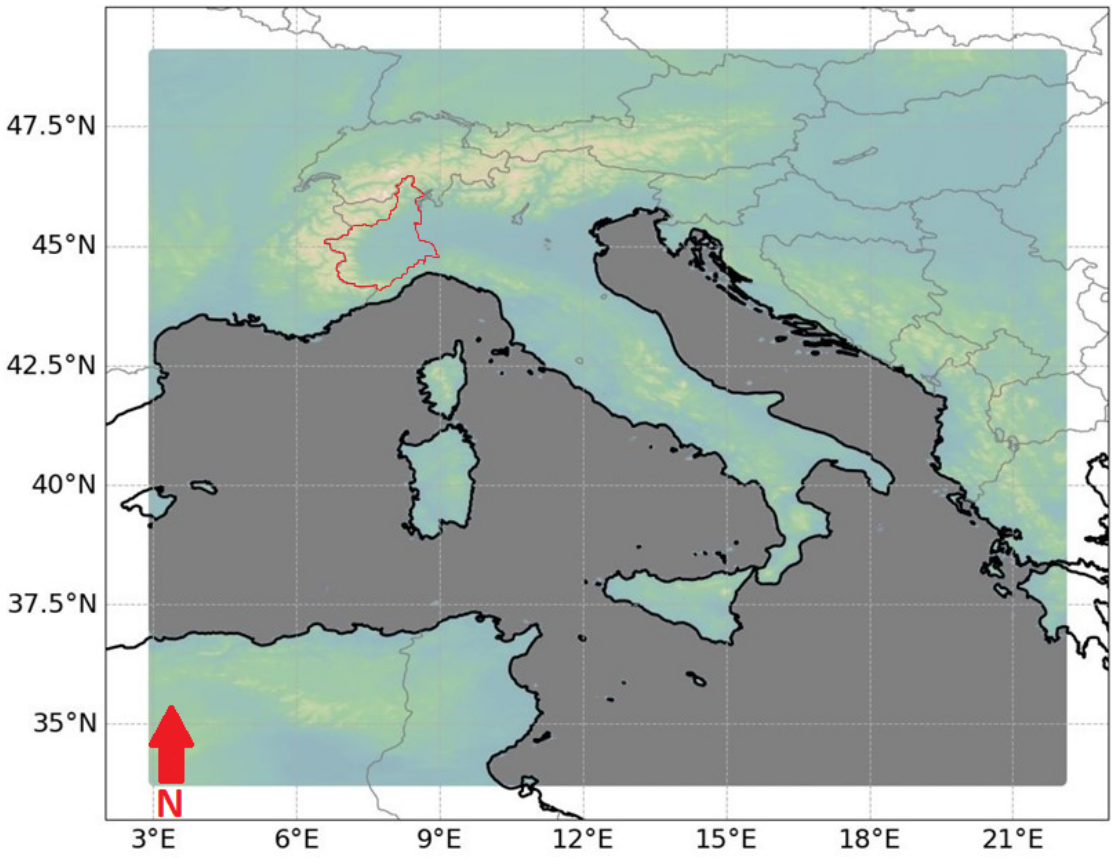

Figure 2.1: Mercator projection of the ICON-2I's horizontal domain centered on the Italian peninsula. Contours of the Piedmont region (Italy), located between 44°N and 46.5°N and between 6.6°E and 9.2°E, are highlighted in red. Source: Operational numerical weather prediction at Agenzia ItaliaMeteo and Arpae Emilia-Romagna based on the ICON model

comprising the conservation equation for the mass fraction q of constituent x and the energy conservation equation (Eqs. 2.3 and 2.4):

$$\rho \frac{d\mathbf{v}}{dt} = -\nabla p + \rho \mathbf{g} - 2\boldsymbol{\Omega} \times (\rho \mathbf{v}) - \nabla \cdot \underline{\boldsymbol{t}} \tag{2.1}$$

$$\frac{d\rho}{dt} = -\rho \nabla \cdot \mathbf{v} \tag{2.2}$$

$$\rho \frac{dq_x}{dt} = -\nabla \cdot \mathbf{J}_x + I_x \tag{2.3}$$

$$\rho \frac{de}{dt} = -p \nabla \cdot \mathbf{v} - \nabla \cdot (\mathbf{J}_e + \mathbf{R}) + \varepsilon \tag{2.4}$$

where the index x represents the constituent of the mixture (dry air, water vapour, liquid water and frozen water), I_x are the hydrometeor's source and sinks terms, $\mathbf{J}_x$ is the diffusion fluxe of constituent x, $\mathbf{R}$ is the flux density of solar and thermal radiation, $\mathbf{J}_e$ is the diffusion flux of internal energy, $\underline{\boldsymbol{t}}$ is the stress tensor due to viscosity and $\varepsilon = -\underline{\boldsymbol{t}} \cdot \nabla \mathbf{v}$ is the kinetic energy dissipation due to viscosity. The equations are integrated in time employing a predictor-corrector iterative method, halfway through the explicit first-order accuracy Matsuno scheme [10] and the implicit second-order accuracy Heun scheme [11]. Fast physics processes are solved sequentially adopting a time-split manner whereas slow physics processes are treated with a process-split manner, as shown in Fig. 2.2

The horizontal grid has its fundamental unit in a triangular cell originating from a spherical icosahedron whose edges undergo a process of initial root division into n sections followed by k bisection steps. This process identifies the nomenclature of the grid, namely RnBk, as outlined in Fig. 2.3.

Such grids avoid polar singularities of latitude-longitude grids and allow a high uniformity in resolution over the whole sphere, as can be observed

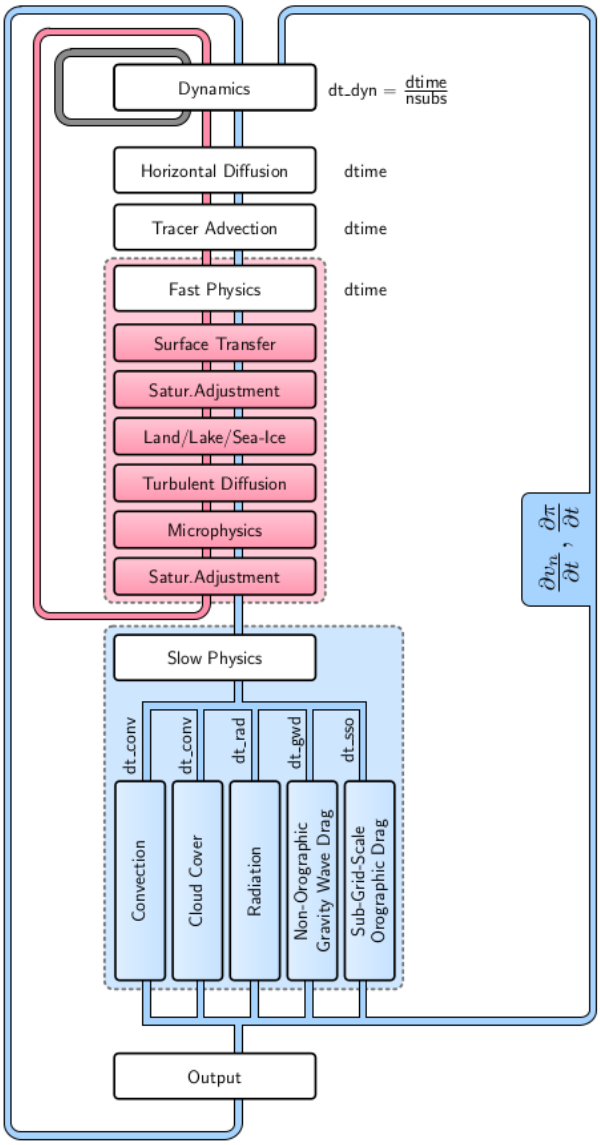

Figure 2.2: Block diagram representing the strategy adopted by ICON to couple the dynamical (white boxes) and the physics cores (red and blue boxes), subdivided in turn in fast and slow processes. The first (latter) are treated in a time-split (process-split) manner. Source: Prill, F., et al. "ICON tutorial." ICON 1 (2022).

in Fig. 2.4.

The ICON-2I nested domain is a regional R9B08 grid with a nominal horizontal resolution of $\overline{\Delta x} \simeq 2.2km$ over Italy. The "child" domain is

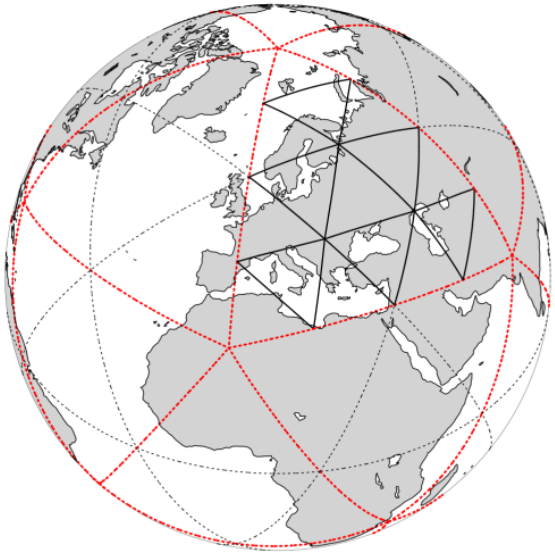

Figure 2.3: Illustration of the grid construction procedure. The original spherical icosahedron is shown in red. In this example, the initial division (n=2; black dotted) is followed by one edge bisection (k=1), yielding a finer grid (solid black lines). Source: Reinert, Daniel, et al. "DWD database reference for the global and regional ICON and ICON-EPS forecasting system." DWD 2023Available online: https://www. dwd. de/DWD/forschung/nwv/fepub/icon database main. pdf (accessed on 27 January 2023) (2020).

bounded by a *lateral boundary zone* consisting of 14 cell rows which serves the purpose of exchanging data from and to the parent grid. This zone is further subdivided into an outermost interpolation zone, where interpolated forcing of the data from the parent grid occurs, followed by a nudging zone, where the interior flow is relaxed towards the boundary conditions from the exterior.

In the vertical direction the atmospheric volume is discretised using a height-based [1] terrain-following Smooth LEvel VErtical (SLEVE)

[1] In non-hydrostatic atmospheric models, pressure is not guaranteed to decrease monotonically with height, hence height-based vertical coordinates are preferred to

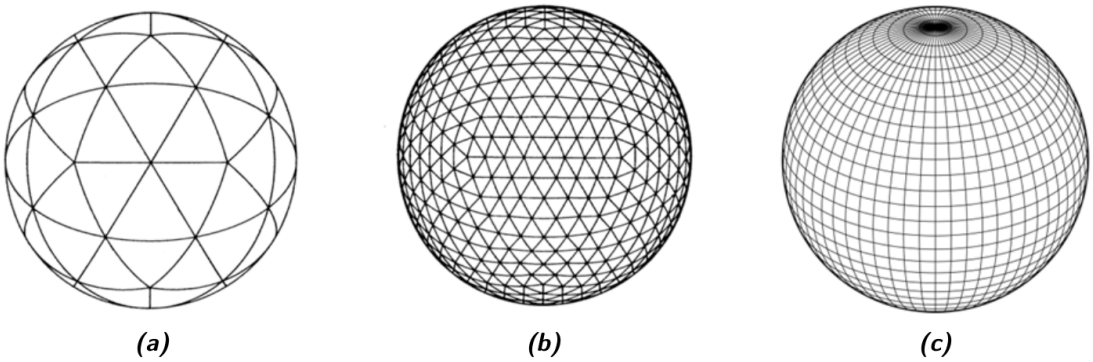

Figure 2.4: (a) Icosahedral grid with a large mesh size. (b) Icosahedral grid with a finer mesh size. (c) Regular latitude-longitude grid with singularities at the poles. Source: Reinert, Daniel, et al. "DWD database reference for the global and regional ICON and ICON-EPS forecasting system." DWD 2023Available online: https://www. dwd. de/DWD/forschung/nwv/fepub/icon database main. pdf (accessed on 27 January 2023) (2020).

coordinate system as in Fig. 2.5, here denoted with μ_s.

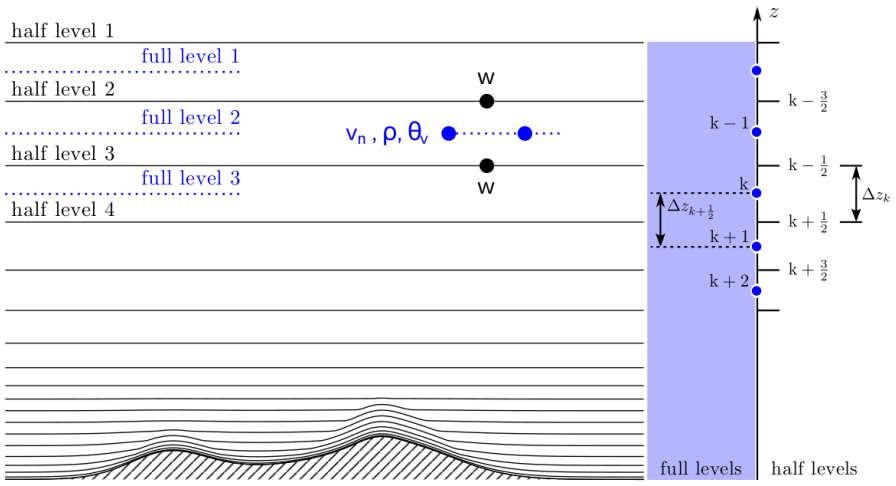

Figure 2.5: Illustration of ICON's terrein-following vertical levels. Thermodynamical quantities (ρ, θ) and the horizontal velocity components (u,v) are evaluated at full levels, whereas vertical velocity (w) is evaluated at half levels. Source: Prill, F., et al. "ICON tutorial." ICON 1 (2022).

pressure-based ones.

SLEVE coordinates allow for a relatively simple implementation of boundary conditions for the computation of atmospheric surface fields, including the no-slip condition on the velocity field.

Each one of the 65 vertical levels, denoted by mu_s and referred to as a "half-level" in ICON terminology, is the result of a mapping from an irregular curvilinear grid associated with the terrain-following coordinates into a rectangular equidistant grid labelled by integers, as illustrated in 2.6. SLEVE coordinates smoothly transition from terrain-following to flat

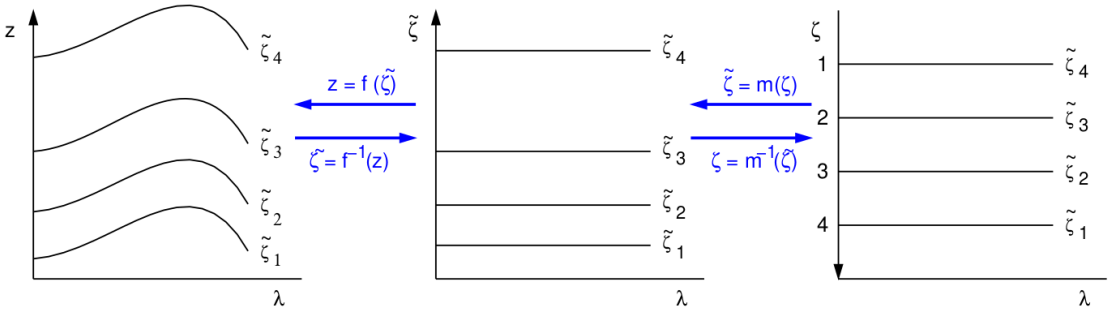

Figure 2.6: Mapping from the irregular curvilinear terrain-following grid to the index space, increasing from top to bottom, adopted for the vertical discretization. Source: Doms, G. Ü. N. T. H. E. R., and U. Schättler. "A description of the nonhydrostatic regional model LM." Part I: Dynamics and Numerics, Deutscher Wetterdienst, Offenbach 520 (2002).

horizontal levels. This is achieved by subdividing the orography $h(x, y)$ into its large, $h_1(x, y)$ and small-scale $h_2(x, y)$ components and assigning to them different decay rates, $B(\mu_s)$, in a process outlined as follows:

$$z(x, y, \mu_s) = \mu_s + B_1(\mu_s)h_1(x, y) + B_2(\mu_s)h_2(x, y) \tag{2.5}$$

being $B_1(\mu_s) < B_2(\mu_s)$. Small-scale ground features, responsible for the majority of transformation errors, dissipate more quickly with height, compared to other vertical coordinates, as can be observed in Fig. 2.7.

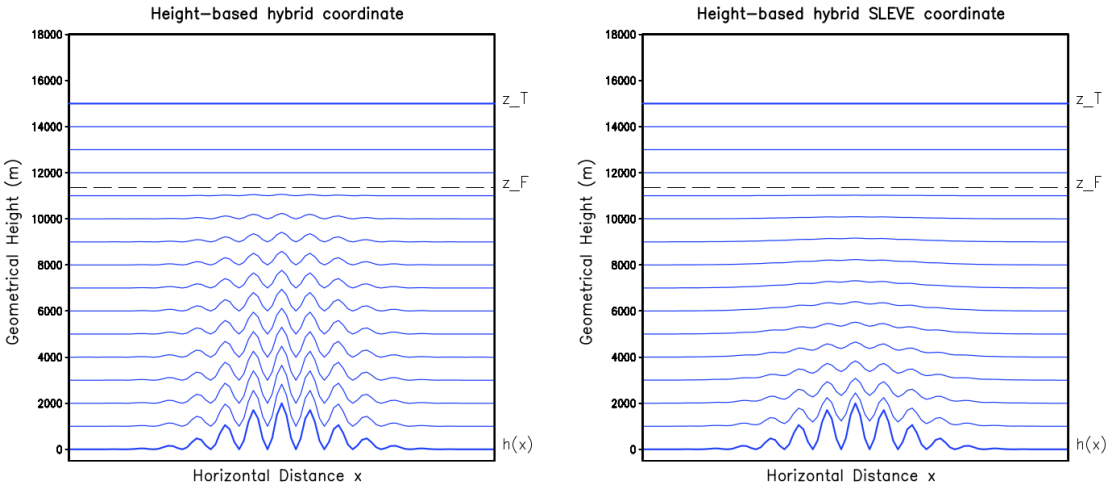

Figure 2.7: Terrain-following hybrid coordinate levels for a bell-shaped mountain superimposed by a small-scale fluctuation. Left: Geometrical height of 16 μ levels with a constant level increment of Δ_μ = 1000m from the surface to the top at $\mu_T = z_T$ = 15000m. Right: Geometrical height of 16 μ_s levels of the SLEVE coordinate with a constant level increment of Δ_{μ_s} = 1000m from the surface to the top at $\mu_{sT} = z_T$ = 15000m. Source: Doms, Günther, et al. "A description of the nonhydrostatic regional COSMO model. Part I: Dynamics and Numerics." Deutscher Wetterdienst, Offenbach, Germany (2011).

2.1.2 Assimilation technique

The set of NWP model's equations constitutes an initial value problem. Initialization of the atmospheric model state is, therefore, necessary to begin the simulation. Assimilation refers to the process of acquisition of observed data and their integration into a *first-guess* simulation in order to provide the most accurate initial state of the atmosphere. In the first numerical weather forecast, hand-interpolated analysis were used as initial conditions [12]. Nowadays, real data are captured in space and time by observational instruments, including weather ground stations, satellites and radio-soundings to cite a few and integrated in the model whithin the framework of HPC. *First-guess* fields, retrieved from a brief run of the model, are merged together with the observations to produce an *analysis*

of the initial atmospheric state, from which starts the free forecast. This operation is repeated cyclically to update the atmospheric fields with the new observations gathered. The task of assimilating sparcely distributed observations into a background field translates into the minimization of a cost function defined as the distance between a desired model state, closest to the observed one, and the background state. Depending on the method adopted to distribute in space and time the available informations from sparce observations, several approaches to data assimilation can be individuated. Variational assimilation (3D Var, 4D Var), working on a deterministic background state, applies statistical considerations based on previous model runs to properly distribute each specific observation into its neighborhoods. Ensemble data assimilation, instead, exploits stochastical estimators, such as the Kalman Filter, to an ensemble of background model states, with the result of a greater accuracy in high-resolution models. Lastly, a combination of variational and ensemble techniques results in a hybrid approach termed *Hybrid Ensemble Variational (EnVar)* and adopted in the assimilation cycle at DWD. More details on the assimilation approaches can be found in [13].

The assimilation system for the ICON LAMs, the Kilometre ENsemble Data Assimilation (KENDA) system, is based on Localised Ensemble Transform Kalman Filter (LETKF) technique. For the selected case study, the ensemble of BCs was not available. As a consequence, the KENDA assimilation cycle could not be applied. Instead, LHN, an assimilation technique based on radar-derived precipitation data (discussed in more detail in the next paragraph) can be applied even to deterministic models and therefore particularly suitable to our specific case.

Latent Heat Nudging Thanks to their high frequency update and spatial resolution, weather radars are increasingly being explored in this context. Radar-derived precipitation is indeed a valuable product for high-resolution data assimilation purposes. However, a direct assimilation of precipitation into the model is complicated by the presence of numerous microphysical parameterisations linking precipitation-related quantities to thermodynamic variables through processes depending on threshold values. The idea, instead, is to attribute the observed precipitation to a specific simulated thermodynamic process.

LHN, originally developed for global scales assimilation purposes, has recently been adopted to meet the needs of high-resolution NWP models. This conceptually simple, yet effective, assimilation scheme assumes a proportionality between surface rain rate and the amount of latent heat released due to precipitation formation. In fact, before precipitating to the ground, water particles undergo several phase changes that result in the release or absorption of latent heat. Integration of this quantity along the path of rainwater through the atmosphere down to the ground should provide an estimate of the rain rate

$$R(l_g) \propto \int_{l_0}^{l_g} \Delta\{L_H(l)\} dl. \tag{2.6}$$

LHN assumes that the whole path l is run through within one single model column and one single time step. The surface precipitation is then proportional to the integral of the latent heat release in the column above this point. In practice, LHN scales the model latent heat profiles by the ratio of observed to model precipitation rates. Whenever a discrepancy between radar-estimated and simulated surface precipitation rate occurs,

the air temperature deltas, namely ΔT_{LH}^{mod}, associated with the release or absorption of latent heat in the model column, are either increased or reduced accordingly, in order to match the observed conditions, as

$$\Delta T_{LHN} = (f-1)\Delta T_{LH}^{mod}, \quad f = \frac{RR_{ana}}{RR_{mod}}, \tag{2.7}$$

where $f \in [0.33,3]$, is the scaling factor composed of a ratio between RR_{ana}, a weighted sum of radar and model surface rain rates, expressed as

$$RR_{ana} = wRR_{rad} + (1-w)RR_{mod}, \tag{2.8}$$

with $w \in [0,1]$ being the weight applied to account for inaccuracies in the radar measurements whereas RR_{mod} is the model-derived rain rate. If the rainfall rate is underestimated by the model, i.e. $f > 1$, the air temperature is locally increased. As a result, an upward air motion develops, leading to condensation and initiation of precipitation processes. Conversely, when the rainfall rate is overestimated by the model, a negative temperature feedback is applied and convection is inhibited. Limitations on the scaling factor f must be imposed to prevent extreme nudging, as would occur in the case where precipitation is observed from radar but not in the model and viceversa.

The latent heat tendency contributing to the temperature change ΔT_{LH}^{mod} is retrieved from each model column and depends on the selected microphysical scheme. In the case of the three-category ice scheme (cloud ice, graupel and hail), the mass transfer rates responsible for either the release or absorption of latent heat are given in Tab. 2.1.

The equation to compute the latent heat released or absorbed as a consequence of the phase change processes described by the three-category

Table 2.1: Mass transfer rates contributing to the release/absorption of latent heat for the three-category ice scheme.

Symbol	**Process**
S_{c}	Condensation and evaporation of cloud water
S_{ev}	Evaporation of rain water
S^{c}_{frz}	Homogeneous freezing of cloud water to form ice
S^{i}_{dep}	Deposition growth and sublimation of cloud ice
S^{i}_{melt}	Melting of cloud ice to form cloud water
S^{r}_{cri}	Freezing of rain due to collection of cloud ice (graupel formation)
S^{r}_{frz}	Freezing of rain to form graupel
S^{s}_{dep}	Deposition growth and sublimation of snow
S^{g}_{dep}	Deposition growth and sublimation of graupel
S^{s}_{melt}	Melting of snow to form rain water
S^{g}_{melt}	Melting of graupel to form rain water

ice scheme and listed in Tab. 2.1 is the following:

$$LH = \frac{\Delta T^{mod}_{LH}}{\Delta t} = \frac{L_V}{c_{pd}}(S_c - S_{ev}) + \frac{L_S}{c_{pd}}(S^i_{dep} + S^s_{dep} + S^g_{dep}) + \\ + \frac{L_F}{c_{pd}}(S^c_{frz} + S^r_{cri} + S^r_{frz} - S^i_{melt} - S^s_{melt} - S^g_{melt}). \tag{2.9}$$

The latent heat tendency derived from the double-moment scheme differs from that of the one-moment scheme because of two factors, namely the introduction of the additional hail class and the contribution of the prognosed number density of hydrometeor species to the formulation of microphysics parametrisations.

The assimilation scheme considered in this thesis is a revision [15] of

the classical LHN scheme developed by [16] for large-scale assimilation purposes, which could lead to inaccuracies if applied to high-resolution models. Additional informations on convective phenomena are indeed introduced by the use of a prognostic, rather than diagnostic, treatment of precipitation at convective scales. The impact falls on both the 3D spatial structure and the timing of the LHN. With a prognostic precipitation scheme, in fact, the model response to the LHN would be delayed by the time occurring between the formation of precipitation aloft, in response to the forcing, and the time it would take for it to reach the ground. As a result, the LHN would continue to erroneously apply a heating source although precipitation formation has already begun. This problem is addressed by adopting a "non-delayed" reference precipitation R_{ref} as the initial value to be compared with the observed precipitation in the form of vertically averaged precipitation flux, defined as:

$$R_{ref} = \frac{1}{z_{top} - z_0} \int_{z_0}^{z_{top}} \left[\sum_i \{\rho(z) q_i(z) v_i\} \right] dz, \tag{2.10}$$

where q_i is the mass fraction and v_i the sedimentation velocity of precipitate i (rain, snow or graupel). Since R_{ref} is a mixture of "undelayed" and fully delayed precipitate particles, this suggested revision only partly mitigates the timing issue.

The prognostic scheme is also able to capture the downdraughts and updraughts associated with deep convective cells. Applying a conventional LHN scheme to these regions would introduce distortions in the 3D structure of the latent heat profiles. In downdraughts regions, where high precipitation rates occur, the latent heat is often zero or sometimes negative, meaning that the LHN scheme would promote the suppression

of precipitation, despite the observed high rates. The revised scheme addresses this problem by applying the LHN only to the model columns where positive latent heat values are observed.

Updraught regions, instead, are characterised by a huge amount of latent heat release and by low precipitation values that would result in an increase of the scaling ratio of Eq. 2.7. Excessive temperature increments would therefore result from the application of LHN. To avoid them, the upper limit of the scaling factor f is reduced from 3 to 2 and the lower is increased from 0.33 to 0.5. To be effective, the revised assimilation scheme here described, with respect to a conventional LHN scheme, requires more frequent acquisitions of radar-derived precipitation observations and reduced horizontal smoothing of the radar data, complemented by the adoption of a higher-resolution model grid scale

2.1.3 Microphysics parameterisations

In numerical meteorology, microphysics refers to the set of sub-grid-scale physical processes responsible for the formation of hydrometeors[2]. Accurate representation of microphysics is essential for predicting weather phenomena and issuing timely public warnings. Since these processes occur at scales smaller than typical grid resolutions, parameterizations become necessary. The Lagrangian approach, which follows the evolution of individual hydrometeors, proves to be computationally prohibitive for operational applications. Instead, Eulerian frameworks dominate the development of microphysical schemes for operational purposes, focusing on ensemble particle behavior rather than individual trajectories.

[2]Liquid and ice particles that form in the atmosphere

Two Eulerian-type schemes have been developed: spectral (bin) and bulk moment schemes. These approaches differ fundamentally in the treatment of the Particle Size Distribution (PSD), which is the function describing particle number concentration per unit mass (or diameter) for each hydrometeor class. The PSD influences many microphysical process such as collision and melting to cite a few.

Spectral schemes Spectral, or bin, schemes explicitly compute the PSD by resolving budget equations for discrete particle size bins, representing a discrete partition of each hydrometeor size spectrum. Accurate representation of the spectral budget equations typically requires approximately 100 size bins. As an example, the diameter of a raindrop ranges from 0.05 mm for drizzle to 8 mm to 9 mm for large raindrops originating from melting hail. This approach provides the most physically accurate method for computing cloud processes, as key microphysical mechanisms can be explicitly applied to the size distribution calculation. These include equations for diffusion growth and interparticle stochastic collection. Although accurate, this method entails a significan computational cost, as it requires a high-resolution size discretization, coupled solutions for multiple interacting processes and a large memory allocation for bin storage. This represents the main limitation for operational adoption of spectral bin schemes, where computational efficiency is paramount. Nevertheless, they remain valuable as reference solutions due to their physical completeness and ability to explicitly represent the dependencies of microphysical processes on particle size and on Cloud Condensation Nuclei (CCN).

Bulk-moment schemes Bulk moment schemes, instead, prognose the PSD through the tuning of a predefined mathematical function with the parameters available. This concept is based on the assumption that an equilibrium shape for the distribution, resulting from collision-coalescence and breakup processes, is reached over time. Several PSD functions have been proposed for this purpose, including the exponential distribution [17], the gamma distribution [18], and the normalized gamma distribution [19] and [20]. For raindrops, a common formulation is represented by the exponential PSD, here generalized for any hydrometeor class x and parameterized with a single free parameter λ:

$$f_x(D) = N_0^x e^{-\lambda_x D} \tag{2.11}$$

where N_0 represents the intercept parameter, typically fixed at the constant value $8000\,\mathrm{m}^3\,\mathrm{mm}^{-1}$. The statistical properties of these functions, called moments, take the form of integrals of the size distribution $f_x(D)$ over the spectrum of all possible diameters:

$$M^k = \int_0^\infty D^k f_x(D) dD \tag{2.12}$$

where the exponent k indicates the moment's order. Each moment refers to a specific physical property of the distribution. The zeroth moment ($k = 0$) corresponds to the total particle number concentration N_x:

$$N_x = \int_0^\infty f_x(D) dD; \tag{2.13}$$

the first-order moment ($k = 1$), normalized by air density ρ, yields the mass mixing ratio q_x:

$$q_x = \frac{1}{\rho} \int_0^\infty m(D) f_x(D) dD \tag{2.14}$$

Higher-order moments describe additional distribution properties such as variance and skewness. The free parameters of the PSD can be linked to the predicted moments. The choice between single- and double-moment schemes determines the number of available parameters: the more moments are considered, the better the control over the PSD shape is. Single-moment schemes predict only the total mass, while double-moment schemes include additional equations for the total number concentration. The shape parameter λ can be determined by inverting the equation for q_x:

$$q_x = \frac{N_0^r}{\rho} \int_0^\infty m(D) e^{-\lambda_x D} dD \tag{2.15}$$

The assumption of an analitical self-similar form for the PSD allows for the parameterization of source and sink terms in the budget equations while taking into account the effects of the size distribution on these processes. This inevitably ntroduces approximations that reduce the accuracy compared to spectral schemes. The main advantage of bulk schemes, especially of single-moment ones, lies in a lower computational cost which explains their preference in operational models. Double-moment schemes have only recently gained popularity due to technological improvements regarding supercomputing.

ICON's Single-Moment Microphysics Scheme The ICON single-moment microphysical scheme is tailored for specific meteorological

conditions. In deep convection scenarios, characterized by intense meso-γ scale updrafts, the model explicitly predicts large ice hydrometeors like graupel and hail. This approach is particularly suited for high-resolution NWPs that are capable of resolving deep convective processes.

The LAM implementation exploits the three-category ice scheme [21] and [22], hereafter referred to as ICON Single-Moment (IC1M), which predicts the mixing ratios of:

- water vapor, as gaseous phase of water substances in the atmosphere;
- cloud water, as small suspended liquid drops;
- rain, liquid phase in the form of spherical drops large enough to have a non-negligible precipitation velocity;
- cloud ice, composed of small ice crystals with little or no appreciable terminal velocity nucleated directly from the water or the vapour phase or produced by ice enhancement processes;
- snow, rimed aggregates of ice crystals with fall speeds of about 0.3-1.5 m/s;
- graupel, consisting of particles with spherical shape, higher density than snow and fall speeds of about 1-3 m/s.

Hydrometeor Budget Formulation The evolution of hydrometeor mass fractions q is governed by budget equations:

$$\frac{\partial q^{l,f}}{\partial t} + \mathbf{v} \cdot \nabla q^{l,f} - \frac{1}{\rho}\frac{\partial P^{l,f}}{\partial z} = S^{l,f} - \frac{1}{\rho}\nabla \cdot \mathbf{F}^{l,f} \tag{2.16}$$

where superscripts l, f denote liquid and frozen phases, P represents precipitation fluxes (gravitational settling), S encapsulates microphysical source/sink terms, and $\mathbf{F}$ accounts for turbulent fluxes.

The scheme implements simplified versions of these equations based on hydrometeor type:

Non-precipitating hydrometeors (where turbulence dominates):

$$\frac{\partial q^{l,f}}{\partial t} + \mathbf{v} \cdot \nabla q^{l,f} = S^{l,f} - \frac{1}{\rho} \nabla \cdot \mathbf{F}^{l,f} \tag{2.17}$$

Precipitating hydrometeors (where sedimentation dominates):

$$\frac{\partial q^{l,f}}{\partial t} + \mathbf{v} \cdot \nabla q^{l,f} - \frac{1}{\rho} \frac{\partial P^{l,f}}{\partial z} = S^{l,f} \tag{2.18}$$

Process rates shown in Fig. 2.8 are derived by integrating particle growth rates over the size distribution:

$$S = \frac{1}{\rho} \int_0^\infty \dot{m} f(D) dD \tag{2.19}$$

An exception exists for autoconversion processes ($S_{au}^{c,i}$), which employ a heuristic approach following [23]. These represent:

- Cloud water → rain conversion
- Cloud ice → snow conversion

The scheme implements threshold-based autoconversion with different

parameters for liquid and ice phases:

$$S^c_{au} = \max\left\{c^c_{au}\left(q^c - q^c_0\right), 0\right\}, \quad \text{where } q^c_0 = 0.2 \text{ g/kg}, \quad c^c_{au} = 4 \times 10^{-4} \text{ s}^{-1} \tag{2.20}$$

$$S^i_{au} = \max\left\{c^i_{au} q^i, 0\right\}, \quad \text{where } q^i_0 = 0 \text{ g/kg}, \quad c^i_{au} = 10^{-3} \text{ s}^{-1} \tag{2.21}$$

Notably, this formulation lacks sensitivity to aerosol effects, preventing distinction between maritime and continental cloud regimes.

The condensation rate of water vapour, denoted by S_c, is parametrised based on the assumption of saturation equilibrium with respect to the water content in the cloud. This assumption is motivated by the evidence that observed in-cloud supersaturation is generally negligible (below 1 %). Consequently, the saturation-adjustment technique is employed. In the occurrence of supersaturation, humidity and temperature adjustments are made to reach a state of isobaric saturation. In contrast, in the event of subsaturation and $q_c > 0$ coexisting, the excess cloud water is evaporated instantaneously until either $q_c = 0$ or water saturation is achieved. This method is adequate for describing condensation in warm-rain processes. However, given that thunderstorms may develop well above the melting layer where temperatures fall beneath $T_0 = 0\,°\text{C}$, the simultaneous presence of liquid and solid forms of water necessitates a generalisation of the saturation adjustment technique. This should include the formation of cloud ice, in addition to cloud water, from the condensation of water vapour. In the region above T_0, the warm-rain

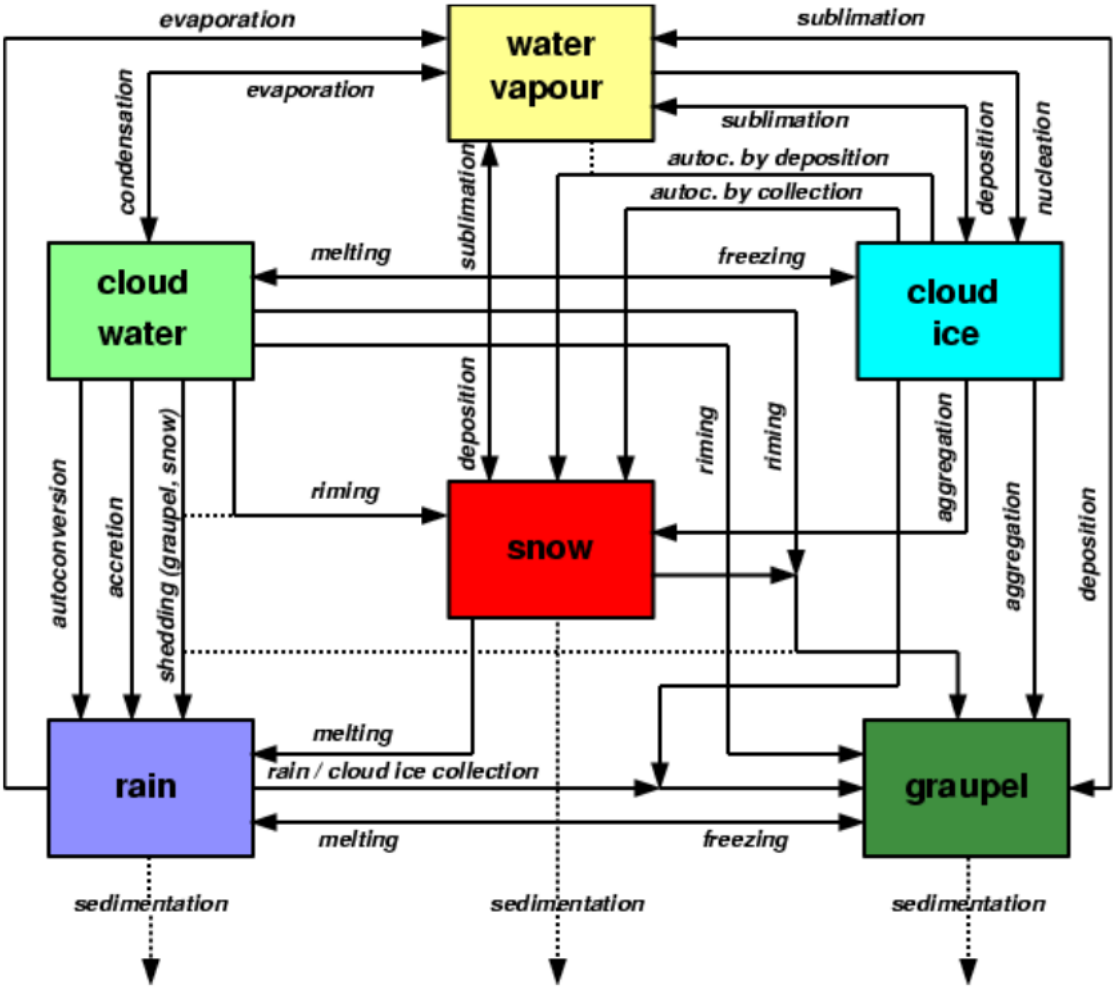

Figure 2.8: Hydrometeors classes (coloured rectangular boxes) and the cloud microphysical processes occurring between them (black lines) as simulated by the three-category ice scheme proposed by Dohms et Al. Source: Doms, Günther, et al. "A description of the nonhydrostatic regional COSMO model. Part II: Physical parameterization." Deutscher Wetterdienst, Offenbach, Germany (2011).

saturation-adjustment scheme is implemented, resulting in the absence of ice formation. However, if $T \leq T_{hn} = -40\,°\mathrm{C}$, homogeneous ice nucleation from supercooled liquid droplets becomes the predominant process. For temperatures ranging from T_{hn} to T_0, the formation of both cloud water and heterogeneously nucleated cloud-ice is possible. In the latter case, the equilibrium vapour pressure, denoted by q^*, is derived as a weighted mean of the equilibrium vapour pressure over water and ice. Consequently, supersaturated water vapour is distributed between cloud water and cloud ice in accordance with the air temperature (2.22).

$$q^* = \begin{cases} q_L^*, & \text{for } q_{CW} > 0, \quad q_{CI} = 0 \\ q_I^*, & \text{for } q_{CI} > 0, \quad q_{CW} = 0 \\ \frac{q_{CW} q_L^* + q_{CI} q_I^*}{q_{CW} + q_{CI}}, & \text{for } q_{CW}, q_{CI} > 0. \end{cases} \tag{2.22}$$

The multiple mechanisms of heterogeneous nucleation are not resolved explicitly. The process of nucleation, i.e. the formation of ice crystals from a liquid solution, occurs as a result of the presence of activated ice-forming nuclei. The calculation of their number concentration is performed in accordance with the prognostic model variables, incorporating the ice enhancement process as delineated in Eq. 2.23. This approximation is derived from aircraft measurements of the concentration of pristine crystals in stratiform clouds.

$$N_i(T) = N_0^i \exp\{0.2(T_0 - T)\}, \quad N_0^i = 1.0 \cdot 10^2 m^{-3} \tag{2.23}$$

In order to simulate the formation of graupel particles, the mechanisms of homogeneous and heterogeneous freezing of raindrops and riming of snow crystals are parametrised. The process of homogeneous freezing

is governed by the temperature parameter known as T_{hn}. With regard to heterogeneous freezing, the processes of contact and immersion nucleation, as well as collisional freezing, are simulated.

The conversion from snow to graupel through riming is parameterized based on a critical microphysical criterion. The transition occurs exclusively when the accumulated ice volume from collected supercooled droplets reaches 12 % of the original snow particle's volume. This threshold, based on experimental observations, corresponds to the point where the riming process sufficiently alters the snow crystal's structure and density to be reclassified as graupel.

ICON's Double-Moment Microphysics Scheme ICON can also apply the double-moment scheme proposed by [24] and later improved by by [22], from now on referred to as ICON Double-Moment (IC2M). Besides mass fractions, it includes budget equations to predict also the number densities of the hydrometeor classes, same as in the single-moment scheme but with the added hail class, in the form of large ice particles with very high terminal velocities (up to 50 m/s). This allows for an explicit parametrisation of all relevant homogeneous and heterogeneous nucleation processes, including a direct parametrisation of CCNs activation, which enables a distinction between maritime and continental CCN conditions, ultimately affecting the dynamical and microphysical evolution of a cloud, and a representation of aerosol-cloud interactions, important for modeling the anthropogenic influence on convective clouds and precipitation by aerosol modification. An overview of all involved hydrometeors and thei microphysical interaction processes is visualized in Fig. 2.9. From this diagram it is already clear the complexity in the parametrisation of this processes, arising from the multiple simultaneous interactions.

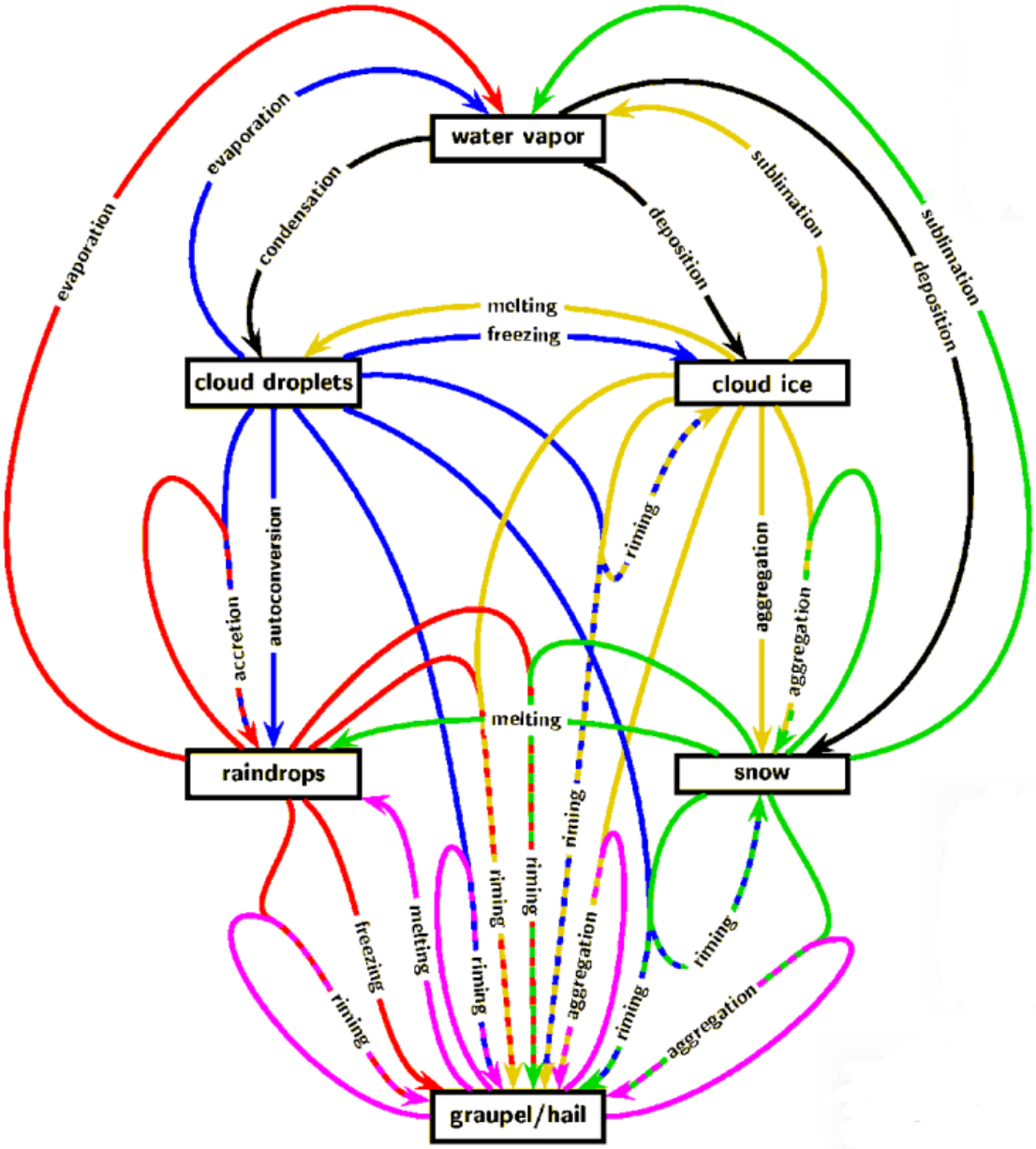

Figure 2.9: Hydrometeors classes (rectangular boxes) connected with lines, each representing a specific cloud microphysical process, as simulated by the double-moment microphysics scheme proposed by Seifert and Behang. Source: Seifert, A., Beheng, K. A double-moment cloud microphysics parameterization for mixed-phase clouds. Part 1: Model description. Meteorol. Atmos. Phys. 92, 45-66 (2006).

All hydrometeors, including cloud droplets (assumed to be mono-dispersed in size by IC1M) are assumed to be distributed following a generalised Γ-distribution

$$f_c(x) = Ax^{\nu} \exp\left(-\lambda x^{\mu}\right) \tag{2.24}$$

This distribution presents two time-dependent, namely A and λ, and two constant parameters, μ and ν, specific of each hydrometeor's class, as summarized in Tab. 2.2.

Regarding raindrops, a droplet radius of $r^* = 40\mu m$ has been selected to distinguish between the smaller droplets, belonging to the cloud-water class, and the larger raindrops. This partition produces a subdivision in the PSD, from which the moments are computed as follows:

$$M_c^k = \int_0^{\infty} x^k f_c(x) dx, \tag{2.25}$$

$$M_r^k = \int_0^{\infty} x^k f_r(x) dx, \tag{2.26}$$

where k refers to the moment's order, c stands for cloud water and r for raindrops.

The nucleation mechanism for cloud water, overlooked in bulk-schemes, is here directly parametrised by time-differentiating an empirically-derived aerosol activation equation

$$N_{CCN} = C_{CCN} S^k, \quad S \text{ in } \% \tag{2.27}$$

where C_{CCN} is the number density of cloud condensation nuclei and S^k is a coefficient-dependent supersaturation with respect to water. In a maritime

Table 2.2: Hydrometeor parameters of the generalized gamma distribution for the IC2M scheme, including minimum and maximum values of mean particle mass as reported in [Seifert, Axel, and Klaus Dieter Beheng. "A two-moment cloud microphysics parameterization for mixed-phase clouds. Part 1: Model description." Meteorology and atmospheric physics 92.1 (2006): 45-66.].

Hydrometeor	**a** ($\mathbf{kg^{-b}\,m^3}$)	**b**	**v**	$\boldsymbol{\mu}$	**xmin** (**kg**)	**xmax** (**kg**)
Cloud	0.124	0.333	0.0	0.333	4.20×10^{-15}	2.60×10^{-10}
Rain	0.124	0.333	0.0	0.333	2.60×10^{-10}	3.00×10^{-6}
Ice	0.835	0.390	0.0	0.333	1.00×10^{-12}	1.00×10^{-6}
Snow	2.400	0.455	0.0	0.500	1.00×10^{-10}	2.00×10^{-5}
Graupel	0.142	0.314	1.0	0.333	1.00×10^{-9}	5.00×10^{-4}
Hail	0.137	0.333	1.0	0.333	2.60×10^{-9}	5.00×10^{-4}

scenario, all CCNs are assumed to be active as soon as $S \geq 1.1$ %, meaning that no further nucleation occurs. Adjusting C_{CCN} and k, maritime and continental scenarios can be simulated. For example, CCNs on land, especially over industrialized urban areas where the production of particulate is massive, are denser than on sea. In the context of this work, the continental scenario has been adopted.

The rate at which water vapor, in a supersaturated environment, deposits on activated CCNs to produce cloud droplets, is formulated as:

$$\left.\frac{\partial N_c}{\partial t}\right|_{nuc} = \begin{cases} C_{ccn} k S^{k-1} \frac{\partial S}{\partial z} w, & \text{if } S \geq 0,\ w\frac{\partial S}{\partial z} > 0 \\ & \text{and } S < S_{max} \\ 0, & \text{else,} \end{cases} \tag{2.28}$$

and, in terms of mass density

$$\left.\frac{\partial L_c}{\partial t}\right|_{nuc} = x_{c,nuc} \left.\frac{\partial N_c}{\partial t}\right|_{nuc} \tag{2.29}$$

where $x_{c,nuc} = 10^{-12}\ kg$ is an arbitrarily chosen smallest drop mass. Vertical air motions, $w\frac{\partial S}{\partial z}$, are predominant in the activation process.

As outlined in Chapter 1.2, after nucleation, cloud water particles undergo diffusion and collision-coalescence processes. Since these growth processes proceed at substantial different speeds, the slowest being diffusion, this phase of the hydrometeor's life is dominated by collection. The following collection processes have been parametrised starting from the Stocastic Collection Equation (SCE):

- Selfcollection of cloud water (raindrops), namely the growth of droplets by mutual coagulation but remaining in the same hydrometeor class;
- Autoconversion, which refers to the formation of raindrops by coagulating cloud water;
- Accretion terms the growth of raindrops by collecting cloud water;
- Collisional breakup is the fragmentation of raindrops after reciprocal collision

Parametrisation of the combined effects of selfcollection and breakup, should result in the observed self-similar equilibrium size distribution of raindrops, achieved through relaxation of the raindrop ensemble to an equilibrium mean diameter.

Moving to the ice phase, a generalized Γ-distribution is assumed for all ice particles (cloud ice, snow, graupel and hail). The first process

encounterd in the formation of an ice crystal is nucleation, consisting on the activation of an ice nucleum above which water vapor deposits. Ice nucleation is parameterised using an adjustment for the number density of ice activated nuclei $N_{IN}(S_i, T)$, computed by applying the deposition-condensation nucleation formula [25]. The equations for the number density and mass of nucleated ice crystals reads, respectively:

$$\left.\frac{\partial N_i}{\partial t}\right|_{nuc} = \begin{cases} \frac{N_{IN}(S_i,T)-N_i}{\Delta t}, & \text{if } S_i \geq 0 \text{ and } N_i < N_{IN}(S_i,T) \\ 0, & \text{else} \end{cases} \tag{2.30}$$

and

$$\left.\frac{\partial L_i}{\partial t}\right|_{nuc} = x_{i,nuc} \left.\frac{\partial N_i}{\partial t}\right|_{nuc} \tag{2.31}$$

where positive supersaturation with respect to ice, namely S_i, must occur for ice phase initiation. Further growth of ice particles by deposition is parametrised, similarly to the liquid phase processes, by adopting an analogy with the boundary conditions for electrostatic and diffusion problems, which produces the following depositional growth equation for ice

$$\frac{\partial L_i}{\partial t}|_{dep} = \frac{4\pi}{c_i} G_{iv}(T,p) \int_0^\infty D_i(x) F_v(x) f_i(x) dx, \tag{2.32}$$

where $\frac{D_i}{c_i}$ is defined as the capacitance (C) of the crystal, which depends uniquely on its particular shape. Cloud ice is assumed to have the shape of an "hexagonal plate", snow is described by mixed aggregates and hail with the "lumped graupel" geometry of [26].

The influence of the collection processes on the evolution of the PSD moments is approached in a novel manner, whith the aim to avoiding

the use of look-up tables and overcoming the limitations of standard formulas. The interaction between two sets of particles is described as function of a mean efficiency that depends only on the mean masses, a characteristic velocity difference term and a geometric term depending on their diameters. Describing the PSD with a Γ-function and a power relation between mass and diameter, yields a feasible analytical evaluation of the collection integrals for processes including riming, autoconversion, accretion, aggregation, ice enhancement and multiplication.

Ice particles originating from freezing of raindrops are subdivided either into the graupel or hail class according to the size of the associated raindrop. The freezing of larger raindrops produces a graupel of greater density that can serve as an embryo of hail, according to the World Meteorological Organization (WMO) definition of hail, while smaller frozen raindrops contribute to the graupel category and, finally, even smaller frozen reaindrops are assigned to the category of cloud ice. This classification, visualized in Fig. 2.10, is motivated by the fact that not all freezing raindrops should be treated as solid ice spheres. Actually, the growth by condensation of small ice particles, known as the Bergeron-Findeisein process, produces low density ice crystals.

The growth of hail by interparticle collision is not considered. Wet-growth, yielding observed large hail sizes is, instead, taken into account. The parametrisation of this process involves the computation of the Schumann-Ludlam-limit, i.e. a lower limit to the size of the hail diameter for the onset of wet growth, by solving a steady-state heat-flux balance equation that imposes the bulk temperature $T_s \approx 0°C$. To model the growth of large ice particles, such as graupel and hail, through collection and collision processes, a continuous growth equation is adopted. This is

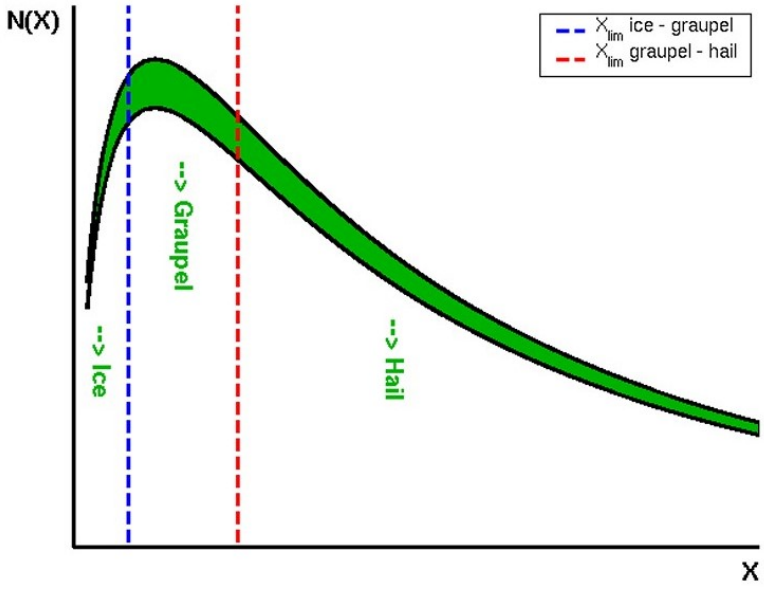

Figure 2.10: Schematic diagram of spectral partitioning of freezing raindrops into three different ice classes depending on the diameter size of the original raindrop, namely cloud ice, gruapel and hail with increasing sizes of the freezing raindrop, as proposed in the revision of the double-moment scheme by Blahak. Source: Blahak, Ulrich. "Towards a better representation of high density ice particles in a state-of-the-art two-moment bulk microphysical scheme." Proc. 15th Int. Conf. Clouds and Precip., Cancun, Mexico. Vol. 20208. 2008.

motivated by the sheer difference in diameter of graupel/hail and cloud droplets which reflects the sparse population of these ice categories within a more uniform distribution of droplets.

2.1.4 Model set-up and post-processing

For the purposes of this study, four different configurations of ICON model were tested, combining the different microphysics schemes with the use or non-use of the LHN. To make specific simulations easier to recognise, the convention has been adopted of naming them after the acronyms of the implemented microphysics and, where applicable, assimilation

scheme. According to this convention, the first simulation, which has the same characteristics as operational runs, is referred to as IC1M, the second as IC2M, the third is referre to as ICON Single-Moment with LHN (IC1M-LHN) and the fourth as ICON Double-Moment with LHN (IC2M-LHN). Each run is a cold start[3] deterministic 24-hour forecast initialised at the same time. The initial and boundary conditions have both a horizontal resolution of 6.5 km and are remapped onto the ICON-2I grid. A 20 seconds time-step has been adopted to integrate in time the equations of the model dynamical core. In runs with LHN assimilation, the instantaneous precipitation estimated by the Italian radar composite is provided every 10 minutes. Tab. 2.3 lists the features of the ICON configurations in the four simulations performed. The model output variables relevant for this analysis, listed in Tab. 2.4 were archived with temporal resolution optimized for their physical characteristics: (1) slowly evolving thermodynamic fields (temperature, pressure) at 30-minute intervals, (2) precipitation fields every 10 minutes, and (3) radar-observable quantities and hydrometeor concentrations at 5-minute sampling to resolve the rapid microphysical evolution characteristic of convective storms.

All numerical simulations were executed on Galileo100 in a dedicated partition of the CINECA HPC infrastructure allocated to the ARPA Piemonte (Bologna, Italy). The computational resources comprised two nodes, each equipped with 18 processing cores. For verification purposes, the model output are retrieved by applying a rectangular geographical mask to the ICON-2I domain that trims only the northern Italian territory, with latitudes and longitudes ranging from 43.7°N to 47.2°N and 6.5°E to 13.8°E, respectively. The post processing phase has been conducted in a

[3]Initialisation of NWP model by interpolating analyses from a global model

Table 2.3: Description of the different ICON configurations used

Settings	**IC1M**	**IC1M-LHN**	**IC2M**	**IC2M-LHN**
Grid spacing (km)	2.2			
Dynamical time step (s)	20			
Vertical η levels	65			
Period of simulation	From 00:00 UTC 06/07/2023 to 24:00 UTC 06/07/2023			
Boundary conditions	ICON-EU re-forecasts (every 10 min)			
Initial conditions	ICON-EU analysis valid at 00:00 UTC 06/07/2023			
Assimilation	/	LHN	/	LHN
Output writing time	`icon_file`: every 30 min `prec_file`: every 10 min `radar_file`: every 5 min			
Parametrisations				
Microphysics	Doms et Al. [27]		Seifert & Beheng double moment [24]	
Radiation	Rapid Radiative Transfer Model (RRTM) [28], [29]			
Deep convection	Explicit			
Shallow convection	[30] with $lshallowconv\_only$=.TRUE			

Python environment with the use of specific meteorological toolsets such as MetView, to realize the cross-section of the model results, and MetPy, to create the SkewT-logP plots.

2.2 Observational tools

To analyse the case study and to validate the model results, observations from ground weather stations, weather radars and radiosoundings are considered.

2.2.1 Ground weather stations

The ground weather station network of ARPA Piemonte provides the meteorological situation on the surface for the Piemonte region. It consists of 400 stations distributed on the ground with a density of almost one

Table 2.4: Description of the variables retrieved from the ICON model simulations

File	Frequency	Variable shortname	Units	Extended name
ICON	30 min	u	$m\,s^{-1}$	U component of velocity
		v	$m\,s^{-1}$	V component of velocity
		wz	$m\,s^{-1}$	W component of velocity
		10u	$m\,s^{-1}$	U component of 10 meter velocity
		10v	$m\,s^{-1}$	V component of 10 meter velocity
		10fg	$m\,s^{-1}$	Maximum 10 meter wind gust
		t	K	Air temperature
		2t	K	2 meter air temperature
		2d	K	2 meter dew point temperature
		pres	Pa	Pressure
		$CAPE_{ML}$	$J\,kg^{-1}$	Mixed Layer CAPE (MLCAPE)
		CIN_{ML}	$J\,kg^{-1}$	Mixed Layer CIN (MLCIN)
		LPI	$J\,kg^{-1}$	Lightning Potential Index
PREC	10 min	tp	$kg\,m^{2}$	Total precipitation
		crr	$kg\,m^{-2}\,s^{-1}$	Convective rain rate
		lsrr	$kg\,m^{-2}\,s^{-1}$	Large scale rain rate
		tgrp	$kg\,m^{-2}$	Graupel precipitation
		$HAIL_{GSP}$	$kg\,m^{-2}\,s^{-1}$	Hail precipitation rate
RADAR	5 min	bref	dBZ	Radar reflectivity
		q	$kg\,kg^{-1}$	Specific humidity
		clwmr	$kg\,kg^{-1}$	Cloud water mixing ratio
		rwmr	$kg\,kg^{-1}$	Rain water mixing ratio
		snmr	$kg\,kg^{-1}$	Snow mixing ratio
		QI	$kg\,kg^{-1}$	Cloud ice mixing ratio
		grle	$kg\,kg^{-1}$	Graupel mixing ratio
		QH	$kg\,kg^{-1}$	Hail mixing ratio

station per square kilometre. From the station network, only those of interest for the event under investigation have been selected (Fig. 2.11). Table 2.5 lists the sensors of each station considered for the study, together with the quantity measured and the frequency of measurements.

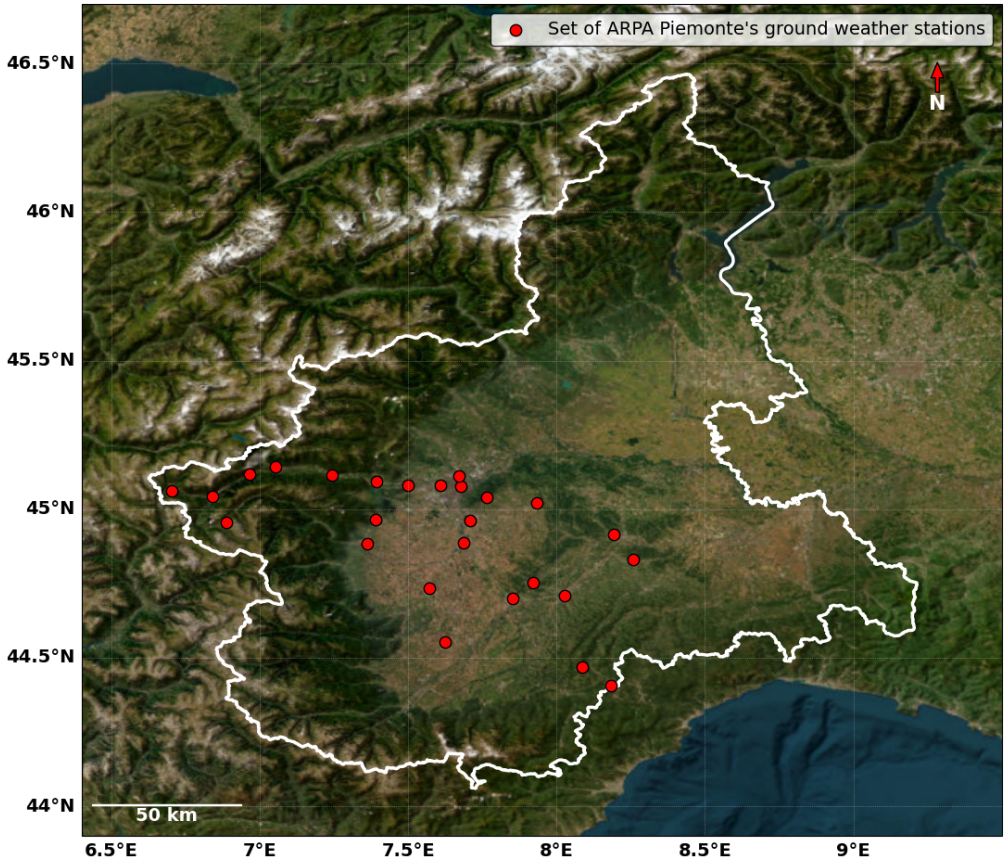

Figure 2.11: Locations of the ARPA Piemonte ground weather stations (red dots) placed along the supercell course superimposed on the satellite map of Piedmont (Italy). Image produced with OpenStreet Map.

2.2.2 Radiosoundings

Radiosoundings consist in the measurement of atmospheric variables through a set of sensors mounted on a buoyant probe which is often launched twice a day. Data, transmitted to the ground via radio waves, provide a detailed description of the vertical atmospheric profile above a specific location, useful in the initialisation phase of an atmospheric model, for real-time assessment of weather patterns and in the analysis of past events. For this study, the radiosounding stations at SLE, LIMN and

Table 2.5: Instrumentation and measurement specifications of ARPA Piemonte weather stations

Instrument	**Measured quantity**	**Unit**	**Frequency (min)**
Thermometer	Air temperature	°C	30
Barometer	Atmospheric pressure	hPa	30
Rain gauge	Precipitation	mm	10
Radiometer	Solar radiation	$\mathrm{W\,m^{-2}}$	10
Anemometer	Wind speed	$\mathrm{m\,s^{-1}}$	10
Wind vane	Wind direction	° (clockwise from N)	10

SPC shown in Fig. 2.12 have been considered.

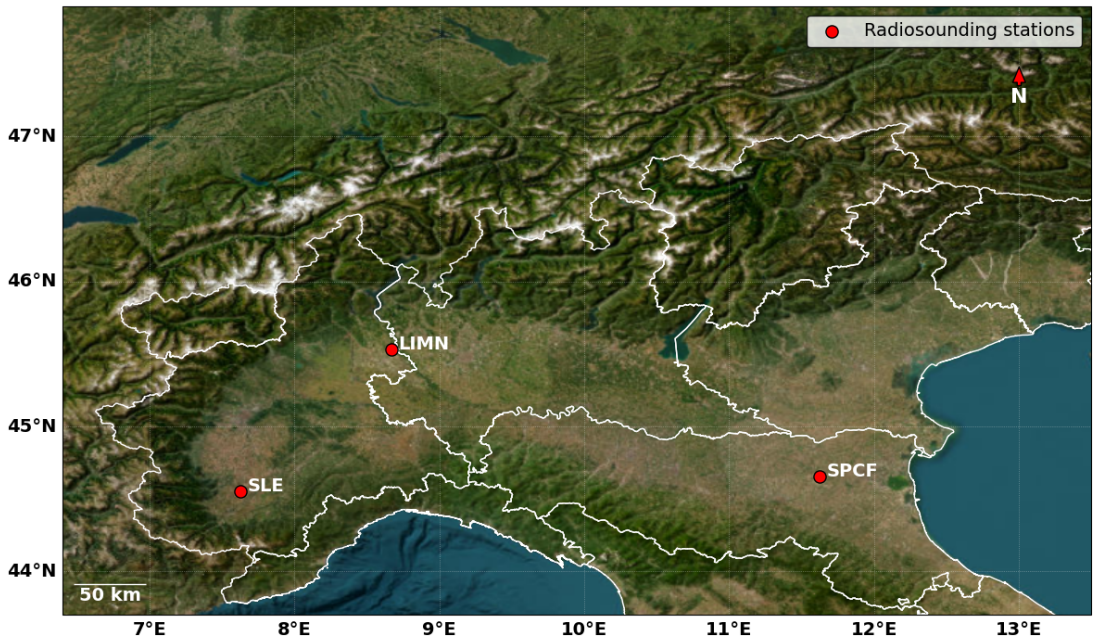

Figure 2.12: Locations of the radiosounding stations (red dots) considered in the analysis superimposed on the satellite map of Northern Italy. Image produced with OpenStreet Map.

CAPE The vertical profiles of air and dew point temperature, obtained from a radiosounding, are used to calculate the CAPE, an important parameter for assessing the convective instability of the atmosphere and the potential for thunderstorm development. CAPE, expressed in $\mathrm{J\,kg^{-1}}$, is proportional to the positive area comprised between the temperature curves produced by the parcel ascent and that of the actual atmospheric temperature profile. The parcel, considered in equilibrium in terms of heat exchange with the environment, is assumed to rise dry-adiabatically at the

beginning, then follows a moist-adiabatic profile ascent as soon as the dew point temperature is reached. Water vapour contained inside the air parcel saturates, releasing the heat of condensation, which significantly increases the air parcel's temperature. As soon as the temperature of the ascending air parcel exceeds that of the ambient air, the parcel rises freely due to buoyancy forces acting on them resulting from the density differences. The height where this phenomenon first occurs defines the Level of Free Convection (LFC). During the ascent, the parcel cools until it reaches the EL, where both its temperature and that of the ambient air are in equilibrium with each others, with the result that the air parcel decelerates until it run out of the kinetic energy gained during the ascent. CAPE is computed as the integral from the LFC to the EL of the buoyant energy, function of the temperature difference between the air parcel considered and the ambient air as

$$CAPE = g \int_{LFC}^{EL} \frac{T_v - T_{v,e}}{T_v} dz, \tag{2.33}$$

where g is the acceleration due to gravity, T_v and $T_{v,e}$ are the virtual temperatures of the air parcel and of the environment, respectively. High CAPE values are representative of a highly unstable atmosphere, potentially leading to severe weather conditions, whereas a neutrally buoyant atmosphere result in a CAPE near zero. If the atmosphere is stably stratified, the CAPE would be negative, meaning that energy should be provided to the atmosphere in order to lift a parcel of air up to the LFC. This energy is referred to as convective inhibition and is quantified by the CIN parameter

$$CIN = -g \int_{IN}^{LFC} \frac{T_v - T_{v,e}}{T_v} dz, \tag{2.34}$$

where IN is the level where the parcel originates. Different CAPE and CIN values can be computed, depending on the properties of the rising air parcel considered in order to have a clearer understanding of the atmospheric instability. A distinction is made between Surface Based CAPE (SBCAPE), MLCAPE, Most Unstable CAPE (MUCAPE) and Surface Based CIN (SBCIN), MLCIN and Most Unstable CIN (MUCIN). Surface-based is adopted to conisider the instability generated from an airmass rising from the surface layer. The mixed-layer, instead, is an average of the thermodynamical properties of air in the first 150 hPa, representative of the inflow layers of a surface-based thunderstorm. In case of elevated instability, information retrieved from the most unstable air parcel is preferrable, since the most unstable parcel of the whole sounding is considered. Radiosoundings also measure wind speed and direction with height. These are later combined and plotted on a hodograph, a curve connecting the tips of the wind vectors at increasing heights, making it easier to visualise vertical wind shear and Storm Relative Helicity (SRH), a measure of cyclonic vorticity.

Vertical wind shear Vertical wind shear is defined as the difference in wind speed and direction between two vertical levels. It is typically computed within the first 0-1, 0-3, and 0-6 kilometres. Relevant wind shear values in these layers suggest favourable conditions for the formation of multicell and supercell thunderstorms. Traditionally, wind shear associated to the 0-1 km layer is the most useful in forecasting tornadogenesis, whereas that in the first 0-3 km is more representative of the thunderstorm's ingestion layers. Lastly, the 0-6 km layer should provide sufficient coverage of the effective vertical development of the updraft. The work of [31] discusses a technique that analyses the minimum constraints on lifted parcel CAPE and

CIN in order to provide the greatest probability of detecting an effective inflow layer for storm-related parameter assessment. The inflow layer is composed of air parcels possessing either a CAPE of at least 100 J/kg or a CIN greater than -250 J/kg along the vertical sounding shown in the Skew-T Log-p diagram. Computing the wind shear inside this layer produces the Effective Bulk Wind Difference (EBWD). Wind direction as a function of height is visualised on the Skew-T Log-p plot using arrows pointing in the direction in which the wind is blowing. Wind speed magnitude is quantified using ticks called barbs, which are added to the arrows. Half a barb for 5 knots, a full barb for 10 knots and a flag for 50 knots.

Storm relative helicity When an updraft interacts with streamwise horizontal vorticity, a vortex tube with vertical vorticity is created. Particles inside this tube, called mesocyclone, follow a helical trajectory, resulting from the combined effects of vertical motion and rotation acting on them. Helicity is the measure of the intensity of this rotation. Since supercells move with respect to the mean winds, SRH, which takes into account the environmental winds relative to storm propagation, is more useful. To be more representative of the thunderstorm structure, SRH is computed as the integral of an infinitesimal helicity over the vertical layers constituting the effective thunderstorm inflow region, retrieved with the same method described in Paragraph 2.2.2. The result is the Effective Storm Relative Helicity (ESRH) parameter, with units of m^2/s^2, computed as

$$eSRH = \int_{eib}^{eit} H' \, dz, \tag{2.35}$$

where

$$H' \approx V'_{avg} \cdot \frac{\partial U'}{\partial z} - U'_{avg} \frac{\partial V'}{\partial z}, \tag{2.36}$$

"eib" stands for the effective-inflow base and "eit" for the effective-inflow top. U'_{avg} and V'_{avg} are averages of the storm-relative environmental horizontal winds between an infinitesimal vertical distance dz. This parameter is of relevance for the evaluation of storm severity. As documented by [32], a strong rotating environment leads to a storm organization which is stable against perturbations and can persist for hours in the same configuration. SRH can be easily visualized on a hodograph as twice the area comprised between the storm relative wind shear vector between inflow base and top and the curve tracked by the tip of the environmental wind vector with height as in Fig. 2.13

(Effective) Supercell Composite parameter As discussed in Chapter 1.2, the combined effect of convective instability, wind shear and helicity could create a favourable environment for supercell development. The Supercell Composite Parameter (SCP), by taking into consideration this three quantities, is able to distinguish between non-supercell, non-tornadic supercell and tornadic supercell situations, establishing the potential for supercell development with reasonable approximation. Traditionally, the wind shear and the helicity terms composing the SCP have been formulated in terms of an arbitrarily chosen atmospheric vertical layer comprised in the first 3 km of the sounding. Recent updates [34] have considered, for this purpose, the effective inflow layer of the thunderstorm. In this analysis, both versions are adopted, namely the classic one:

$$SCP = \frac{MUCAPE}{1000\,\mathrm{J\,kg^{-1}}} \cdot \frac{BWD}{20\,\mathrm{m\,s^{-1}}} \cdot \frac{SRH}{50\,\mathrm{m^2\,s^2}}, \tag{2.37}$$

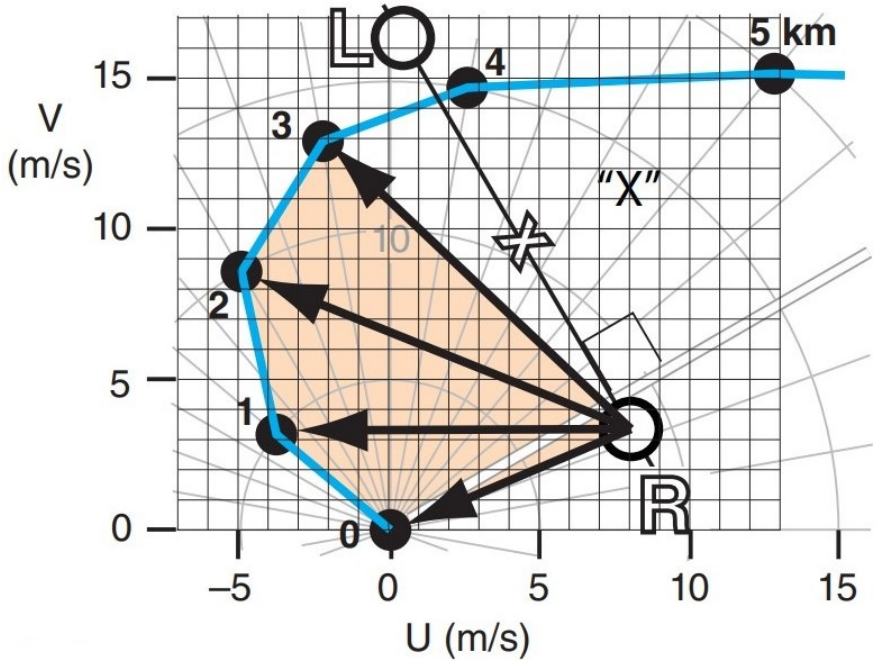

Figure 2.13: The orange shaded area represents half of the SRH value, computed for a right-moving supercell "R" with Bunker ID technique [33] in the first 0-3 km atmospheric layers. Source: Stull, Ronald B. Practical meteorology: an algebra-based survey of atmospheric science. University of British Columbia, 2015.

and the update one, with calculations within the effective inflow layer:

$$eSCP = \frac{MUCAPE}{1000\,\mathrm{J\,kg^{-1}}} \cdot \frac{EBWD}{20\,\mathrm{m\,s^{-1}}} \cdot \frac{ESRH}{50\,\mathrm{m^2\,s^2}}. \tag{2.38}$$

The EBWD term is restricted to the $0.5 < \frac{EBWD}{20\,\mathrm{m\,s^{-1}}} < 1.5$ interval. Outside this range a zero value is assigned to EBWD. Values grater than 1 indicate the increasing likelihood of right-moving supercell development, whereas values lower than -1 favours left-moving supercells. The diagram in Fig. 2.14 relates the effective Supercell Composite Parameter (eSCP) value to the type of supercell, ranging from non-supercell to supercell with significant tornado potential. It can be seen that values greater than 1 and

lower than 5 define the range of possible eSCP favouring the formation of a non-tornadic supercell. It should be noted that the ranges and scaling factors admitted for the MUCAPE, ESRH and EBWD parameters, as well as the minimum CAPE and CIN constraints used to identify the effective inflow layer, are representative of the North American atmospheric scenario and may be inappropriate when applied to the Padania valley in Piedmont, Italy. Nevertheless, the SCP and eSCP values found serve as a relative reference.

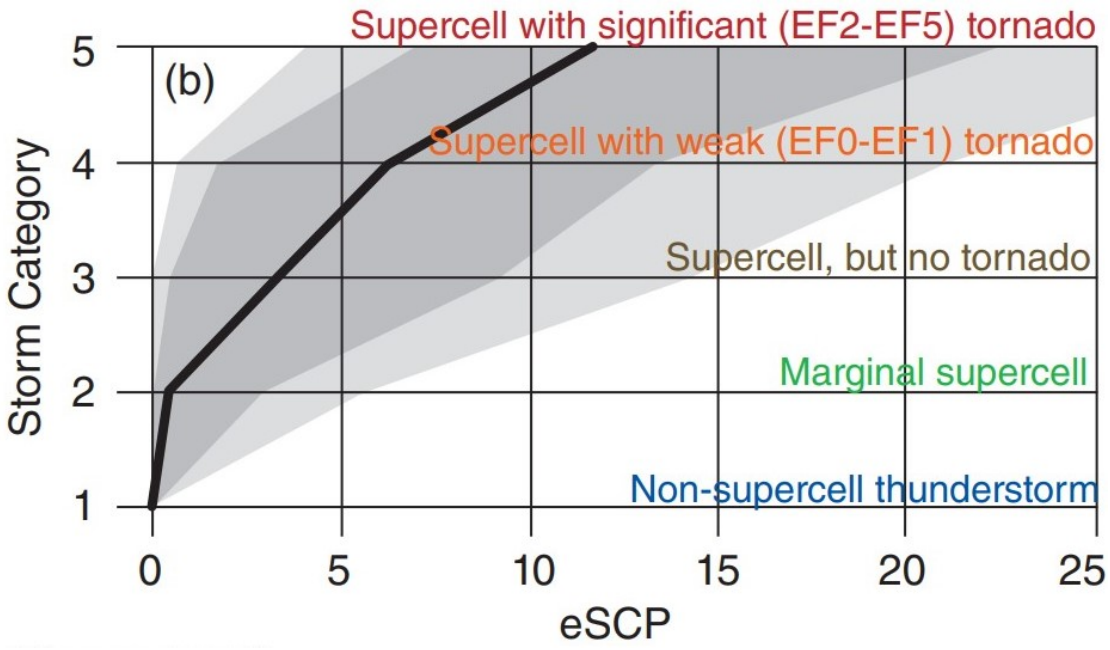

Figure 2.14: Diagram showing the statistics of the relation between the eSCP parameter, on the x-axis, and thunderstorm intensity, on the y-axis, over several hundreds of right-moving storms in North America. Source: Stull, Ronald B. Practical meteorology: an algebra-based survey of atmospheric science. University of British Columbia, 2015.

2.2.3 Weather radar

Weather radars are fundamental tools in meteorological observation and forecasting. These systems operate by detecting the backscattering of

electromagnetic waves caused by hydrometeors, allowing for the retrieval of critical informations regarding their spatial distribution and physical properties. A standard radar configuration comprises of a receiver and a transmitter, typically elevated to minimize ground-level interference, with the function of transmitting and receiving an electromagnetic signal through an antenna, and a radome to shield the instrument from bad weather. The antenna irradiates pulsed signals at a predetermined elevation angle while rotating azimuthally to achieve full 360° coverage. Once a complete rotation is executed, the elevation angle is incrementally adjusted, enabling a three-dimensional volumetric scan of the atmosphere. This systematic scanning strategy ensures comprehensive data collection for meteorological analysis. Weather radar frequencies, listed in Tab. 2.6, belong to the microwave range of the EM spectrum.

Table 2.6: Radar frequency bands and corresponding wavelengths

Band	**Frequency Range (GHz)**	**Wavelength Range (cm)**
L	1–2	30–15
S	2–4	15–7.5
C	4–8	7.5–3.75
X	8–12	3.75–2.5
Ku	12–18	2.5–1.67
K	18–27	1.67–1.11
Ka	27–40	1.11–0.75

Weather radars have traditionally transmitted and received only single-polarised waves, resulting in limited and incomplete information, especially regarding the type and composition of the scatterer. More recently, dual-polarisation weather radars have been introduced to enable the study of the composition of scatterers within the radar resolution volume and to

distinguish between hydrometeors and clutter, caused by reflections from non-meteorological objects, either natural or man-made, mostly located in a relatively close proximity of the radar [35].
The polarimetric variables obtained from a dual polarimetric radar consist of the Horizontal Reflectivity (Z_H) and of the Vertical Reflectivity (Z_V) factors, which are related to the backscattering properties of the particle such as shape and composition, the Differential Reflectivity (Z_{DR}) factor, which measures the difference between the two orthogonal backscattered signals, the Cross Correlation Coefficient (ρ_{hv}), which is influenced by the shape distribution of the hydrometeor; the Total Differential Phase (Φ_{DP}), the Specific Differential Phase (K_{DP}) and the Backscatter Differential Phase (δ) measure the effect of the EM wave phase shift produced by the scatterer, while the Linear Depolarisation Ratio (LDR) and Circular Depolarisation Ratio (CDR) measure the effect of the rotation of the polarisation plane by the scatterer. Finally, the Specific Attenuation ($A_{h,v}$) and the Specific Differential Attenuation (A_{DP}) are related to the propagation effects of the EM wave through a medium filled with hydrometeors.
Tab. 2.7 lists the system specifications of the two weather radars considered in this thesis, namely the Bric della Croce (TO, Piedmont, Italy) and Monte Settepani (SV, Liguria, Italy) weather radars.

Radar variables and derived products are visualized on horizontal or vertical maps. In this context, a Range-Height Indicator (RHI) map produces a vertical cross section of the radar analysed volume along a specific azimuth[4] angle for all elevation angles implemented in the radar

[4]The horizontal angular distance from a reference direction, usually the northern point of the horizon, to the point where a vertical circle through a celestial body intersects the horizon, usually measured clockwise.

Table 2.7: Comparison of system specifications between Monte Settepani and Bric della Croce weather radars

Parametro	**Bric della Croce (GPM250C)**	**Monte Settepani (Meteor400C)**
Radar type	Meteor 400C (Gematronik)	GPM 250C (Selex)
Polarization type	Simultaneous H and V	Alternate H and V
Antenna type	Central feed	Central feed
Antenna diameter	4.2 m	4.2 m
Beam width	1.0° (max., senza radome)	1.0° (max., senza radome)
Maximum sidelobe level	-28 dB	-28 dB
Maximum cross polar discrimination	-25 dB	-25 dB
Antenna gain	44.5 dB	44.5 dB
Radom type	Sandwich	Sandwich
Radome transmission loss	0.2 dB (max., one way)	0.2 dB (max., one way)
Transmitter type	Magnetron	Klystron
Frequency	5640 MHz	5625 MHz
Peak Power	250 kW	250 kW
Pulse length	0.5, 2.0 µs	0.5, 1.5, 3.0 µs
PRF (Pulse Repetition Frequency)	300 - 1200 Hz	300 - 1200 Hz
Range resolution	340 m (4 averaged samples)	375 m (5 averaged samples)

scan. A Constant Altitude Plane Position Indicator (CAPPI) map shows horizontal radar acquisitions at a constant altitude, extrapolating the values from a collection of Plane Position Indicator (PPI) at varying elevation angles. The latter ones are projections on a horizontal plane of a three-dimensional conical surface, representative of a complete atmospheric scan by means of the radar beam at a fixed elevation angle. As a consequence, the altitude of the return signal increases in proportion to the distance from the radar site.

Working principle Weather radars emit pulsed electromagnetic (EM) signals that propagate through space and time, carrying a power density stored in the form of oscillating electric ($\vec{\mathbf{E}}$) and magnetic ($\vec{\mathbf{H}}$) fields. By definition

$$\left|\vec{\mathbf{S}}\right| = \left|\vec{\mathbf{E}} \times \vec{\mathbf{H}}\right| = \frac{\left|\vec{\mathbf{E}}\right|^2}{\eta_0}, \tag{2.39}$$

which is further averaged over the pulse duration time to have a steady value

$$\overline{\left|\vec{\mathbf{S}}\right|} = \frac{1}{\eta_0 T_c} \int_0^{T_c} |\mathrm{Re}(\mathbf{E}(t))|^2 \mathrm{d}t = \frac{|\mathbf{E}|^2}{2\eta_0} \tag{2.40}$$

The signal from a conventional radar antenna does not propagate isotropically in space. Instead, the power is concentrated in a single "pencil beam" main lobe surrounded by many tiny side lobes. The gain (g) of the antenna defines the amount of power density carried by the main lobe relative to that of an isotropic radiator, and varies in space according to a Gaussian distribution, as a function of the beamwidths θ and ϕ, as shown in Fig. 2.15. Considering an horizontally polarized wave, the mean power density to hit a scatterer placed at a distance r from the radar can

therefore be expressed as

$$\overline{\left\|\vec{\mathbf{S}}^{i}_{hh}(r,\theta,\phi)\right\|} = \frac{P^{t}_{h}}{4\pi l_h(r) r^2} g\, f^2(\theta,\phi) \tag{2.41}$$

The fraction represents the average power density that an isotropic antenna would produce, corrected by the attenuation losses $l_h(r)$, whereas $g f^2(\theta,\phi)$ accounts for the spatial gain distribution of the beam. The object

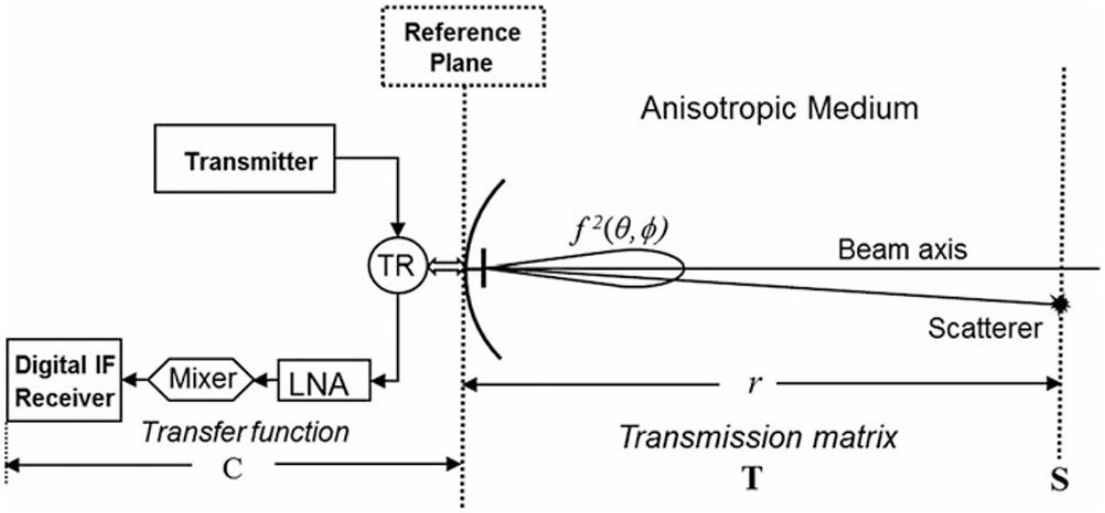

Figure 2.15: Simplified diagram of radar transmission and reception illustrating one transmitter and receiver of a dual-polarization radar. Source: Ryzhkov, Alexander V., and Dušan S. Zrnić. Radar polarimetry for weather observations. Vol. 486. Cham, Switzerland: Springer International Publishing, 2019.

absorbs part of the EM wave and reflects the rest in all directions. The fraction of the power returning to the radar defines the backscattered signal, which is directly proportional to the received EM wave through the Scattering Matrix (**S**), whose coefficients s_{mn} include the inherent electromagnetic scattering properties of hydrometeors. The power received by the radar is therefore computed as the product of the average backscattered power density times the effective area of the receiving antenna A_e, proportional

to its physical size, as

$$P_{hh}^{r} = \frac{|E_{hh}^{s}|^2}{2\eta_0} A_e = \frac{P_h^t g^2 \lambda^2 f^4(\theta,\phi)}{(4\pi)^2 r^4 l_h^2(r)} |s_{hh}|^2 \tag{2.42}$$

This equation holds true if a single hydrometeor is hit by the emitted pulse. The reality, though, is that the signal has a spatial width, defining the radar range resolution, along which many scatterers may potentially contribute to the backscattered signal. The introduction of a range weighting function and of a summation over the total number of hydrometeors illuminated simultaneously by the same pulsed EM wave inside the radar resolution volume, as depicted in Fig. 2.16, results in the weather radar equation:

$$\langle P_{hh} \rangle = \frac{P_h^t g^2 \lambda^2 c\tau\theta_1^2}{2^8 \pi r^2 l_h^2(r) l_r \ln 2} \langle |s_{hh}|^2 \rangle \tag{2.43}$$

where $< |s_{hh}|^2 >$ is the ensemble average representative of the scatterers, l_r are losses due to the application of the range weighting function and τ is the pulse duration. The equivalent reflectivity factor is introduced as

$$Z_{hh} = \frac{4\lambda^4}{\pi^4 |K_w|^2} < |s_{hh}|^2 >, \tag{2.44}$$

where K_w is a function of the dielectric constant of water ε_w. The standard form of the weather rada equation is then expressed as

$$P_{hh} = \left(\frac{\pi^3 P_h^t g^2 c\tau\theta_1^2}{2^{10} \ln 2 \lambda^2 l_r} \right) \frac{|K_w|^2}{r_0^2 l_h^2} Z_{hh} \tag{2.45}$$

The term within brackets is an absolute constant, depending on the radar

properties, and $|K_w|^2$ is used regardless of the type of scatterers in the radar resolution volume.

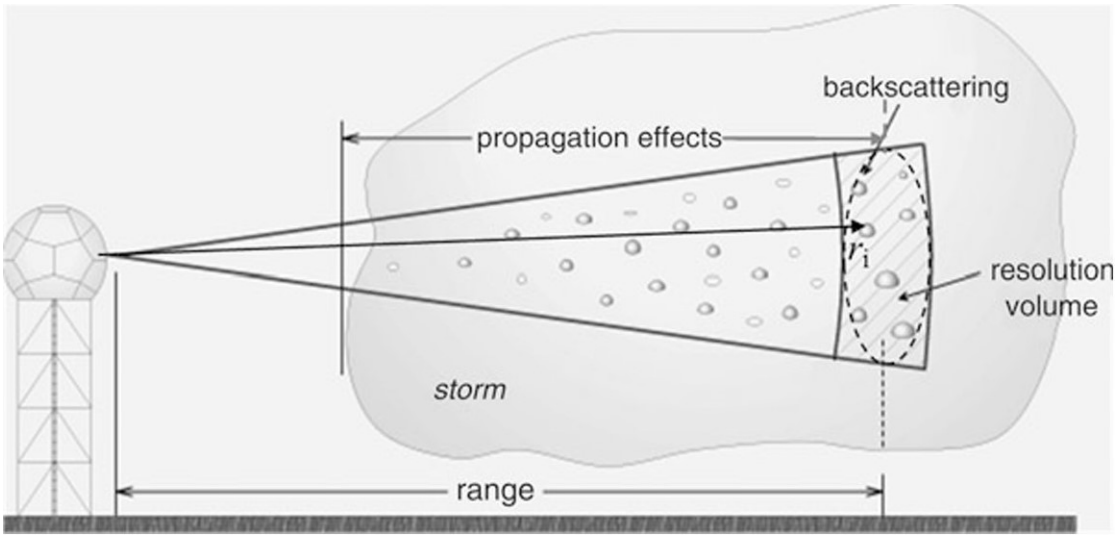

Figure 2.16: Scattering by an ensemble of hydrometeors illustrating propagation, backscattering, and resolution volume. Source: Ryzhkov, Alexander V., and Dušan S. Zrnić. Radar polarimetry for weather observations. Vol. 486. Cham, Switzerland: Springer International Publishing, 2019.

Reflectivity factor In the assumption of small hydrometeors, compared to the wavelength λ, having a spherical shape, the Rayleigh approximation can be adopted to compute analytically the backward scattering amplitudes, namely

$$s = \frac{\pi^2 D^3}{2\lambda^2} \frac{\varepsilon - 1}{\varepsilon + 2} \tag{2.46}$$

Substituting this formula in Eq. 2.44 for the case of raindrops gives the Equivalent Reflectivity Factor (Z)

$$Z = \int D^6 N(D)\, \mathrm{d}D \tag{2.47}$$

where $N(D)$ is the function describing the PSD and D is the diameter. Depending on the sixth power of the raindrop diameter, Z is mostly determined by the higher end of the raindrop spectrum. As an example, a single 5 mm raindrop produces the same reflectivity of a million 0.5 mm drops.

Reflectivity is an important parameter because it can be used to estimate the precipitation rate. In fact, an empirical relationship can be established between Z and the precipitation rate (R), which, from simple geometric considerations, can be expressed as

$$R \sim \int D^{3.67} N(D)\, dD. \tag{2.48}$$

There are many empirical $Z(R)$ relations, each depending on the type and location of the event observed, the most common being the Marshall-Palmer relation [17]. ARPA Piemonte adopts the following relation:

$$Z = 300R^{1.5} \tag{2.49}$$

where R is in $\mathrm{mm\,h^{-1}}$ and Z in linear units ($\mathrm{mm^6/m^3}$), despite reflectivity being normally expressed in dBZ units by further normalizing Z by $1\,\mathrm{mm^6/m^3}$ and taking 10 times the $\log_{10}$.

Tab. 2.8 illustrates the conversion table between reflectivity factor (in dBZ) and rainfaill rate (in $\mathrm{mm\,h^{-1}}$) obtained from Eq. 2.49. $Z(R)$ relations strongly depend on the shape of the hydrometeors distribution and therefore should be used only as a first approximation to rainfall rate.

Table 2.8: Classification of precipitation intensity based on the R(Z) relationship adopted by ARPA Piemonte; Z is the radar reflectivity (dBZ) and R stands for rainfall rate (mm/h).

Reflectivity (dBZ)	**Rainfall Rate (mm/h)**	**Intensity**
<10	<0.1	Absent/Negligible
10–20	0.1–0.5	Very light
20–35	0.5–5	Light
35–45	5–22	Moderate
45–55	22–103	Heavy
>55	>103	Very heavy

2.3 Statistical tools

This section provides a theorical overview of the statistical tools adopted in this thesis, i.e. the Fraction Skill Score (FSS) and the Particle IDentification (PID) algorithm. The first represents the score adopted for the verification stage, whereas the second refers to the post-processing of radar data for the purpose of hydrometeor classification.

2.3.1 Fractions Skill Score

The FSS is a member of the NeighbOurhood-NeighbOurhood (NO-NO) fuzzy verification framework, therefore constituting a post-processing tool for assessing the probability of detection of a 2D spatial pattern in a deterministic forecast. It represents a simple alternative to the more expensive approach of running ensemble forecasts. The method operates by comparing the frequency distribution of events within predefined neighborhoods across both model-predicted and observed fields, assessing the spatial probability of detection through a skill score metric that ranges from 0 (no skill) to 1 (perfect forecast). The neighborhood size in the

FSS method is defined by square boxes whose dimensions range from a single grid cell (equivalent to point-to-point comparison) to the entire model domain. As expected, the skill score typically increases with larger neighborhood sizes, reflecting greater spatial tolerance in the verification process. In this study, we employ the FSS to quantitatively assess the model's ability to reproduce observed precipitation patterns, with particular focus on convective systems detected by weather radar. Furthermore, this approach helps identify the optimal spatial scale for presenting model outputs, balancing between resolution accuracy and predictive skill.

Description of the method The first step towards computing the forecast skill is to match the resolution grid of the radar to that of the model, in order to allow for a reasonable comparison between the two [36]. The spatially discretised precipitation fields are then converted into binary form using a threshold-based filtering technique. Cell values (O_r) below the threshold (q) are set to zero, while those above are set to one. This discretization process repeated for different threshold values, although resulting in a loss of informations about precipitation intensity, is consistent with the interest of FSS in detecting spatial patterns rather than intensity levels. The result of the filtering process is illustrated in Fig. 2.17 for the forecast (left) and radar (right) fields, where grey and white boxes indicate the presence and absence of precipitation, respectively. With Fig. 2.17 still in mind, the next step is to obtain the fraction of cells containing precipitation with respect to the total number of cells in the box. This fraction, having fixed a cell in the domain, depends on the length of the square box n and on the selected threshold, as shown here for the forecast field:

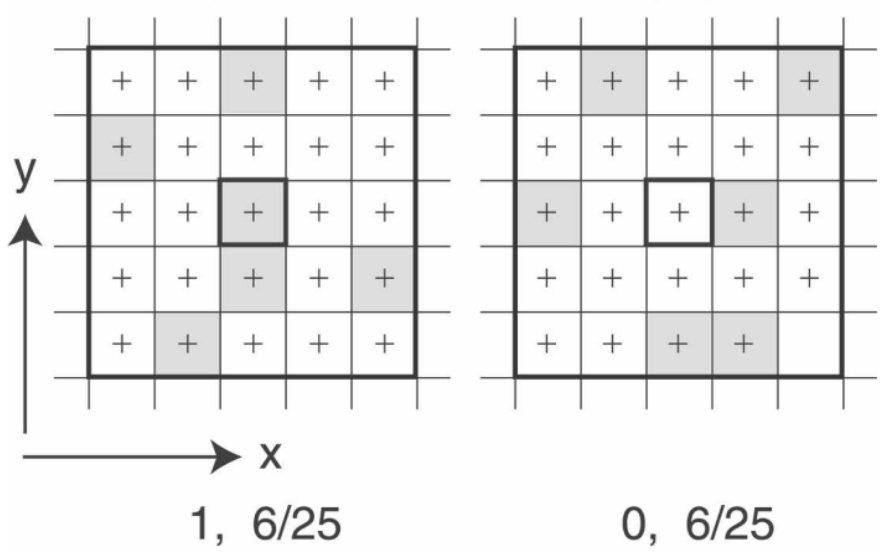

Figure 2.17: Schematic example of radar (left) and forecast (right) fractions obtained when applying the FSS method, which involves discretization of the domain of interest and filtering of the analysed quantity based on a threshold. Source: Roberts, Nigel M., and Humphrey W. Lean. "Scale-selective verification of rainfall accumulations from high-resolution forecasts of convective events." Monthly Weather Review 136.1 (2008): 78-97.

$$O(n)(i,j) = \frac{1}{n^2} \sum_{k=1}^{n} \sum_{l=1}^{n} I_O \left[i + k - 1 - \frac{n-1}{2}, j + l - 1 - \frac{n-1}{2} \right] \tag{2.50}$$

$$I_O = \begin{cases} 1 & \text{se } O_r \geq q \\ 0 & \text{se } O_r < q \end{cases} \tag{2.51}$$

The same procedure, applied to the observed field, produces the fraction $M(n)(i,j)$. Computing the Mean Squared Error (MSE) between these

two fractions, namely

$$MSE_{(n)} = \frac{1}{N_x N_y} \sum_{i=1}^{N_x} \sum_{j=1}^{N_y} \left[O_{(n)i,j} - M_{(n)i,j} \right]^2 . \tag{2.52}$$

produces a skill dependent on the frequency of the event. The MSE is further normalised with its reference value represented by the worst case scenario,

$$MSE_{(n)ref} = \frac{1}{N_x N_y} \left[\sum_{i=1}^{N_x} \sum_{j=1}^{N_y} O^2_{(n)i,j} + \sum_{i=1}^{N_x} \sum_{j=1}^{N_y} M^2_{(n)i,j} \right] . \tag{2.53}$$

to finally obtain the FSS:

$$FSS_{(n)} = 1 - \frac{MSE_{(n)}}{MSE_{(n)ref}} \tag{2.54}$$

The analysis implements two different approaches. The first, designated 2D fuzzy, compares the forecast and observation (radar) 3-hours precipitation fields. The second implementation, the 3D fuzzy, incorporates the variable 'time' into the analysis by comparing the observation field to the previous and next three-hour forecast fields. This extended temporal window reduces sensitivity to exact timing whilst capturing the spatial organisation of precipitation systems more effectively. By plotting the FSS value as a function of the neighbourhood dimension n, as shown in Fig. 2.18, we can identify a range of scales where the simulation can be considered reliable and the results can be presented with a certain degree of precision. Below this range, the prediction skill is no better than that of a random forecast; above it, the information is too smoothed to be useful.

Useful scale numbers are marked in bold on the FSS plot.

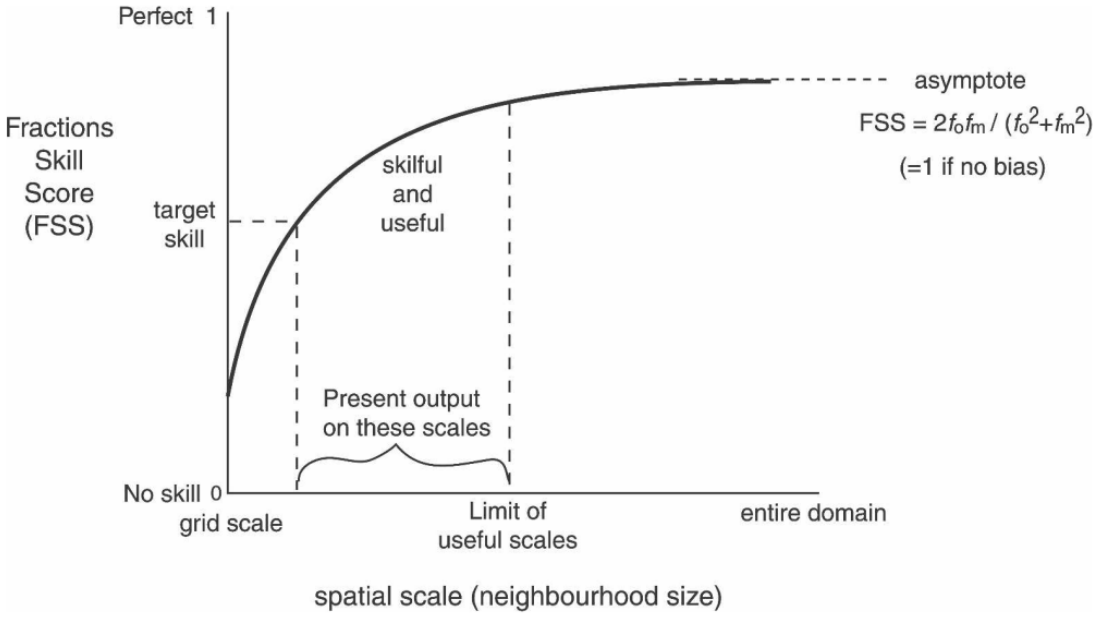

Figure 2.18: Schematic graph of FSS value against spatial scale. Increasing the latter, the skill increases until an asymptote is reached. Source: Roberts, Nigel M., and Humphrey W. Lean. "Scale-selective verification of rainfall accumulations from high-resolution forecasts of convective events." Monthly Weather Review 136.1 (2008): 78-97.

2.3.2 Bias and Root Mean Squared Error

The bias is a statistical measure that quantifies the average discrepancy between a model's predictions and the corresponding observations. A high bias indicates systematic errors in the model, reflecting a consistent tendency to either overestimate or underestimate the observed values. Mathematically, bias is defined as the mean difference between simulated

and observed values over the total number of data points:

$$bias = \frac{1}{N}\sum_{i=1}^{N}(y_{sim,i} - y_{obs,i}) \tag{2.55}$$

where N is the total number of observations, $y_{obs,i}$ is the observed value at point i and $y_{sim,i}$ is the simulated (predicted) value at point i.

For a comprehensive model assessment, bias is typically analyzed alongside the Root Mean Squared Error (RMSE), a widely used metric for evaluating point-to-point accuracy. The RMSE quantifies the standard deviation of prediction errors, providing insight into the overall deviation between simulated and observed data. Its formulation is given by:

$$RMSE = \sqrt{\frac{1}{N}\sum_{i=1}^{N}(y_{sim,i} - y_{obs,i})^2} \tag{2.56}$$

Since RMSE squares the errors, it is particularly sensitive to outliers, meaning that a high RMSE indicates poor model precision. Similarly to bias, RMSE is scale-dependent, making comparisons across different variables problematic without normalization. A low RMSE with a non-zero bias suggests that the model's errors are consistent but systematically offset, implying that calibration (e.g., via bias correction) could improve accuracy. A high RMSE with low bias indicates high variability in errors, meaning the model may fit the data on average but with large deviations in individual predictions, potentially due to random noise or model inadequacy. This combined analysis helps distinguish between structural model deficiencies, bias, and stochastic or localized inaccuracies, RMSE, guiding further refinements in model development.

2.3.3 Particle Identification

PID is a technique used to classify hydrometeors by analyzing dual-polarimetric radar measurements, which are sensitive to particle type, shape, size distribution, and fall behavior within the radar resolution volume. This method combines polarimetric observations, including Z_H, Z_{DR}, K_{DP} and ρ_{hv}. The classification algorithm used in this study can identify ten hydrometeor types: large drops, drizzle, rain, heavy rain, rain-hail mixtures, hail, graupel, wet snow, dry snow, and ice crystals. Non-meteorological echoes, such as ground clutter, clear-air returns, noise, and unclassified signals, are also detected to ensure accurate cloud analysis. Each polarimetric variable is linked to a specific hydrometeor class through a MemBership Function (MBF), described by an asymmetric distribution function, which quantifies the likelihood of a given measurement belonging to a particular class on a scale from 0 to 1. For example, rain exhibits a wide range of reflectivity values, resulting in a broad MBF for Z_H that remains high across most observed intensities but decreases sharply above 60 dBZ, where hail becomes the dominant species. The algorithm employs fuzzy logic, a framework well-suited for handling overlapping classifications and noisy radar data due to its robustness and computational efficiency. As depicted in Fig. 2.19, the process consists of four key stages [37]. The first step towards the implementation of the PID algorithm is the fuzzification of the data set, where raw polarimetric inputs are transformed into fuzzy sets using predefined MBF. To reduce measurement noise, all radar variables are averaged over a window of three beams and three range gates in the polar volume. The rule inference step is then applied, whereby each fuzzy set is assigned a probability of belonging to different hydrometeor classes based on logical rules. The adopted inference rule is

the product of the temperature MBF and the weighted sum of the MBF of the aforementioned radar parameters [38]

$$P_T = MBF(T) \cdot \frac{\sum_i^N [w(x_i) \cdot MBF(x_i)]}{\sum_i^N w(x_i)} \tag{2.57}$$

where $N = 4$, x_i are the radar parameters, $w(x_i)$ are the weights associated with each radar parameter and T is the temperature derived from either sounding or model. In the aggregation step the results from multiple rules are combined using the maximum aggregation method to produce a composite fuzzy output and, finally, the last step is defuzzification, which converts the aggregated fuzzy set into a definitive hydrometeor classification.

2.4 Methodology

To evaluate the optimal microphysical representation for the convective system under investigation, a comparative analysis of ICON single- and double-moment bulk schemes against radar observations has been conducted. For each microphysics configuration, twin experiments are performed: a baseline simulation and a second run incorporating LHN. The two simulations used the same model parameters; the only difference between them was the activation of the LHN.

Predictive skill assessment of ICON simulations To assess the model's predictive capability, two complementary analytical approaches were performed on the output data from the four simulations. The first analysis focused on verifying the spatial and temporal patterns of precipitation,

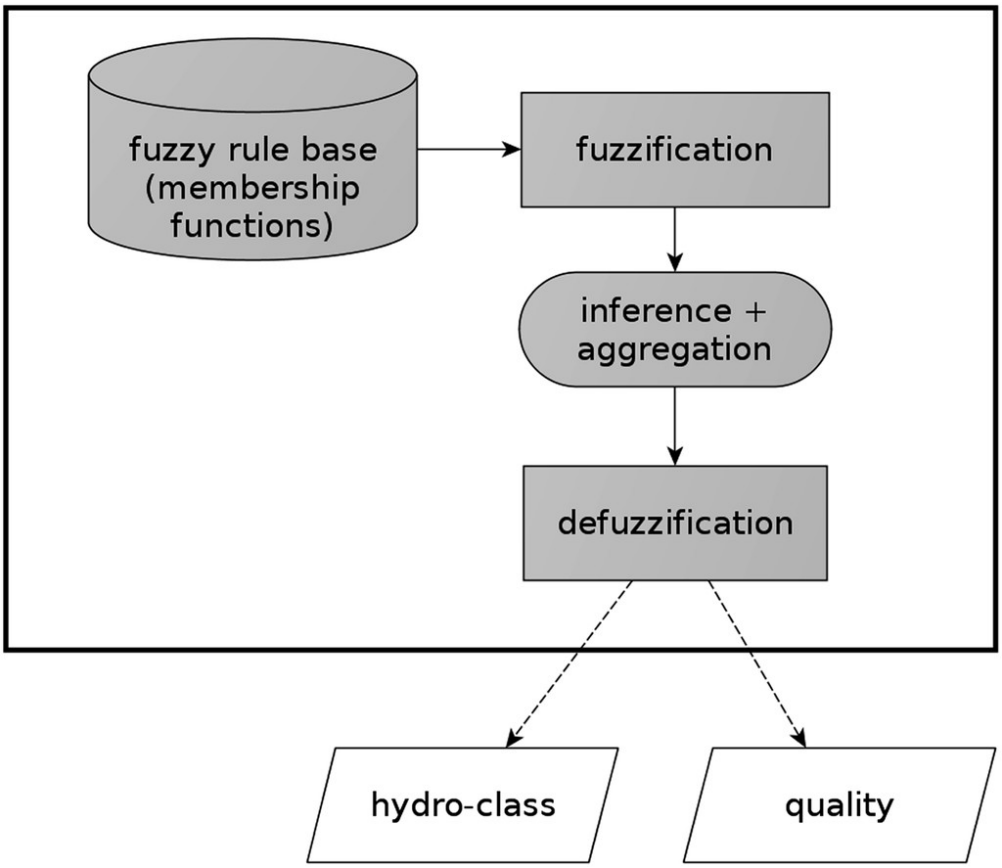

Figure 2.19: Block diagram of the fuzzy logic PID control system. Source: Journal of Atmospheric and Oceanic Technology 32, 1; 10.1175/JTECH-D-14-00097.1

including hail, and radar reflectivity fields over Northern Italy through a two-stage verification process. Initial qualitative evaluation involved visual comparison between model outputs and observations, examining the morphological characteristics of convective structures. This was followed by quantitative fuzzy verification using the FSS method on the precipitation field, which objectively evaluates forecast skill by accounting for both displacement and intensity errors across multiple spatial scales. The observed precipitation data were derived from radar polarimetric variables using the operational $R(Z)$ relationship adopted by the Italian Department

of Civil Protection, subsequently adjusted using rain gauge measurements to reduce potential biases. Regarding simulated reflectivity, this was diagnostically calculated from prognostic hydrometeor concentrations using the Efficient Modular VOlume scan RADar Operator (EMVORADO) [39]. Reflectivity of hail is simulated by adopting look-up tables, provided by EMVORADO, directly relating Z and the radar wavelenght λ to the prognostic model variables, instead of the more computationally expensive but precise Mie theory, with degraded performances regarding especially ice melting processes [40]. Melted hail is treated as a two-layered sphere, composed of ice in the inside and water on the outside. Tab. 2.9 lists the assumtpions made by EMVORADO regarding composition and shape of all hydrometeor's classes.

Table 2.9: Particle composition and morphology in EMVORADO

Class	**Composition**	**Morphology**
Cloud water	H_2O	Sphere
Rain	H_2O	Sphere
Dry ice	Ice + air	Sphere
Dry snow	Ice + air	2-layer (dense core)
Dry graupel	Ice + air	Sphere
Dry hail	Ice + air	Sphere
Wet ice	Ice + air + H_2O	Soaked
Wet snow	Ice + air + H_2O	Soaked 2-layer
Wet graupel	Ice + air + H_2O	Soaked (2-layer ice/water or water)
Wet hail	Ice + H_2O	2-layer ice + wet

In parallel with the spatial analysis, a quantitative point-by-point validation of surface thermodynamic variables was conducted. Observational data where acquired from the network of ground weather stations operated by ARPA Piemonte that recorded the event. Particular attention was paid to air temperature, relative humidity, wind speed and direction, and accumulated precipitation. To ensure statistical robustness of the results, performance metrics such as bias and RMSE were computed while excluding null-value pairs between observations and simulations, thereby avoiding artificial inflation of the model's predictive skill. Furthermore, a minimum threshold of 1 mm was applied to observed precipitation to account for instrumental sensitivity of rain gauges and exclude negligible accumulations. For a more comprehensive evaluation of the atmospheric thermodynamic structure, a comparison between simulated and observed vertical profiles was performed using radiosonde data. Specifically, the SLE, LIMN and SPC stations were analyzed by interpreting SkewT-logP diagrams and calculating key instability indices, including CAPE, CIN, EBWD, and ESRH. This multi-level approach allowed assessment of not only the model's surface performance but also its ability to properly reproduce the vertical atmospheric structure, which is crucial for convective processes.

Microphysical analysis The core analysis of this thesis evaluates the performance of single- and double-moment microphysics parameterization schemes implemented in ICON in reproducing the microphysical and polarimetric signatures of supercell thunderstorms. Validation relies on polarimetric radar observations from the Bric della Croce and Monte Settepani weather radars. To ensure a systematic comparison, only the optimal configuration for each microphysics scheme, identified in the

previous analysis, is considered. The study area is restricted to northern Italy, with a focus on the region during the most intense phase of thunderstorm development, which is characterised by heavy precipitation over a large area. A detailed examination of storm structure and microphysical composition is conducted through vertical cross-sections of reflectivity and hydrometeor mixing ratios. The cross-section is strategically positioned near the updraft region, where the most severe convective activity typically occurs, allowing for an in-depth analysis of kinematic and microphysical processes. To precisely define the location of the vertical cross-section, the updraft region must first be identified. For observational data, this is achieved through qualitative analysis of CAPPI images at 2, 3, and 5 km altitudes. In the simulations, however, a more objective approach is employed, leveraging the vertical velocity profile of the updraft. The updraft's kinematic evolution follows a well-defined pattern: during initial ascent, vertical velocity increases due to buoyancy-driven acceleration until reaching a peak, after which deceleration occurs due to entrainment of dry air and stabilization relative to the surrounding environment. Consequently, the vertical velocity profile exhibits a distinct maximum, marking the most dynamically active portion of the updraft. To isolate this region in the simulations, horizontal cross-sections of vertical velocity are analyzed at the model level corresponding to the observed peak updraft intensity. This method provides a robust spatial reference for positioning the vertical cross-section, ensuring alignment with the core of convective activity.

The simulated reflectivity cross-section is compared against an observational reference obtained by intersecting a 3D radar volume composed of stacked CAPPI reflectivity products from the Monte Settepani radar.

This volume integrates successive CAPPI planes extracted at increasing altitudes, spanning from ground level to 19 km - the maximum detection altitude where the radar's highest elevation beam (19.5°) sampled the supercell structure. The vertical cross-section is then derived by sectioning this composite volume along the analysis plane. A distinct analytical approach is required for hydrometeor distributions. While the model explicitly resolves hydrometeor mixing ratios, the comparison focuses solely on their spatial distribution and typology, due to the inability of weather radars to provide direct quantitative measurements of hydrometeor concentrations. Nevertheless, polarimetric radar enable hydrometeor classification via dedicated algorithms. The implemented approach builds upon the framework established by [37], while incorporating additional hydrometeor classes to enhance discrimination capabilities. This methodology enables robust qualitative comparison of hydrometeor types between simulated and observed storm structures.

Chapter 3

Results and discussion

3.1 Predictive skill assessment of ICON simulations

3.1.1 Precipitation fields

Precipitation forecasting is arguably one of the most challenging tasks for a NWP model, as it relies on parameterizations to represent the nonlinear subgrid-scale processes that govern the formation and growth of hydrometeors. Consequently, there will inevitably be some degree of spatiotemporal and quantitative discrepancy between model outputs and observations. To illustrate this issue more clearly, we analyze 24-hour accumulated precipitation fields over a large area of northern Italy. In Fig. 3.1, IC1M and IC2M simulations are directly compared against observational data to enable a clear visual assessment of their performance. This comparison reveals a systematic overestimation of precipitation intensity by the single-moment microphysics scheme, particularly in regions where the model correctly captured precipitation events. Exemples

of this include the border between Liguria and France in southern Emilia-Romagna. A similar overestimation occurs in the Northeast, where thunderstorms are triggered by a weak frontal system descending from the Alps, as is later confirmed by radar analysis. Although IC2M produces spatial patterns similar to those of IC1M, it is better at capturing the observed intensity of precipitation events, including the daily precipitation peak of 150 mm. The models appear to displace the main bulk of precipitation observed in Piedmont, which is primarily associated with supercell activity, to the east. This results in two distinct high-intensity precipitation bands across the provinces of Milano, Bergamo, and Verona, which are indicative of intense convective processes in both simulations. However, IC1M produces more extensive and continuous precipitation bands than IC2M, which generates more localised structures. Another notable feature is that the IC1M model produces fewer widespread regions of light precipitation than IC2M, which is likely due to its low sensitivity to minor precipitation thresholds. IC2M shows a modest improvement in this regard, capturing the light rainfall typically associated with the tail of downdrafts more effectively. The patterns simulated by both models over the Piedmont region (Italy) stem from a multicellular thunderstorm complex that originated at approximately 1800 UTC. For this reason, they are unrelated to the supercell. The failure of both microphysical schemes to properly capture the supercell-induced precipitation suggests that there are fundamental limitations to this modeling approach. This poor performance may be attributed, at least in part, to the absence of assimilated data within the Planetary Boundary Layer (PBL). Such a data deficiency could significantly compromise the model's ability to accurately represent the essential triggering mechanisms for deep convection development.

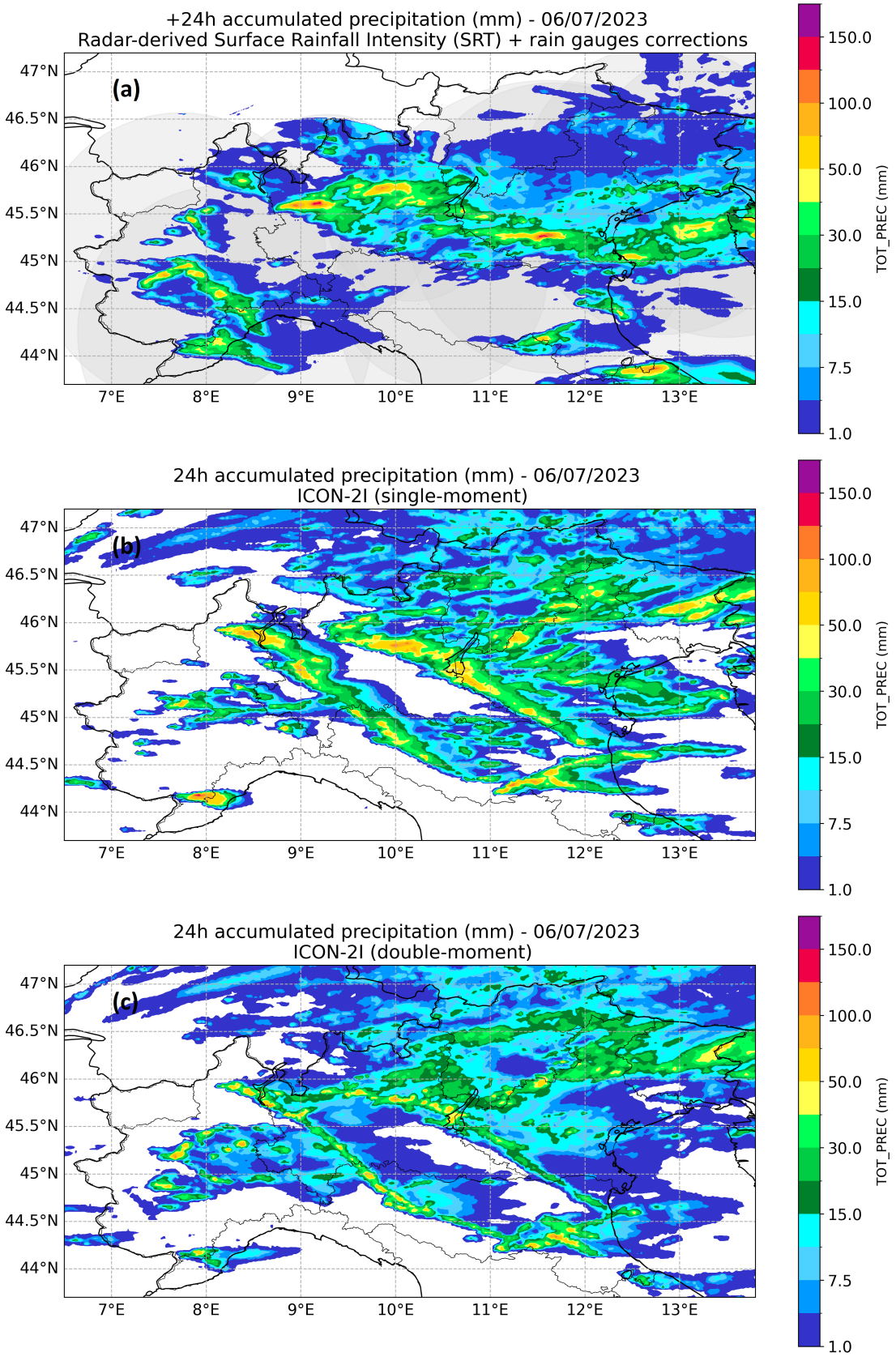

Figure 3.1: 24-hours accumulated precipitation from (a) radar observations, (b) IC1M and (c) IC2M on July 6, 2023. The grey circles in the top image represent the domains covered by radars used to generate the composite.

Introducing LHN significantly improves the model's ability to forecast precipitation. The IC1M-LHN and IC2M-LHN simulations both produce precipitation patterns that align well with observations across the radar-covered regions shown in Fig. 3.2. Although the elongated precipitation bands present in earlier simulations have been suppressed, the precipitation patterns remain widespread and are consistent with the observed intense convective activity.

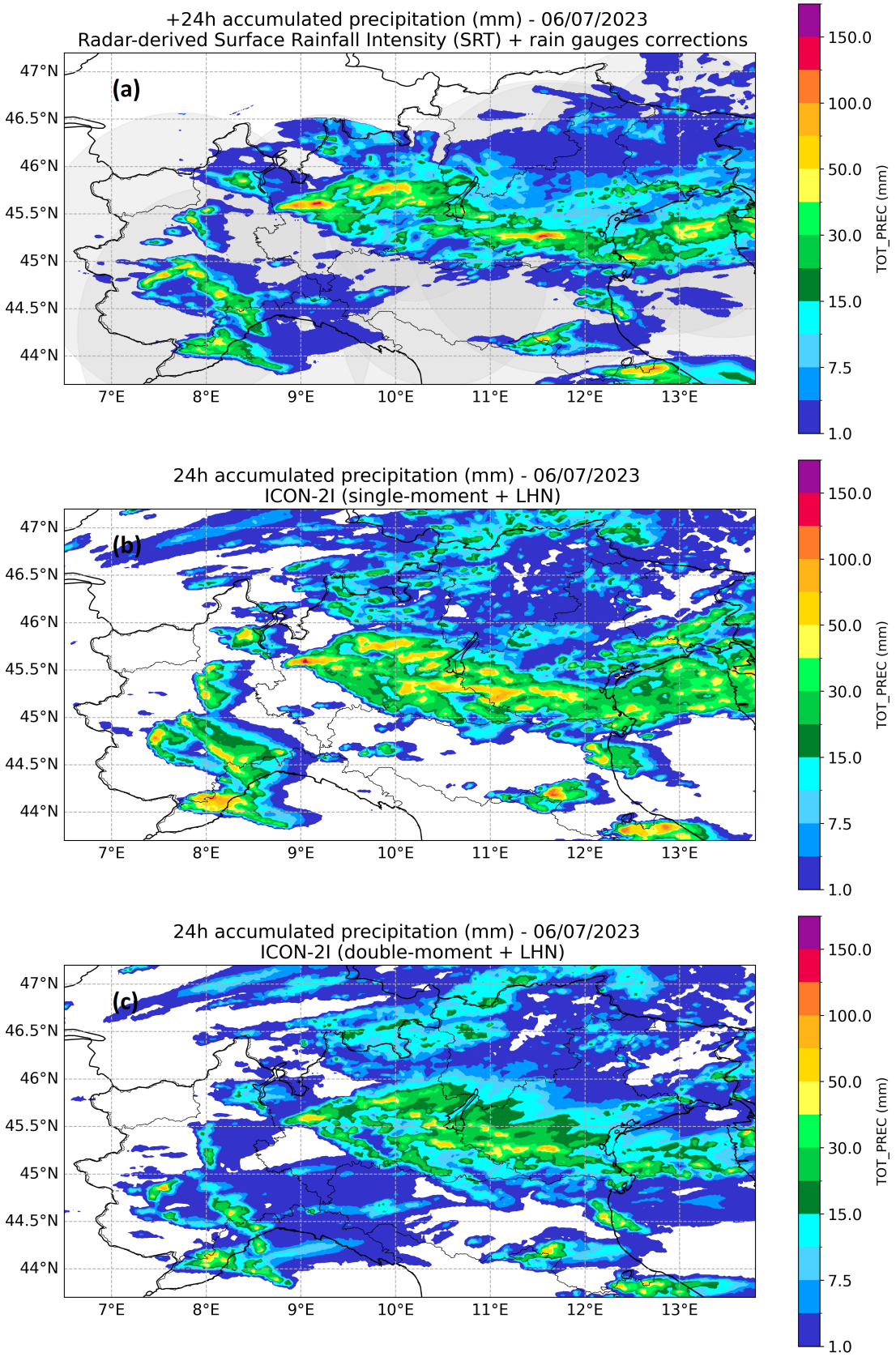

Figure 3.2: 24-hours accumulated precipitation from (a) radar observations, (b) IC1M and (c) IC2M on July 6, 2023. The grey circles in the top image represent the domains covered by radars used to generate the composite.

Compared to IC2M-LHN, IC1M-LHN persistently overestimates precipitation intensity and struggles to adequately represent the spectrum of small raindrops, particularly in the previously identified regions. Precipitation fields obtained with LHN achieve a reasonable degree of spatial correspondence between observed and simulated thunderstorms, enabling a direct comparison of storm morphology and intensity, particularly in the case of the supercell. Fig. 3.3 compares the hourly precipitation evolution of the observed supercell, from 1100 UTC to 1400 UTC with that simulated by IC1M-LHN, providing insight into the model's temporal accuracy. During the mature phase of the supercell (1300 UTC), IC1M-LHN shows good agreement with the observations by correctly locating the precipitation core geographically, although it slightly underestimates its intensity. The feature of the single-moment scheme that overestimates precipitation intensity, which has been previously observed, becomes particularly evident during the supercell's occlusion and dissipation phases, which occurs around 1400 UTC.

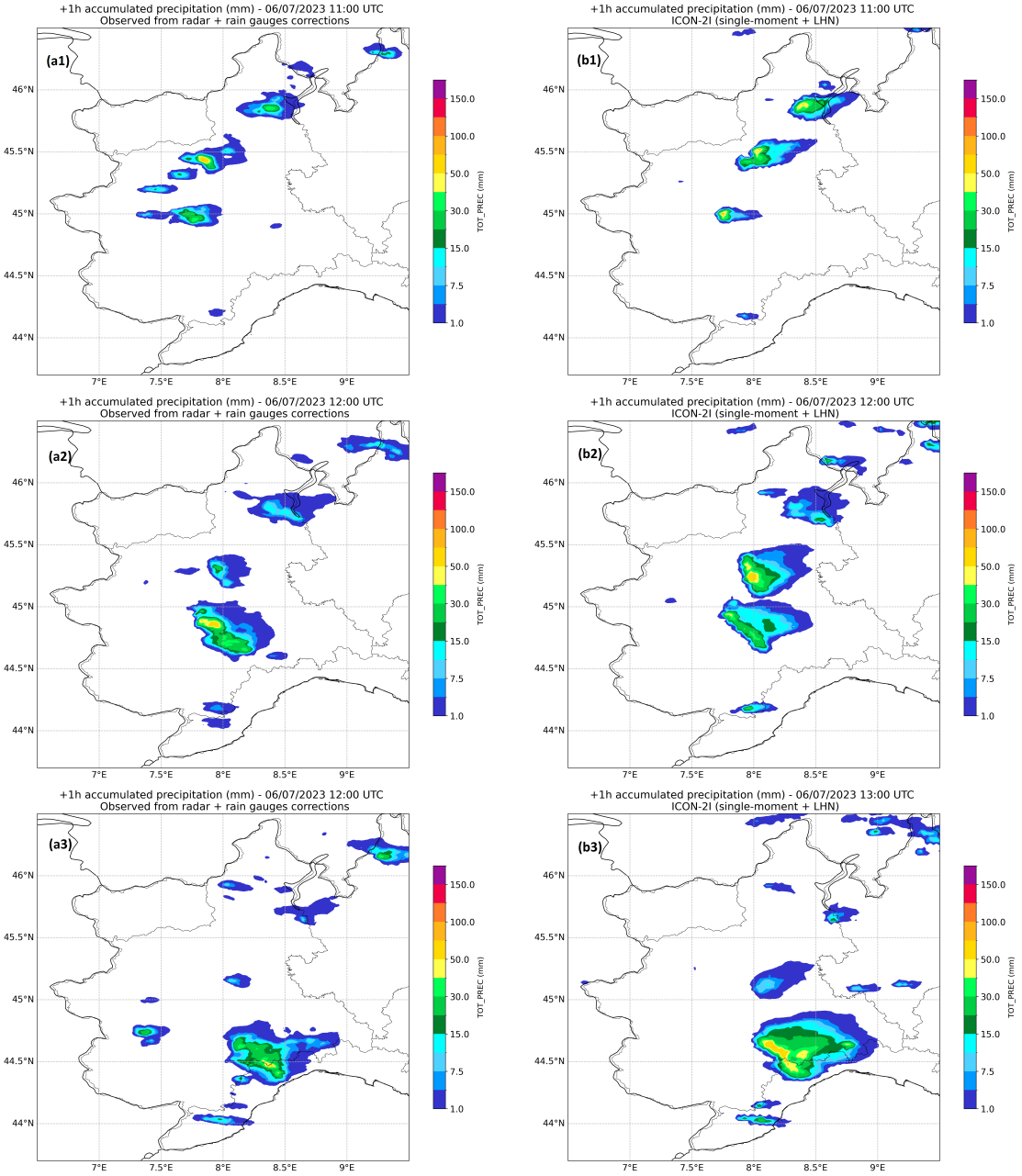

Figure 3.3: 1-hour accumulated precipitation over the Piedmont region (Italy) obtained from (a) Composite of Bric della Croce and Monte Settepani weather radars and (b) IC1M-LHN and between (1) 1100 UTC and 1200 UTC, (2) 1200 UTC and 1300 UTC and (3) 1300 UTC and 1400 UTC.

The hourly precipitation patterns produced by IC2M-LHN in Fig.

3.4 exhibit a southward displacement compared to the observations, particularly during the initial stages of supercell development. Given the supercell's NW-SE trajectory, this could suggest a delayed response to the LHN in the double-moment scheme. However, as the thunderstorm approaches the Ligurian border, IC2M-LHN more accurately captures the position and spatial extent of the high-intensity precipitation core than IC1M-LHN does. Furthermore, IC2M-LHN predicts an elongated region of light precipitation extending downwind of the supercell without an observed counterpart.

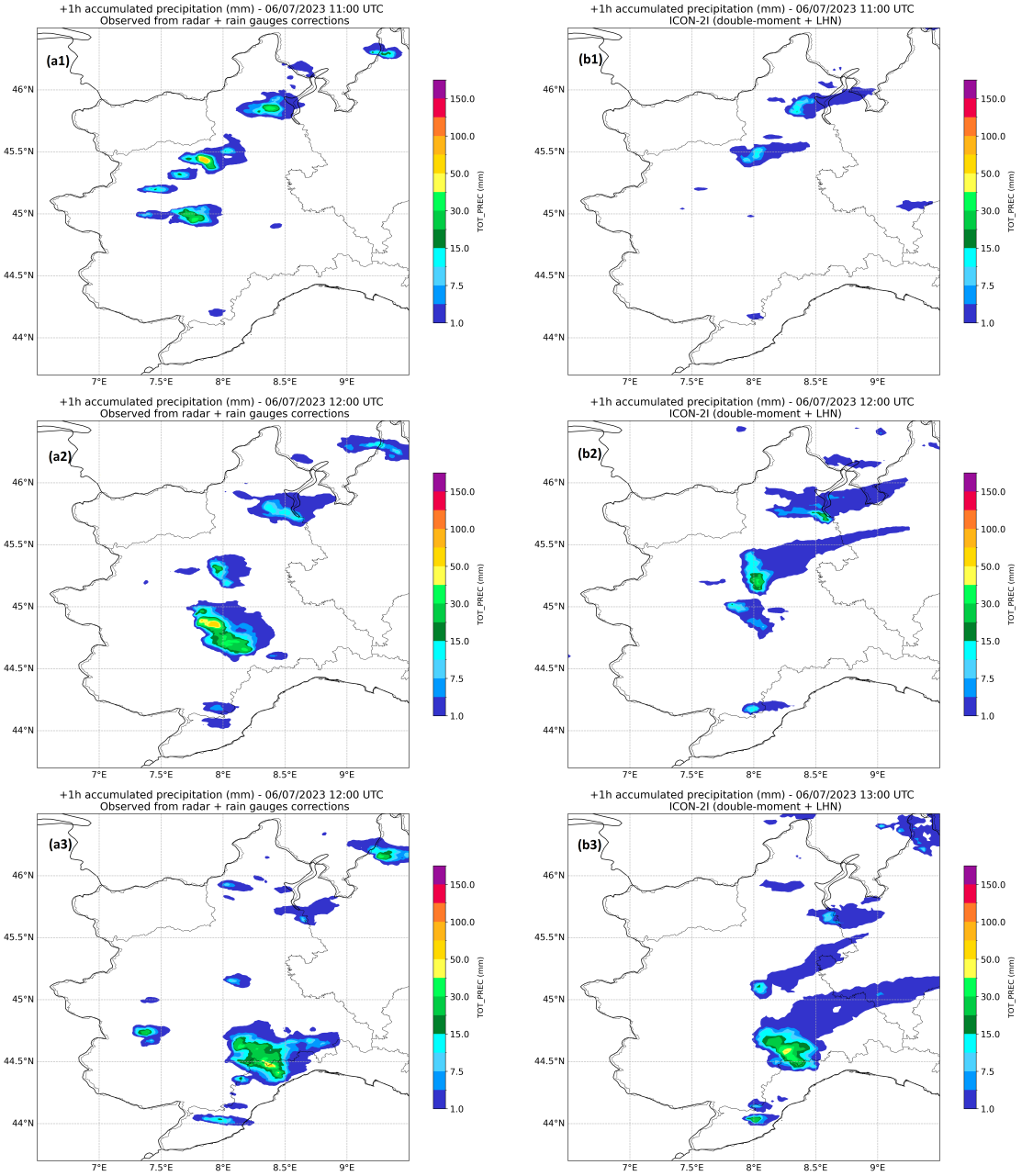

Figure 3.4: 1-hour accumulated precipitation over the Piedmont region (Italy) obtained from (a) Composite of Bric della Croce and Monte Settepani weather radars and (b) IC2M-LHN between (1) 1100 UTC and 1200 UTC, (2) 1200 UTC and 1300 UTC and (3) 1300 UTC and 1400 UTC.

A performance of the model was assessed quantitatively by comparing

the amount of precipitation accumulated over a 24-hours period along a transect line aligned with the supercell's trajectory, as shown in Fig. 3.5. By doing so, the developing stages of the supercell are also captured. As anticipated, the model runs without assimilation fail to simulate any precipitation, as they missed the supercell entirely. The comparison reveals distinct behavioral differences between the assimilated runs. During the early phase of storm development (the left portion of the transect), IC1M-LHN outperforms IC2M-LHN, confirming the slower response of the double-moment scheme to LHN adjustments. While IC1M-LHN correctly positions the maximum precipitation, it overestimates its severity by approximately 30 mm.

Despite the accumulated precipitation profiles showing good model-observed correspondence overall,

both schemes fail to capture the observed reduction in precipitation between 44.65°N and 44.58°N. The double-moment scheme produces its most significant accumulations during the later stages of the supercell, concurrently with the production of hail, as described in Section 3.1.2.

3.1.2 Hail

Hail production is a crucial metric for evaluating the microphysics schemes of convection-permitting models. The presence of large hailstones in the observed supercell has been confirmed through eyewitness reports, reports from trained storm spotters, and photographic or video evidence of the event and the resulting damage. Our model outputs of hail surface density (in $\mathrm{kg\,m^{-2}}$) are every 10 minutes (Tab. 2.4). Fig. 3.6 shows the locations of observed hail (green triangles), and heavy rain (blue dots) superimposed on the 24-hour accumulated hail produced by the IC2M and IC2M-LHN

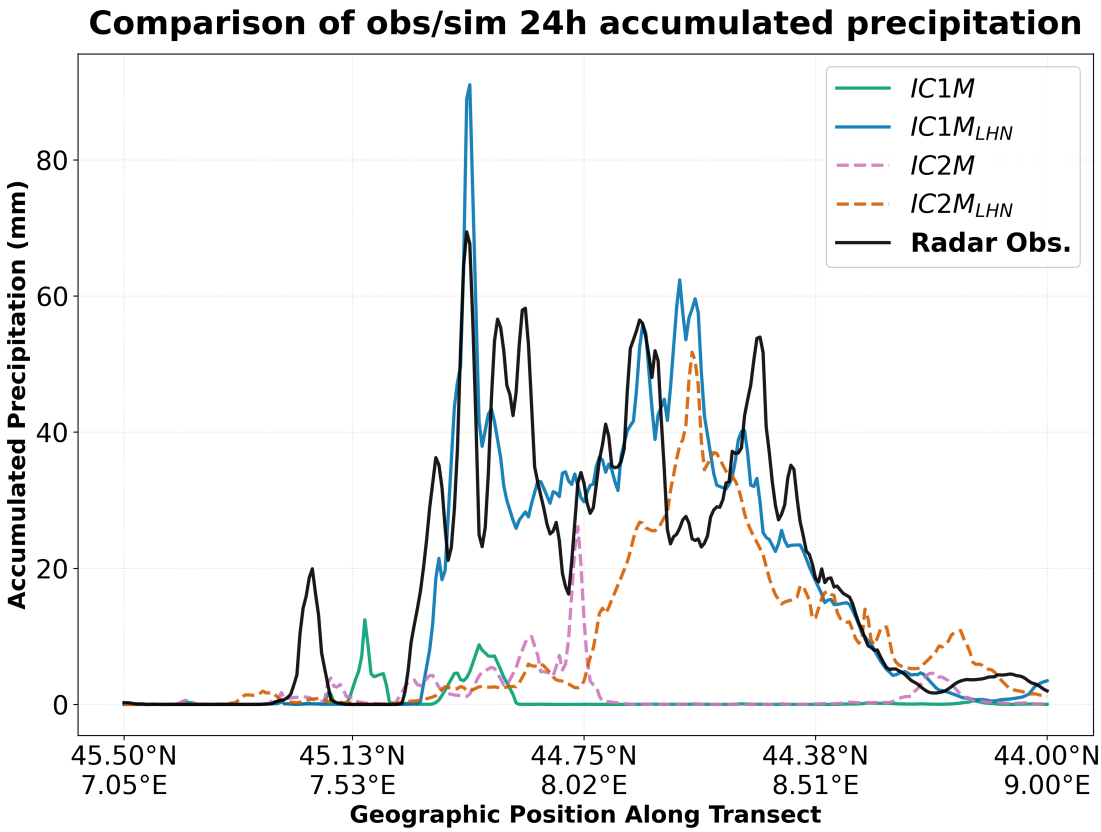

Figure 3.5: Comparison between radar-derived, IC1M, IC2M, IC1M-LHN and IC2M-LHN 24-hour accumulated precipitation (mm) along a transect line drawn by following the path of the supercell under investigation.

simulations. The following analysis is restricted to assessing the accuracy of the simulations in estimating the location of hail production since a quantitative comparison is unfeasible due to a lack of extensive in-field measurements.

The IC2M simulation produces hail bands that mirror the precipitation patterns shown earlier. Extensive areas show hail surface density values exceeding 50 kg m^{-2} distributed broadly across northern Italy, particularly in the Lombardia region and to the west of Piedmont, Italy. These zones of high hail accumulation correspond geographically to the locations

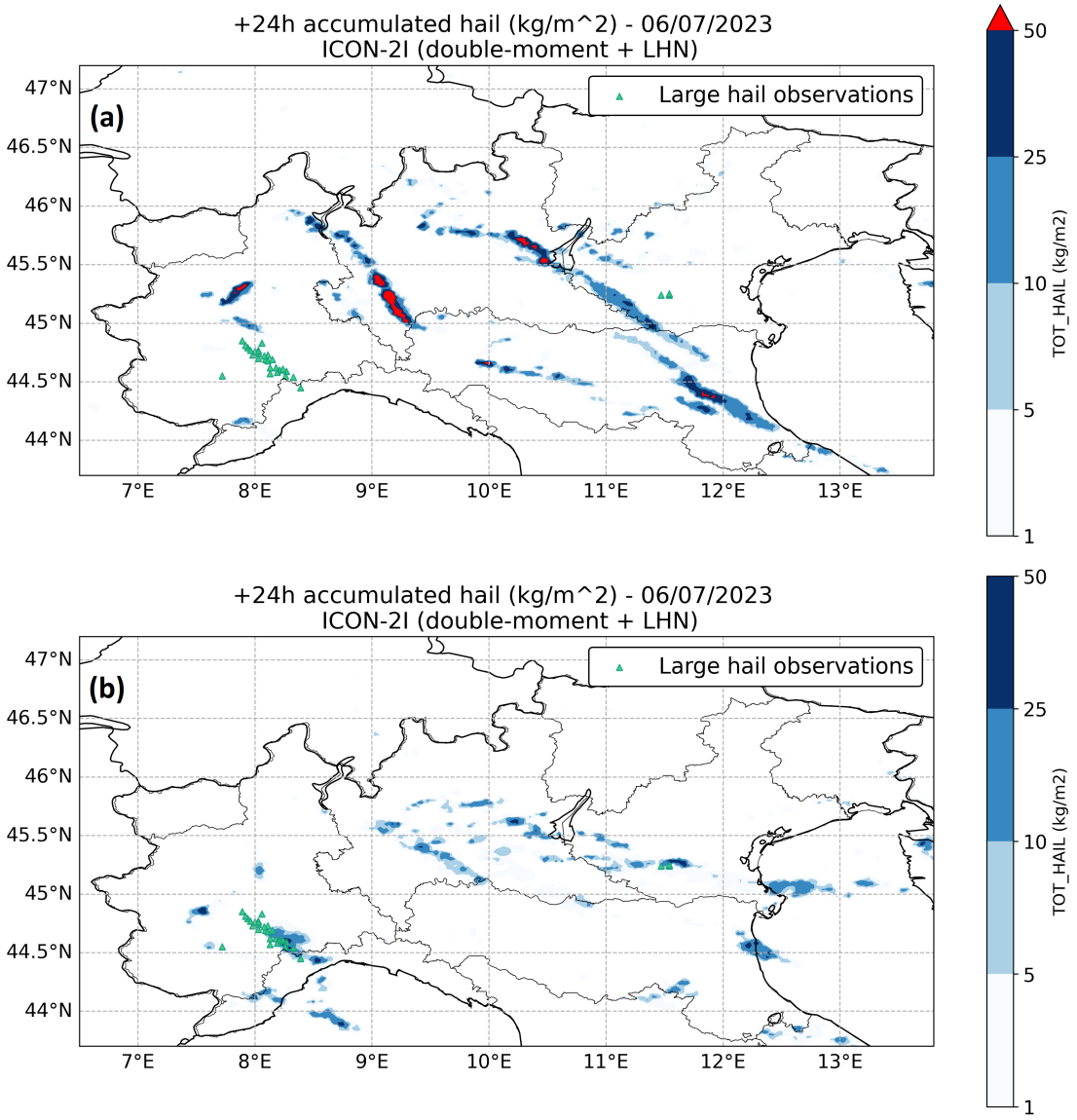

Figure 3.6: Hail accumulations (kg/m^2) produced by (a) IC2M and (b) IC2M-LHN schemes (in blu). The green triangles are addedd in post processing and represent location where large hail was reported that day, based on the European Severe Storm Laboratory (ESSL) database https://eswd.eu/cgi-bin/eswd.cgi

of severe thunderstorms that produced peaks of 100 mm in the IC2M precipitation field. Notably, while this simulation fails to produce the supercell that hit the Piedmont region and, therefore, its associated hail

amounts, it does capture significant hail accumulation from an evening thunderstorm simulated between the provinces of Torino and Asti. In contrast, IC2M-LHN generated moderate hail accumulations of less than $50\,\mathrm{kg\,m^{-2}}$. Although it successfully captures hail occurrences across most affected areas, including Piedmont, it generates a false alarm due to the hail forecast over the province of Milan where only heavy rain and strong wind gusts were actually reported. A detailed analysis of the hail pattern produced by the supercell, as simulated by IC2M-LHN, reveals two discrepancies with the observations. Firstly, the model displaces the primary hail core towards the Ligurian border, to the south of the observed hail core, where the dissipation phase of the cell is observed. Secondly, the simulation shows a delay in hail production compared to the first reports of hail, which occurred as the supercell turned southeastward.

3.1.3 Fraction Skill Score verification

The FSS verification process uses a two-tiered approach to evaluate the accuracy of the model's precipitation forecasts. Initially, a 2D Fuzzy verification is performed by directly comparing the model's 3-hourly precipitation fields with observations. To account for potential temporal displacements of the model's precipitation structures, the analysis is then expanded into a 3D Fuzzy verification, which incorporates the preceding and subsequent 3-hourly simulated fields. Simulations without LHN incorporation are evaluated over the entire Italian domain to assess baseline performance. In contrast, LHN runs focus specifically on Northern Italy, where convective activity was prevalent. This regional focus enables a targeted examination of the model's predictive skill and the efficacy of LHN in convective scenarios. The x-axis shows the thresholds of

three-hourly accumulated precipitation, with the maximum representative of a convective rainfall event, such as that which occurred during the event under study (up to 40 mm/3h). The y-axis, instead, denotes the spatial scale at which verification occurs, ranging from the model's nominal horizontal resolution (2.2 km) up to 143 km. Each point on the plot corresponds to an FSS value (ranging from 0 to 1) for a given combination of precipitation threshold and spatial scale. To assess statistical significance, FSS values exceeding the expected value of a random forecast (i.e., a no-skill reference) are highlighted in bold. This emphasizes that the model's performance at these specific threshold-scale combinations is meaningful and not due to chance. The most demanding verification conditions arise from combining high precipitation thresholds with small spatial scales, as thise requires the model to capture both the intensity and location of precipitation precisely. Conversely, as we move diagonally from the bottom right (high thresholds and small scales) towards the top left (low thresholds and large scales), the model's ability to capture broader precipitation patterns more reliably is expected to improve, resulting in better predictive skill.

2D Fuzzy

Figs. 3.7a, 3.7b, 3.7c, and 3.7d show the 2D Fuzzy plots for the four simulations being investigated. Introducing LHN significantly enhances the model's predictive skill. While the non-assimilated runs only exhibit their first useful spatial scale at 143 km, the assimilated runs prove skillful predictions even at the model's nominal resolution of 2.2 km for low to medium precipitation thresholds ($\leq 5mm/3h$).

Accurately simulating convective events remains a particular challenge

for the model, primarily due to the inherent difficulty of triggering convection at small scales without data assimilation. A minor difference emerges between IC1M and IC2M with regard to the maximum precipitation threshold at which a useful scale is achieved. This threshold is found to be 0.5 mm/3h for the single-moment scheme and at 1.2 mm/3h for the double-moment scheme. However, this marginal improvement does not substantially alter the overall assessment of poor model performances. For higher accumulated precipitation thresholds (e.g., 40 mm/3h), the non-assimilated runs fail to produce useful skill scale. In contrast, the LHN runs show significant improvement: IC1M-LHN successfully captures intense rainfall events, those with a 40 mm/3h threshold, within a spatial range of 6.6 km from the observed locations, for instance. IC2M-LHN, instead, doesn't produce any useful scale at this threshold. When the threshold is lowered to 20 mm/3h, the first useful spatial scale for IC2M-LHN is encountered at 37.4 km. These good results further demostrate the temporal accuracy of the LHN when applied to the single-moment scheme.

3D Fuzzy

The effect of increasing the temporal integration window differs significantly between simulations with and without assimilation. For runs without assimilation, this extended timeframe is particularly beneficial at low precipitation thresholds. The useful scale for IC1M increases substantially, decreasing from 143 km to 37.4 km at the 0.5 mm/3h threshold. Meanwhile, IC2M shows a similar improvement at the 0.2 mm/3h precipitation threshold. These results suggest that, despite exhibiting errors in the timing of convective initiation, the model maintains reasonable skill

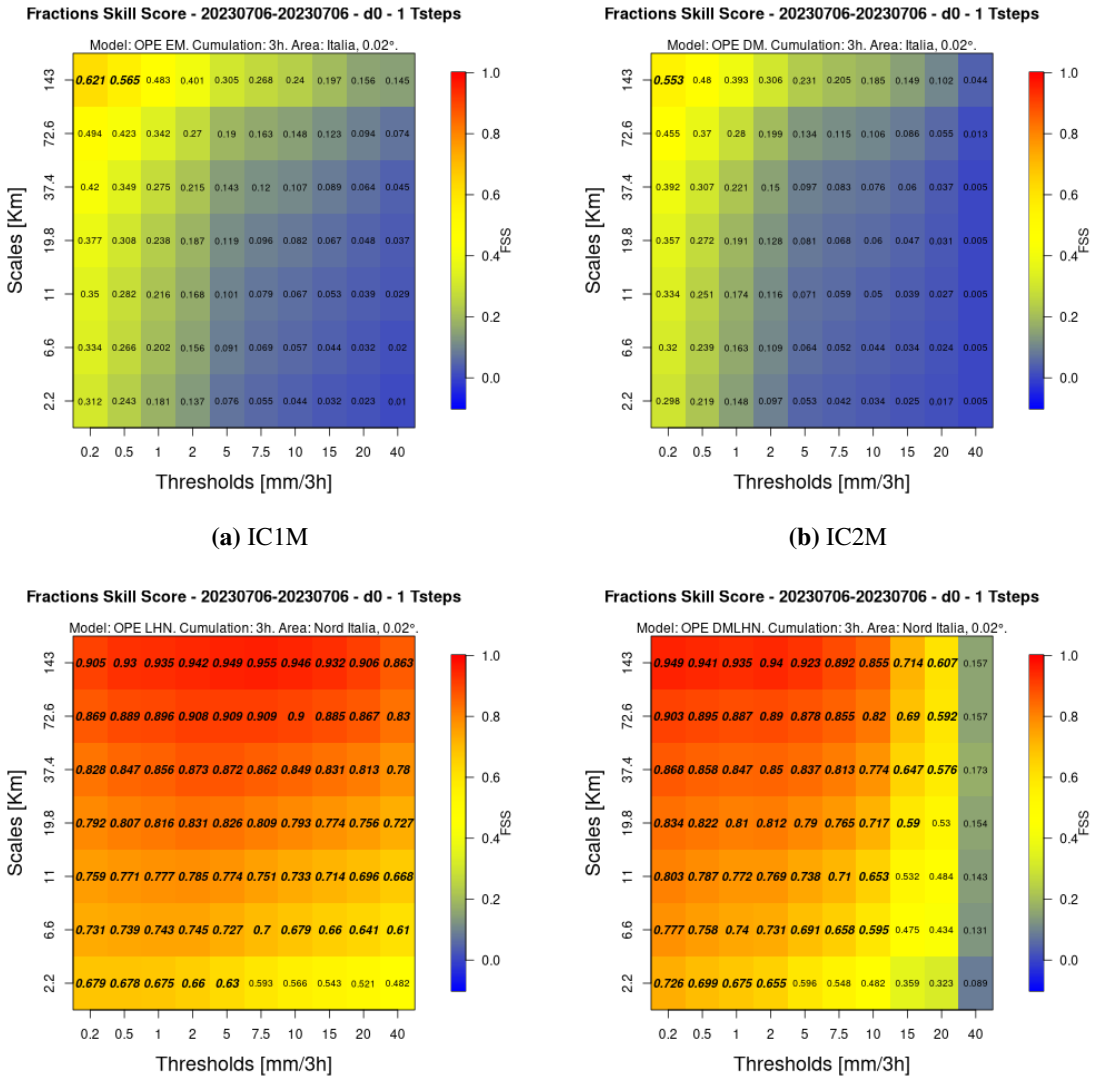

(a) IC1M

(b) IC2M

(c) IC1M-LHN

(d) IC2M-LHN

Figure 3.7: FSS scores for (a) IC1M, (b) IC2M, (c) IC1M-LHN and (d) IC2M-LHN simulations, time-step 1 hour, over the northern Italian territory.

in representing the thermodynamic environment conducive to light-to-moderate precipitation events. In contrast, LHN runs exhibit a twofold behaviour in FSS scores at high thresholds when longer averaging periods are used. For the single-moment scheme, the LHN technique appears to provide excellent temporal and spatial localization of extreme precipitation events. Consequently, expanding the analysis window introduces noise by potentially combining precipitation patterns that occurred before or after the actual event. This effect is clearly demonstrated by the increase of the useful scale at the highest threshold (40 mm/3h) from 6.6 km to 11 km when transitioning from 2D to 3D Fuzzy. In contrast, the FSS values of the double-moment scheme for the 3D Fuzzy are characterized by a slight improvement, particularly at the 20 mm/3h threshold, where the useful scale decreases from 37.4 km to 19.8 km. A substantial improvement is also evident in the useful precipitation threshold at the model resolving scale of 2.2 km, which increases from 2 mm/3h to 7.5 mm/3h.

3.1.4 Reflectivity fields

The evolution of thunderstorms was also examined by analysing radar reflectivity fields. To get data without ground clutter contamination, only data from a height of two kilometres above the surface were considered. The relatively flat topography of the Po Valley facilitates direct comparison between the terrain-following levels of the model and radar-derived constant altitude planes. All analyses are therefore performed using the 37th level of the model, which corresponds to a mean height of 2 km above ground, as well as corresponding observations from 2km CAPPI. As stated previously, simulated reflectivities are calculated runtime starting from the ICON prognostic variables using the EMVORADO operator.

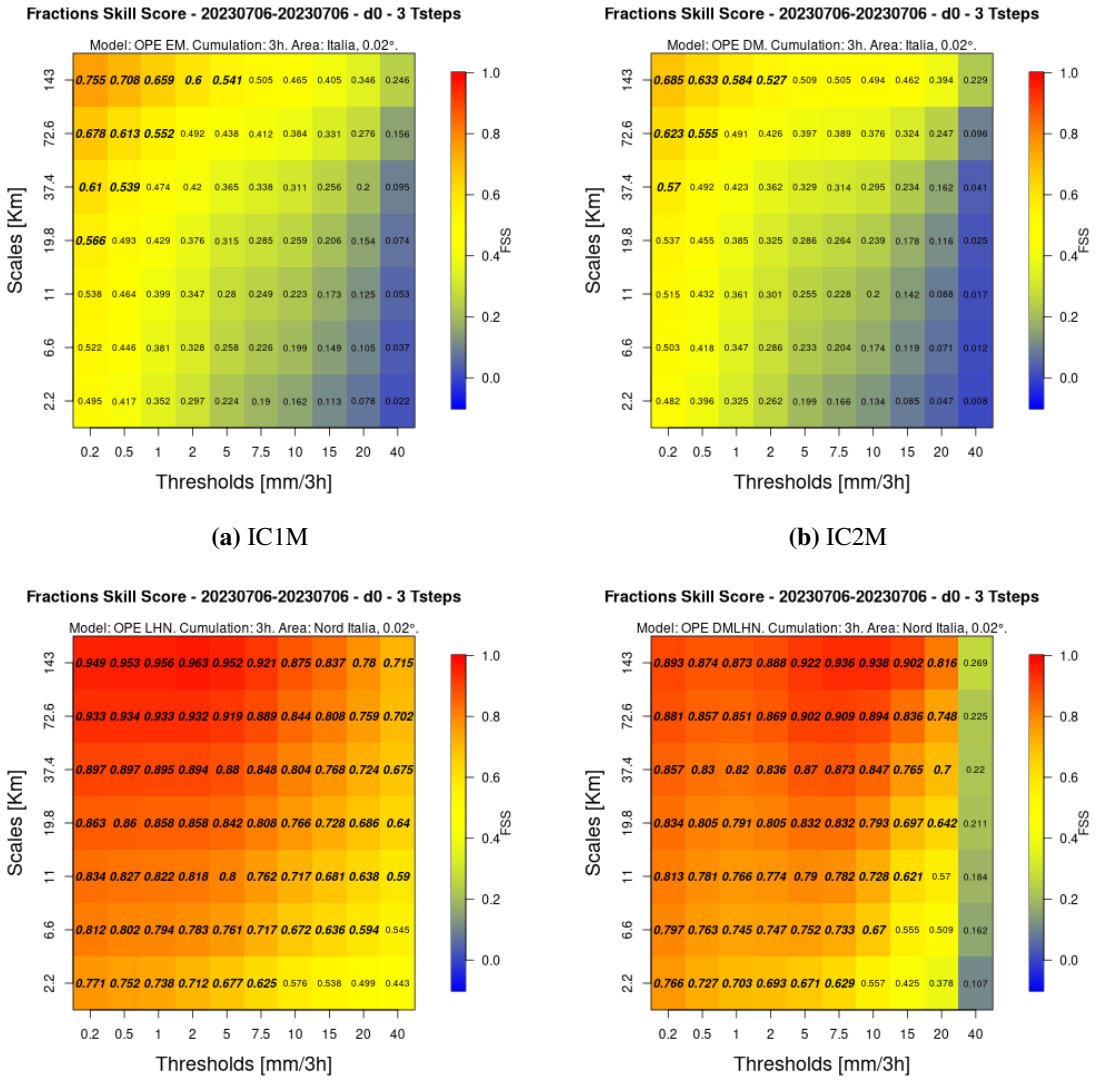

(a) IC1M

(b) IC2M

(c) IC1M-LHN

(d) IC2M-LHN

Figure 3.8: FSS scores for (a) IC1M, (b) IC2M, (c) IC1M-LHN and (d) IC2M-LHN simulations, time-step 1 hour, over the northern Italian territory.

The reflectivity maps at 0810 UTC in Fig. 3.9 reveal distinct convective patterns in simulations with and without LHN. While IC1M-LHN and IC2M-LHN simulations show widespread convective activity across Lombardy and Veneto, this feature is mostly absent in both IC1M and IC2M simulations. Observations depict a multicellular system developing to the east of Lake Como in the early morning. New cells form and propagate eastwards with the mean wind flow. One of these cells manifest right-moving supercell characteristics by 0810 UTC before dissipating south of Lake Garda around 1200 UTC. The IC1M and IC2M simulations successfully reproduce the convection initiation of this cell at similar times and locations. However, the simulated cell diverges from the observation in its subsequent evolution, persisting until 2000 UTC while tracking an east-southeastward trajectory rather than dissipating earlier.

Fig. 3.10 shows the reflectivity patterns over northern Italy at 0850 UTC, revealing significant differences in storm development. While the IC1M and IC2M simulations both forecast cell splitting for the convective system that originated to the east of Lake Como at 0810 UTC, the observations demonstrate that the cell had already reached maturity by this time, as evidenced by the presence of high reflectivity regions, and was propagating southward.

The reflectivity fields observed at 1250 UTC in Fig. 3.11 show the dissipation of the original convective system over Lombardy and Emilia-Romagna, as well as the formation of new convective cells in four distinct regions. These new cells developed along the southern shores of Lake Como, across the plains of the Vercelli province in Piedmont, near the border between the Côte d'Azur and Liguria, and over the Langhe territory - the latter of which represents the supercell under investigation. While

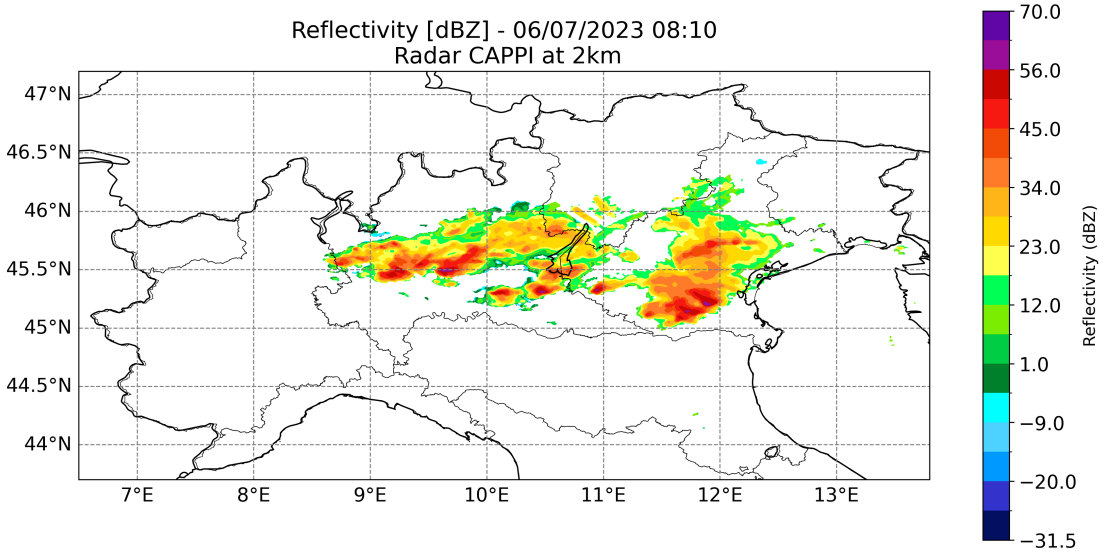

(a) Observations

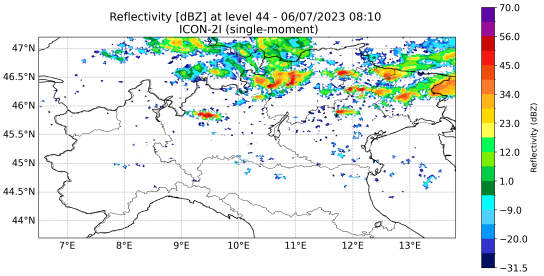

(b) IC1M

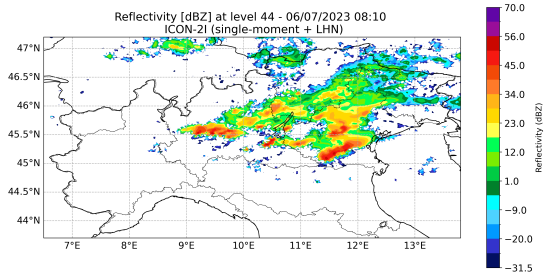

(c) IC1M-LHN

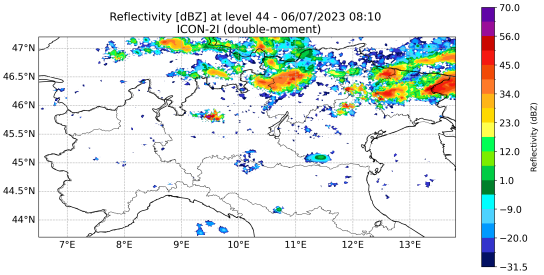

(d) IC2M

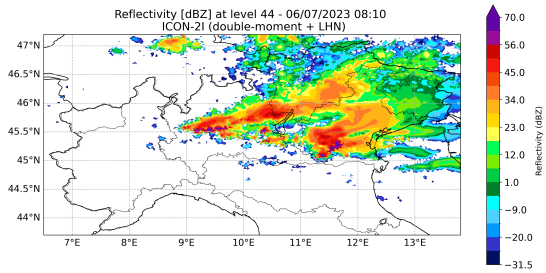

(e) IC2M-LHN

Figure 3.9: Reflectivity fields over Northern Italy produced at 0810 UTC. Observations are retrieved from the Italian Civil Protection Department (DPC) radar composite whereas simulated reflectivity values are produced with EMVORADO

the simulations without assimilation (IC1M and IC2M) only captured the convective activity occurring over Lake Como and Liguria, the runs with

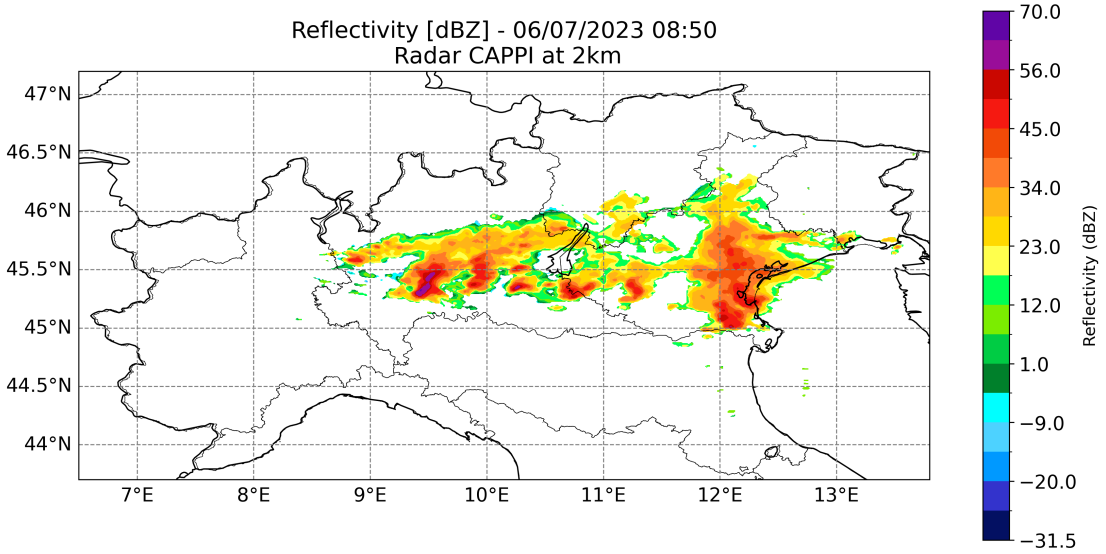

(a) Observations

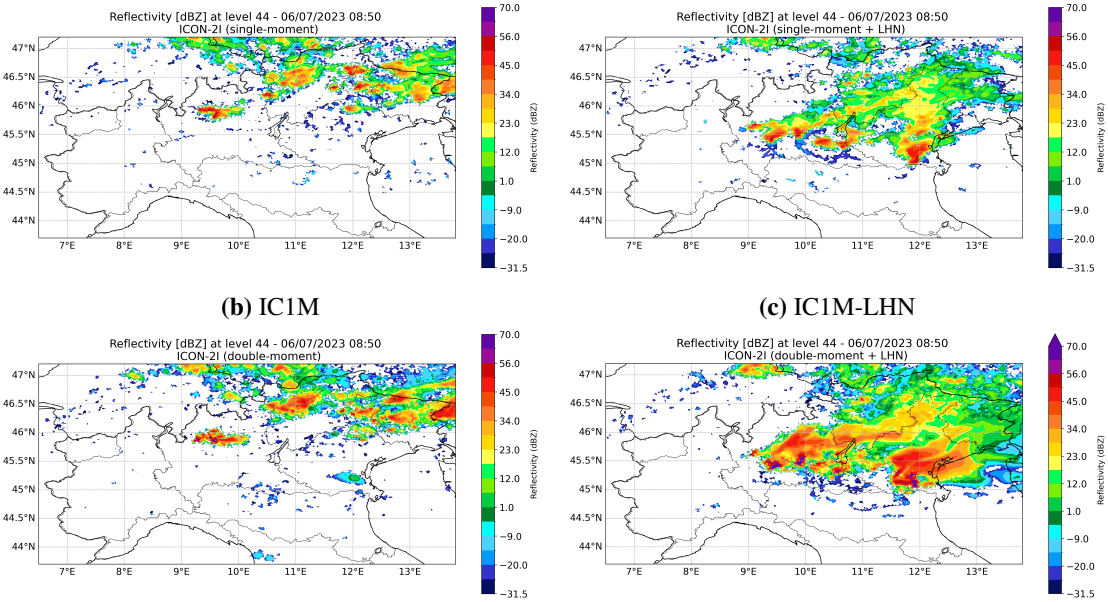

(b) IC1M

(c) IC1M-LHN

(d) IC2M

(e) IC2M-LHN

Figure 3.10: Reflectivity fields over Northern Italy at 0850 UTC. Observations are retrieved from the DPC radar composite (panel a). Simulated reflectivities from the four runs (panel b-d)

LHN assimilation (IC1M-LHN and IC2M-LHN) successfully reproduced the full range of observed convective cells.

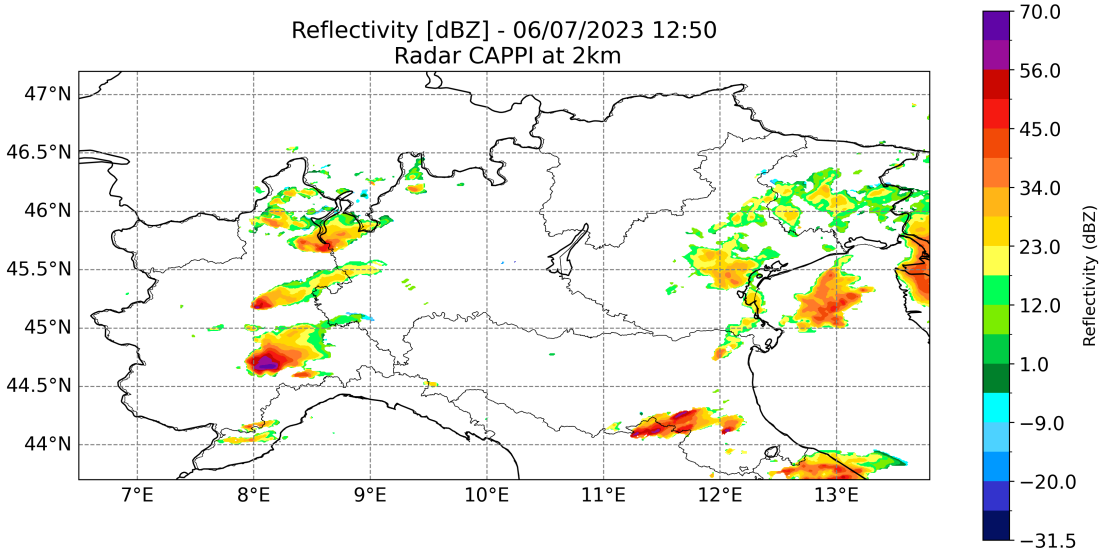

(a) Observations

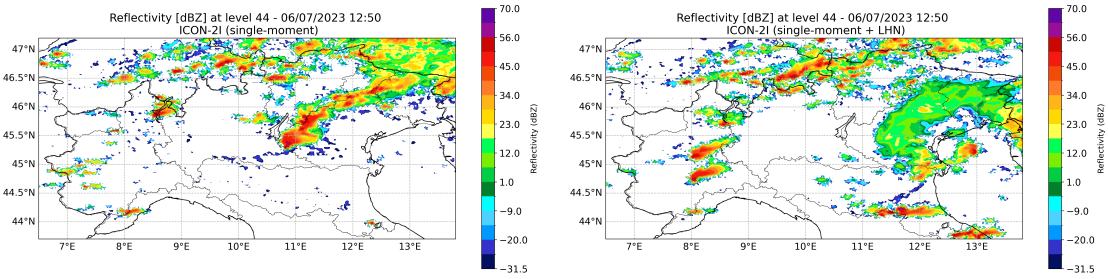

(b) IC1M

(c) IC1M-LHN

(d) IC2M

(e) IC2M-LHN

Figure 3.11: Reflectivity fields over Northern Italy at 1250 UTC. Observations are retrieved from the DPC radar composite (panel a). Simulated reflectivities from the four runs (panel b-d)

At 1330 UTC, the Monte Settepani weather radar observed the supercell at its maximum intensity phase, presenting a broad high-reflectivity region

(marked in purple) and a detached reflectivity tongue advecting precipitation northeastwardly toward Lombardy region. The IC2M-LHN simulation accurately reproduces spatially these observed features but overestimates reflectivity values in the trailing precipitation region by approximately 20 dBZ compared to radar measurements. In contrast, IC1M-LHN generates a more compact reflectivity structure with values gradually diminishing as they radiate outwards from the primary downdraft region. The simulation lacks the distinct precipitation tongue evident in both the observations and the double-moment simulation. The overestimation of reflectivity in the IC2M-LHN run persists throughout the precipitation field, whereas the IC1M-LHN maintains systematically lower values that align more closely with observed intensities, which fail to capture the full spatial extent of the precipitation distribution.

By 1500 UTC, the IC2M-LHN simulation shows the trailing precipitation region moving unrealistically in the streamwise direction (Fig. 3.13), whereas IC1M-LHN simulation better resolves the fine-scale features of the supercell's dissipative phase as it moves over the Ligurian Sea. During this period, the simulations without LHN develop a new convective cell to the west of Lake Como, indicative of the pronounced atmospheric instability present in that region, as evidenced by the high CAPE values. Subsequent analysis (Figs. 3.14 and 3.15) reveals that this cell evolves into a right-moving supercell, which ultimately contributes to the precipitation band discussed in the previous section.

The reflectivity patterns produced by the two microphysics schemes differ significantly, highlighting their respective strengths and limitations. While IC2M-LHN better captures the spatial extent and location of high-reflectivity cores of thunderstorms, particularly evident at 1300 UTC

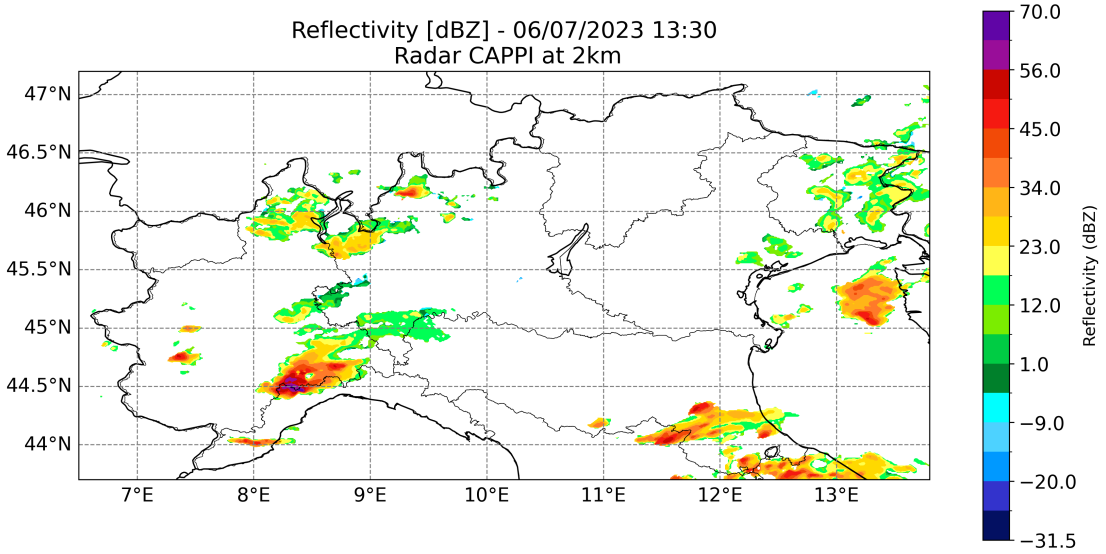

(a) Observations

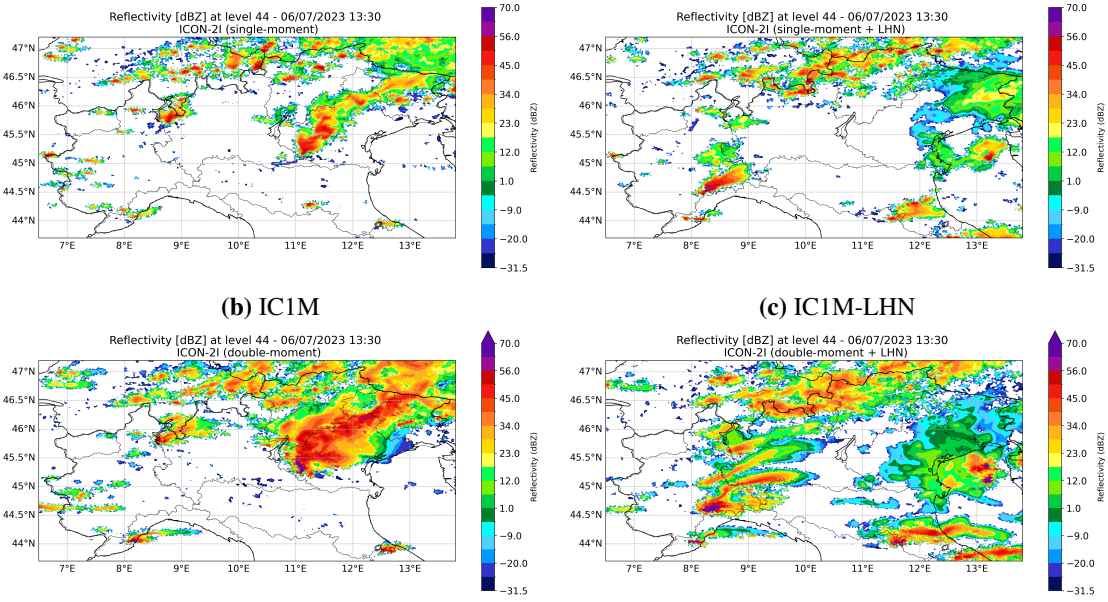

(b) IC1M

(c) IC1M-LHN

(d) IC2M

(e) IC2M-LHN

Figure 3.12: Reflectivity fields over Northern Italy at 1330 UTC. Observations are retrieved from the DPC radar composite (panel a). Simulated reflectivities from the four runs (panel b-d)

in Fig. 3.12, it struggles to reproduce the characteristic morphological features observed in the horizontal cross-sections of the reflectivity maps

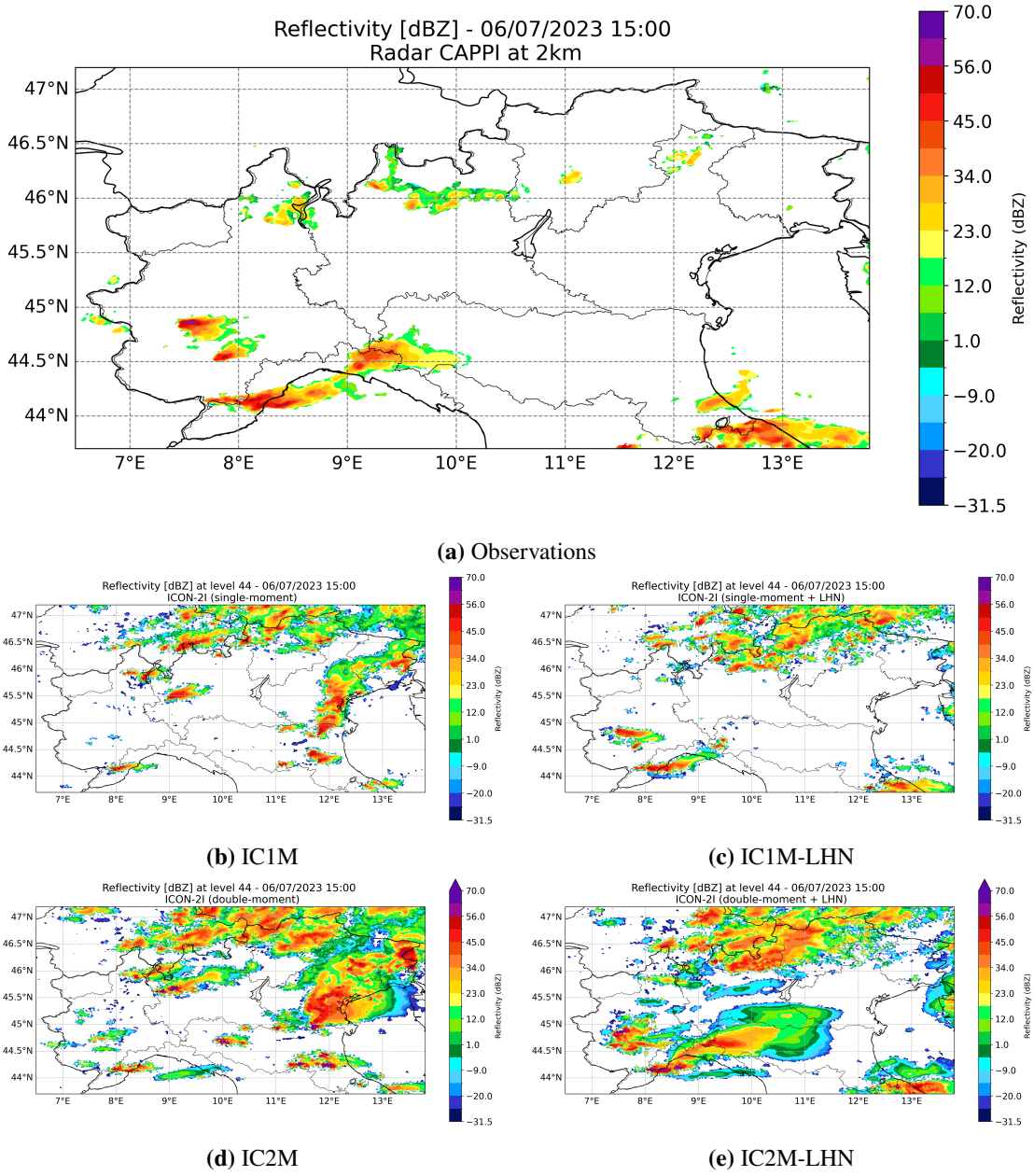

(a) Observations

(b) IC1M

(c) IC1M-LHN

(d) IC2M

(e) IC2M-LHN

Figure 3.13: Reflectivity fields over Northern Italy at 1500 UTC. Observations are retrieved from the DPC radar composite (panel a). Simulated reflectivities from the four runs (panel b-d)

of supercells, such as the hook echo. Overall, IC1M-LHN produces more realistic precipitation distributions and reflectivity patterns. However, its

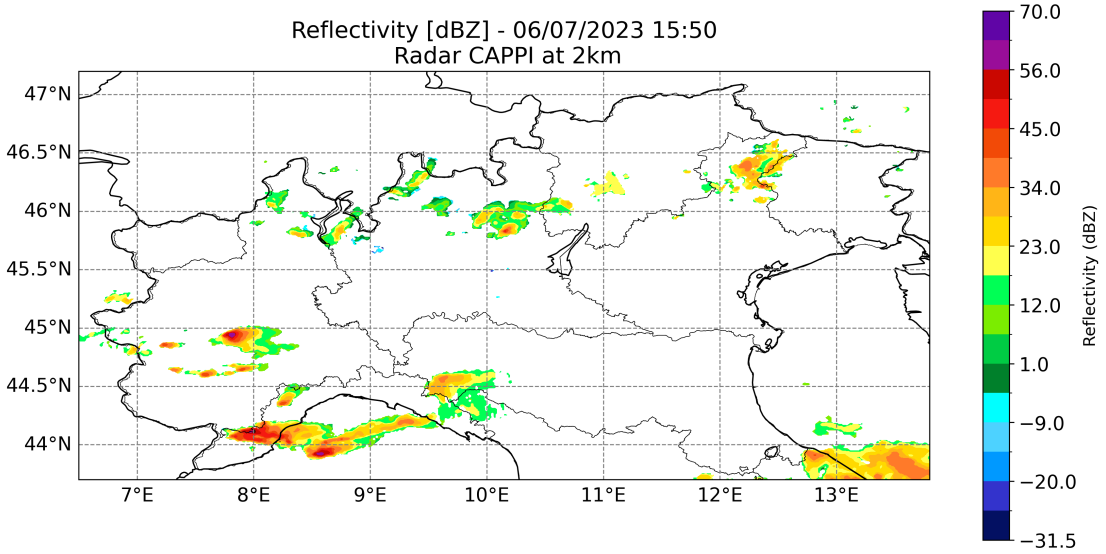

(a) Observations

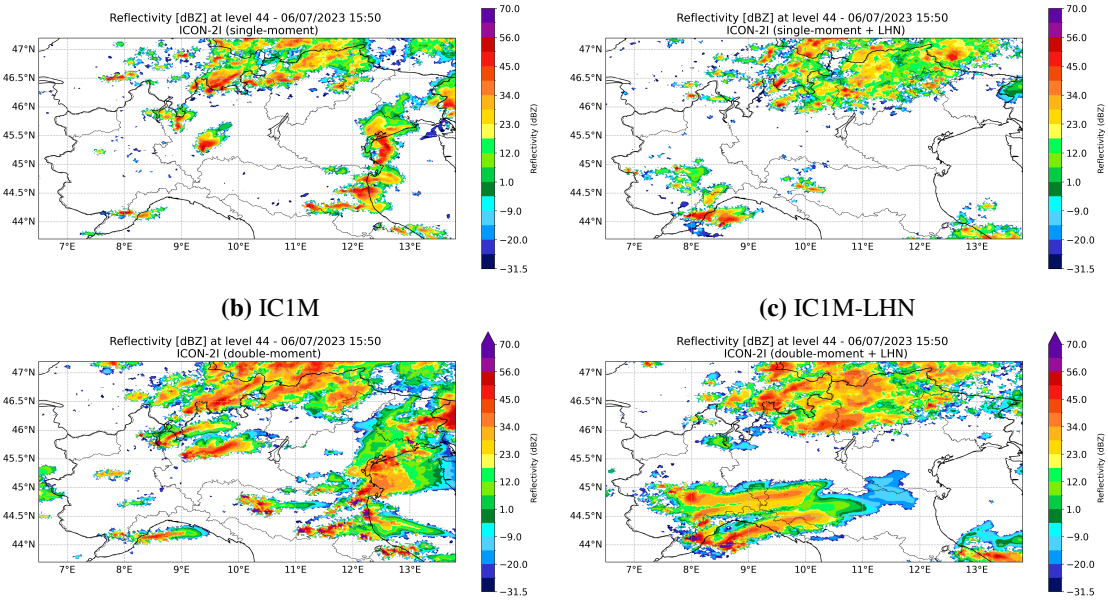

(b) IC1M

(c) IC1M-LHN

(d) IC2M

(e) IC2M-LHN

Figure 3.14: Reflectivity fields over Northern Italy at 1550 UTC. Observations are retrieved from the DPC radar composite (panel a). Simulated reflectivities from the four runs (panel b-d)

inability to simulate hail, a key category of hydrometeor in the simulation of convective thunderstorms, represents a fundamental limitation. Since

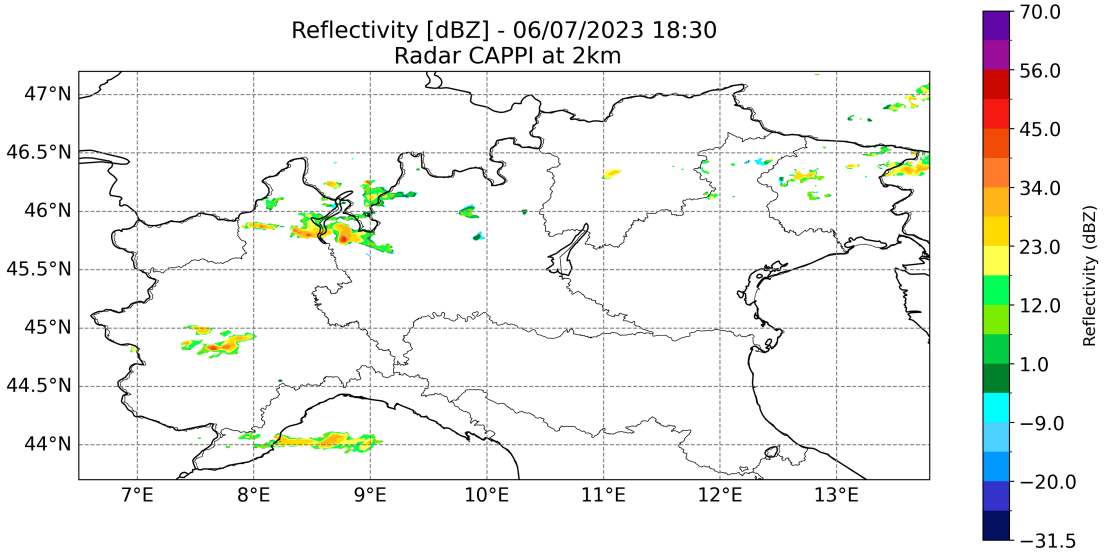

(a) Observations

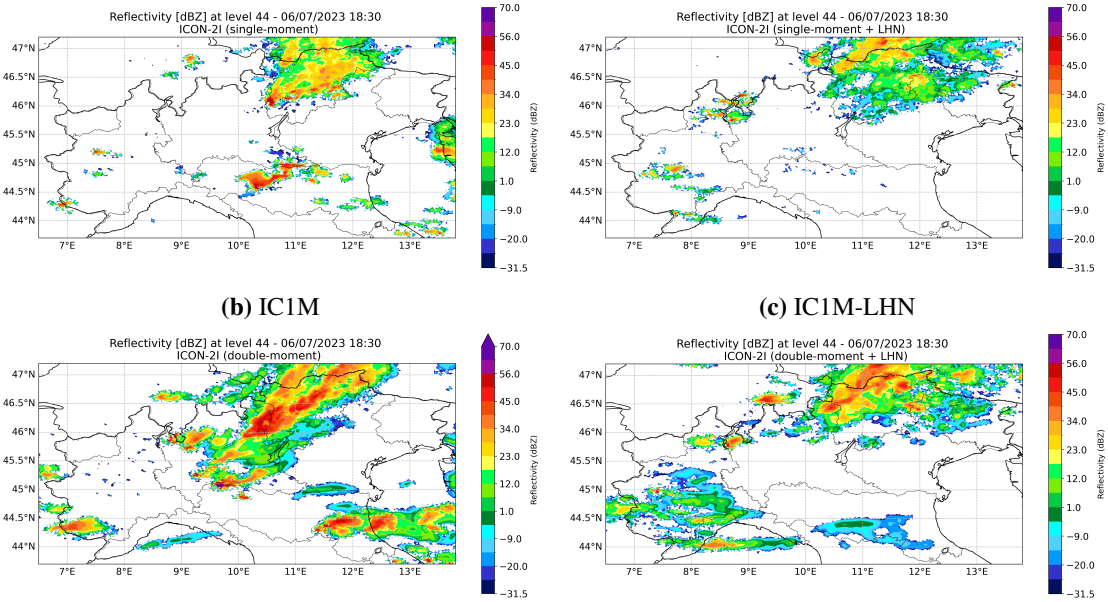

(b) IC1M **(c)** IC1M-LHN

(d) IC2M **(e)** IC2M-LHN

Figure 3.15: Reflectivity fields over Northern Italy at 1830 UTC. Observations are retrieved from the DPC radar composite (panel a). Simulated reflectivities from the four runs (panel b-d)

radar reflectivity depends on the sixth power of the diameter of the particles sample within the radar resolution volume, the absence of large hailstones

results in the highest values of reflectivity being underestimated.

3.1.5 Skew-T Log-p diagrams

IC1M & IC2M The 1200 UTC simulated radiosoundings from IC1M and IC2M at SLE, LIMN, and SPC stations collectively depict a thermodynamically unstable environment across northern Italy, characterized by substantial CAPE[1] values above 2000 J kg^{-1}, coupled with strong low-level wind shear and elevated SRH, all indicative of conditions favorable for severe convection. The simulated dew point temperature profiles exhibit good overall correlation with observations but they tend to smooth pronounced vertical gradients and underrepresent small-scale water vapor fluctuations. In contrast, air temperature profiles show excellent agreement, particularly at the SLE station (Figs. 3.16 and 3.17). Despite this thermodynamic consistency, systematic CAPE underestimation at SLE station persists in both configurations, with a deficit of 32 % for IC1M and 29 % for IC2M, attributable to persistent cold biases in both surface air and dew point temperatures resulting from unassimilated PBL thermodynamic data. Notably, the MLCAPE substantially reduces these biases and provides more reliable estimates of thunderstorm strength, demonstrating the similarity between observed and simulated thermodynamic profiles. Indeed, the error in the single-moment scheme decreases to a modest 4 % overestimation, while the double-moment scheme achieves remarkable accuracy, deviating by just +0.46 % from observations. A significant model-observation discrepancy emerges at the SPC station (Figs. 3.18 and 3.19). While the observed

[1] In this scenario, SBCAPE and MUCAPE coincide due to the absence of a strong capping inversion layer. Therefore, CAPE terminology includes both.

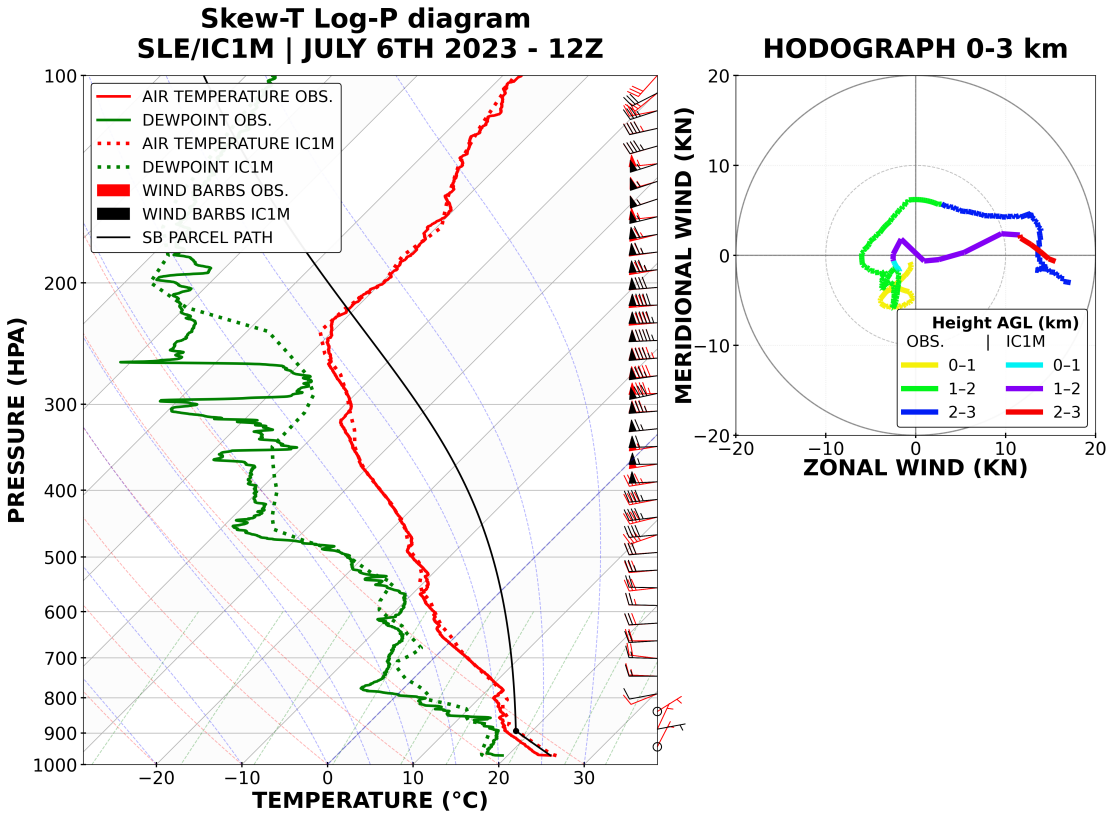

Figure 3.16: Comparison between observed (solid lines) and IC1M-simulated (dashed lines) radiosonde profiles (left panel) and corresponding 0-3 km hodographs (right panel) at SLE station. Temperature profiles show observed air temperature (red), dew point temperature (green), and theoretical surface-lifted parcel temperature (black). Hodograph colors denote different atmospheric layers. Wind barbs indicate speed and direction at standard pressure levels.

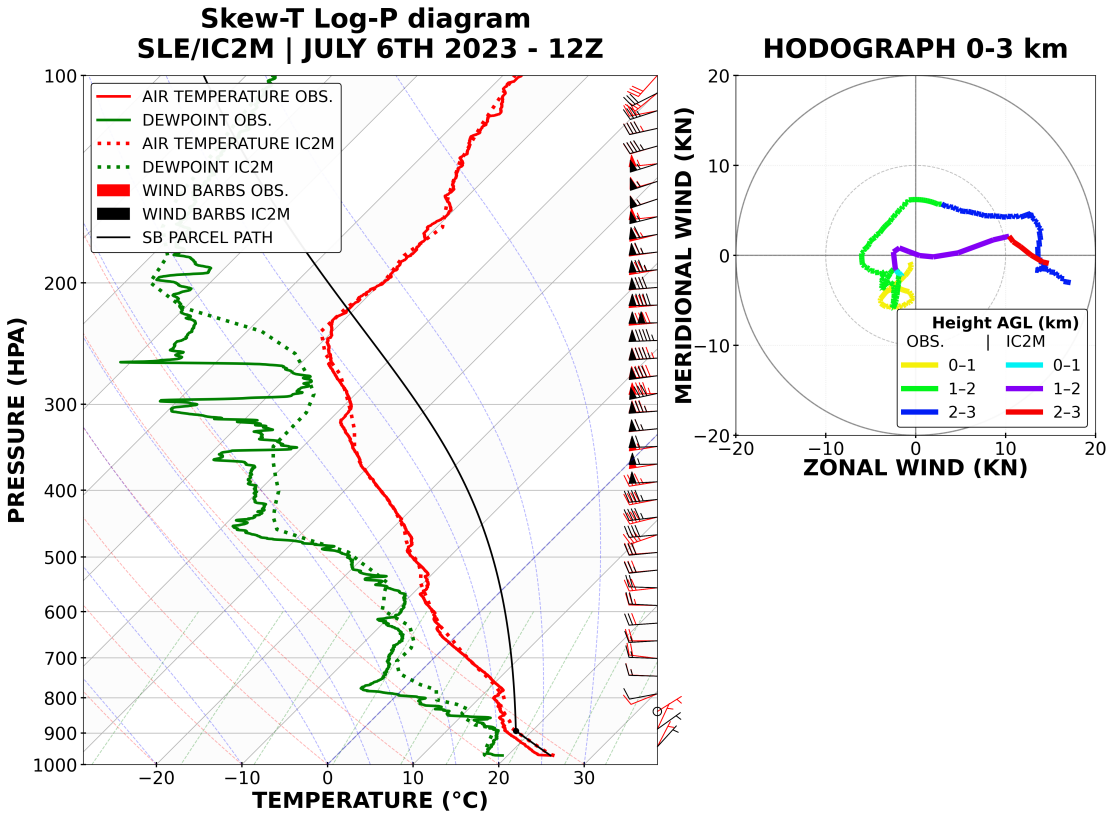

Figure 3.17: Comparison between observed (solid lines) and IC2M-simulated (dashed lines) radiosonde profiles (left panel) and corresponding 0-3 km hodographs (right panel) at SLE. Temperature profiles show observed air temperature (red), dew point temperature (green), and theoretical surface-lifted parcel temperature (black). Hodograph colors denote different atmospheric layers. Wind barbs indicate speed and direction at standard pressure levels.

CAPE values of 683 J kg^{-1} reflect cooling from actual precipitation events in the Bologna province, the simulations maintain unrealistically high values of 2480 J kg^{-1} (IC1M) and 2406 J kg^{-1} (IC2M) due to their failure to predict the actual rainfall events, confirmed by radar analysis. A similar pattern is evident at the LIMN station, where simulated instability is higher than what local observations suggest, indicating that the models may be incorrectly advecting thermodynamic energy eastward. By

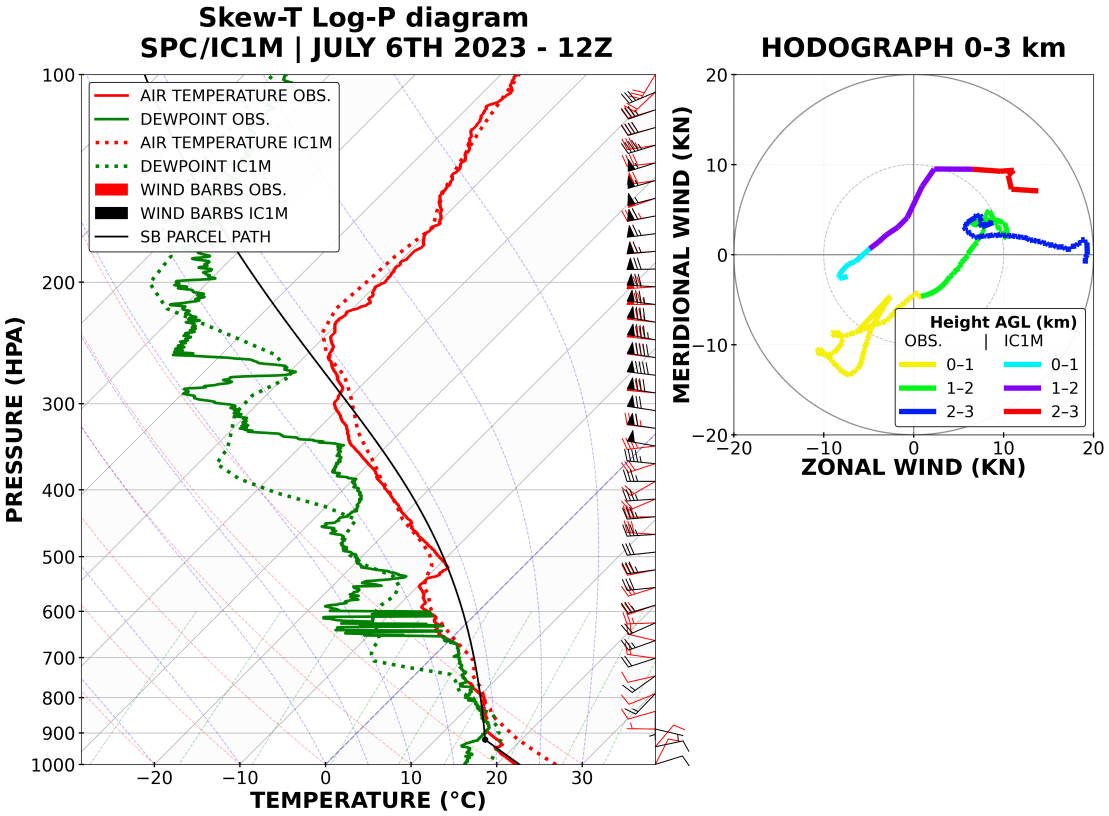

Figure 3.18: Comparison between observed (solid lines) and IC1M-simulated (dashed lines) radiosonde profiles (left panel) and corresponding 0-3 km hodographs (right panel) at SPC. Temperature profiles show observed air temperature (red), dew point temperature (green), and theoretical surface-lifted parcel temperature (black). Hodograph colors denote different atmospheric layers. Wind barbs indicate speed and direction at standard pressure levels.

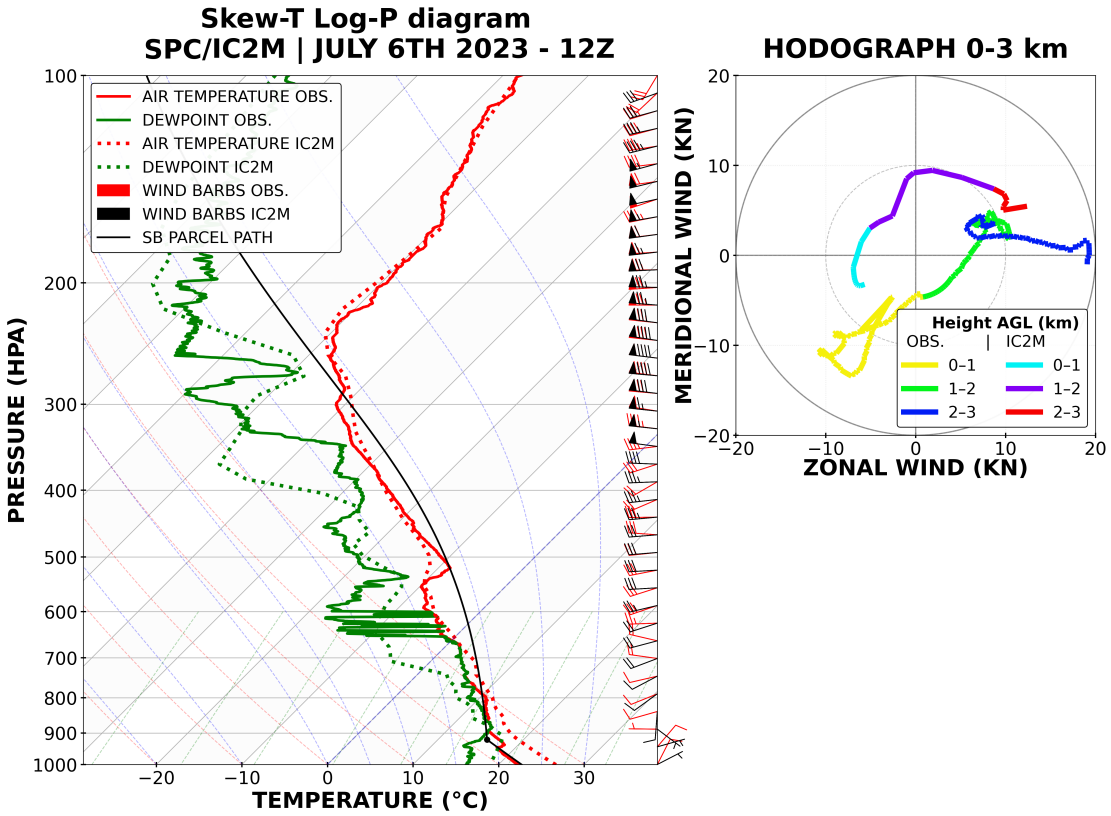

Figure 3.19: Comparison between observed (solid lines) and IC2M-simulated (dashed lines) radiosonde profiles (left panel) and corresponding 0-3 km hodographs (right panel) at SPC. Temperature profiles show observed air temperature (red), dew point temperature (green), and theoretical surface-lifted parcel temperature (black). Hodograph colors denote different atmospheric layers. Wind barbs indicate speed and direction at standard pressure levels.

comparing the simulated and observed wind barbs, plotted on the right vertical axis of the SkewT-LogP diagram before the LHN introduction, we can see that both models struggle to simulate the complex behaviour of wind vectors in the lower boundary layer (0-1 km), which has an impact on the layers just above (1-3 km). Upon entering the free atmosphere, however, the models provide a better prediction of synoptic-scale wind vectors, as evidenced by the near-perfect alignment of the simulated wind barbs with respect to observed ones. The simulated wind profiles in the 0-3 km layer, visualised on the hodograph next to the skew-T log-p diagram, demonstrate varying degrees of supercell-favourable kinematic characteristics across radiosounding stations. At SLE (Figs.3.16 and 3.17), both schemes produce marginal supercell conditions: vertical wind shear reaches $\approx 10\,\mathrm{m\,s^{-1}}$ in the 0-3 km range and $\approx 22\,\mathrm{m\,s^{-1}}$ in the 0-6 km range, while hodographs show subtle clockwise curvature quantified by an SRH in the 0-3 km layer of $86\,\mathrm{m^2\,s^{-2}}$ for IC1M (Fig. 3.16) and of $83\,\mathrm{m^2\,s^{-2}}$ for IC2M (Fig. 3.16), significantly weaker than the observed $113\,\mathrm{m^2\,s^{-2}}$. Though, the reason for a null SCP, despite documented supercell development nearby, is to attribute to the 0-3km bulk wind shear slightly below the 10 m/s threshold recorded by both simulations and observations. In contrast to observations, where SCP = 1, both IC1M and IC2M significantly overestimate supercell potential at SPC, producing SCP values of 5 and 4 respectively. This discrepancy stems from three factors in the simulations: (1) artificially elevated MUCAPE values resulting from unpredicted precipitation events, (2) enhanced SRH values of $154\,\mathrm{m^2\,s^{-2}}$ (IC1M) and of $149\,\mathrm{m^2\,s^{-2}}$ (IC2M) in 0-3 km layer, representing 25 % and 21 % overestimations respectively, further corroborated by the distinctive C-shaped hodograph curvature, characteristic of right-moving supercells,

and (3) 0-3 km wind shear exceeding the $10\,\mathrm{m\,s^{-1}}$ supercell threshold set in the SCP formulation. The combined effect of these parameters creates a favorable environment for sustained, rotating updrafts in the model simulations.

IC1M-LHN & IC2M-LHN The implementation of LHN yields significant improvements in the simulated radiosoundings. Most notably, the 0 km to 3 km hodographs show markedly better agreement with observations, evidenced by a 15 % average reduction in ESRH bias compared to non-assimilated runs. The double-moment scheme at LIMN station in Fig. 3.20 achieves particularly striking accuracy, with errors in 0-3 km SRH of less than 1 %. The thermodynamic profiles of both the SPC and LIMN stations have improved substantially, confirming the effectiveness of LHN in properly assimilating precipitation events into the model framework. LHN's most pronounced impact appears in CAPE adjustments. At the SPC station, IC1M-LHN produces a 65 % CAPE reduction, resulting in a much more realistic 26 % positive bias relative to observations, comparable to the model performance at SLE. However, when LHN is applied to the double-moment scheme, it overcorrects the thermodynamic profile, generating a 44 % CAPE underestimation. This pattern persists at the LIMN station, where LHN demonstrates consistently better performance with the single-moment scheme. Improvements are also observed at Cuneo Levaldigi, where LHN reduces the CAPE bias to 25 % for IC1M-LHN (Fig. 3.21) and 22 % for IC2M-LHN (Fig. 3.22), which further validates LHN's ability to improve thermodynamic representation. According to the null eSCP values, the effective inflow layer cannot sustain an environment conducive to supercell development in any of the four simulations, nor

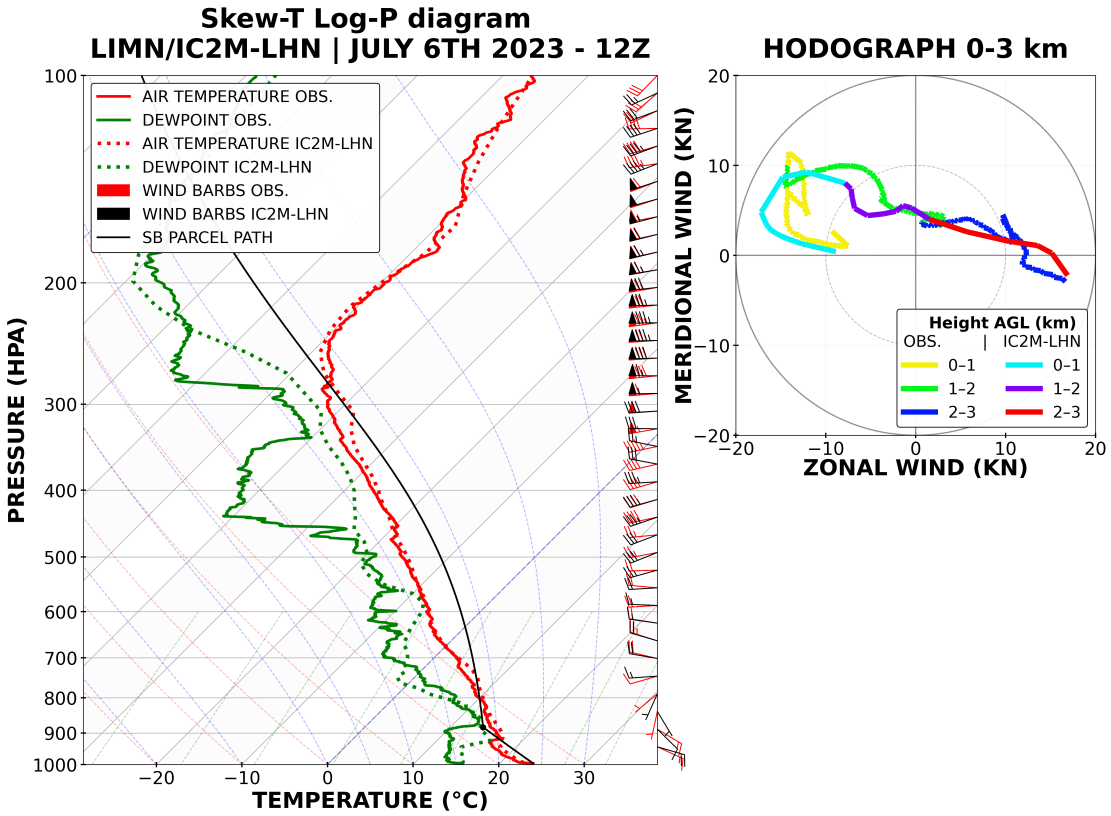

Figure 3.20: Comparison between observed (solid lines) and IC2M-LHN-simulated (dashed lines) radiosonde profiles (left panel) and corresponding 0-3 km hodographs (right panel) at LIMN. Temperature profiles show observed air temperature (red), dew point temperature (green), and theoretical surface-lifted parcel temperature (black). Hodograph colors denote different atmospheric layers. Wind barbs indicate speed and direction at standard pressure levels.

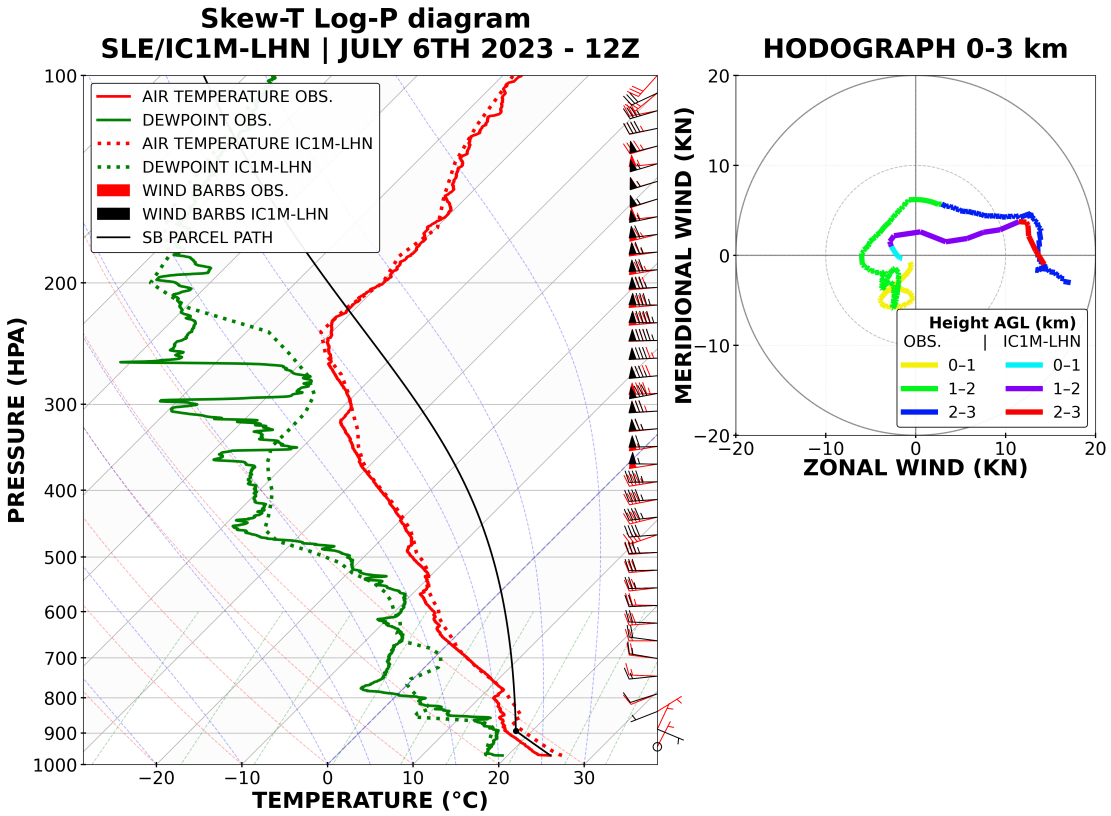

Figure 3.21: Comparison between observed (solid lines) and IC1M-LHN-simulated (dashed lines) radiosonde profiles (left panel) and corresponding 0-3 km hodographs (right panel) at SLE. Temperature profiles show observed air temperature (red), dew point temperature (green), and theoretical surface-lifted parcel temperature (black). Hodograph colors denote different atmospheric layers. Wind barbs indicate speed and direction at standard pressure levels.

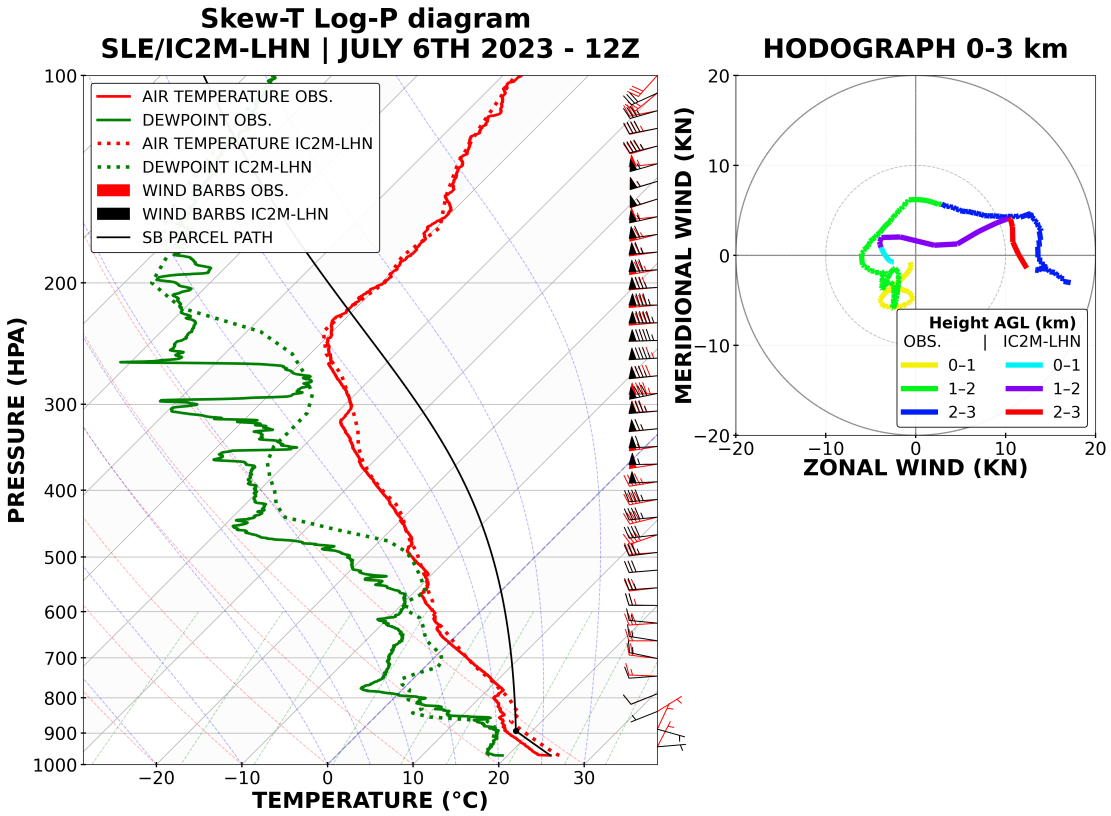

Figure 3.22: Comparison between observed (solid lines) and IC2M-LHN-simulated (dashed lines) radiosonde profiles (left panel) and corresponding 0-3 km hodographs (right panel) at SLE. Temperature profiles show observed air temperature (red), dew point temperature (green), and theoretical surface-lifted parcel temperature (black). Hodograph colors denote different atmospheric layers. Wind barbs indicate speed and direction at standard pressure levels.

in the observations. However, since a supercell was observed near SLE approximately one hour after the radiosounding, it can be concluded that the CAPE and CIN requirements that define the effective inflow layer may be too stringent for the observed phenomenon and a focus on SCP is preferrable. In order to have a clearer overview of the situation, the parameters associated to the radiosoundings across all stations and model configurations are entirely reported in Tab. 3.1, Tab. 3.2 and in Tab. 3.3.

Table 3.1: Comparison between observed (Obs) and simulated sounding parameters for the LIMN station

Parameter	**Unit**	**Obs**	**IC1M**	**IC2M**	**IC1M-LHN**	**IC2M-LHN**
SBCAPE	$J\,kg^{-1}$	987	2389	2497	800	694
SBCIN	$J\,kg^{-1}$	0	0	0	-38	-49
MLCAPE	$J\,kg^{-1}$	132	1942	2039	654	731
MLCIN	$J\,kg^{-1}$	-111	0	0	-41	-31
Inflow Base Height	m	176	186	186	186	186
Inflow Top Height	m	361	2283	2132	1845	2132
ESRH	$m^2\,s^{-2}$	21	45	41	94	134
EBWD	kt	6	10	9	12	11
0-1 km SRH	$m^2\,s^{-2}$	20	15	16	34	70
0-3 km SRH	$m^2\,s^{-2}$	156	77	76	112	158
0-6 km SRH	$m^2\,s^{-2}$	160	108	111	142	172
0-1 km Shear	kt	7	3	3	3	6
0-3 km Shear	kt	28	19	19	24	27
0-6 km Shear	kt	37	29	29	36	39
SCP	–	2	0	0	1	1
eSCP	–	0	0	0	0	0

Table 3.2: Comparison between observed (Obs) and simulated sounding parameters for the SLE station

Parameter	Unit	Obs	IC1M	IC2M	IC1M-LHN	IC2M-LHN
SBCAPE	$J\,kg^{-1}$	2994	2030	2128	2245	2335
SBCIN	$J\,kg^{-1}$	0	0	0	0	0
MLCAPE	$J\,kg^{-1}$	1722	1642	1714	1816	1955
MLCIN	$J\,kg^{-1}$	0	-5	-3	-10	-4
Inflow base	m	385	380	380	380	380
Inflow top	m	403	1983	2260	1490	1490
ESRH	$m^2\,s^{-2}$	1	68	73	52	54
EBWD	kt	1	12	13	4	3
0-1 km SRH	$m^2\,s^{-2}$	-18	16	12	8	8
0-3 km SRH	$m^2\,s^{-2}$	113	86	83	88	81
0-6 km SRH	$m^2\,s^{-2}$	158	173	179	162	162
0-1km Shear	kt	3	3	3	3	3
0-3km Shear	kt	18	19	19	19	18
0-6km Shear	kt	42	43	43	43	42
SCP	–	0	0	0	0	0
eSCP	–	0	0	0	0	0

3.1.6 Comparison with ground stations

This section provides a point-by-point verification analysis, comparing the surface variables simulated at the lowest model level (65) with ground station observations along the supercell's trajectory. Both statistical and graphical assessment methods are used to assess model performance. Statistical verification involves calculating the bias and RMSE, averaged across all stations and time points. Graphical analysis incorporates time-series plots that track the temporal evolution of key variables. Together, these approaches provide a rigorous evaluation of the model's ability to

Table 3.3: Comparison between observed (Obs) and simulated sounding parameters for the SPC station

Parameter	Unità	Obs	IC1M	IC2M	IC1M-LHN	IC2M-LHN
SBCAPE	$J\,kg^{-1}$	683	2480	2406	861	379
SBCIN	$J\,kg^{-1}$	-17	0	0	-35	-97
MLCAPE	$J\,kg^{-1}$	374	2174	2108	402	96
MLCIN	$J\,kg^{-1}$	-43	0	0	-56	-102
Inflow base	m	11	20	20	20	20
Inflow top	m	1149	2511	2511	571	327
ESRH	$m^2\,s^{-2}$	121	130	131	31	1
EBWD	kt	14	21	18	3	10
0-1km SRH	$m^2\,s^{-2}$	40	16	29	103	66
0-3km SRH	$m^2\,s^{-2}$	123	154	149	166	202
0-6km SRH	$m^2\,s^{-2}$	158	224	232	199	225
0-1km Shear	kt	8	3	5	17	9
0-3km Shear	kt	26	26	23	30	35
0-6km Shear	kt	33	38	37	39	48
SCP	–	1	5	4	2	1
eSCP	–	0	4	0	0	0

represent the atmospheric conditions near the surface experienced during the supercell event.

Air temperature

In the hours preceding the supercell development, all model configurations realistically reproduce the temporal evolution of the 2 meter air temperature. Despite this, a consistent cold bias is evident, particularly at the Alba Tanaro (Fig. 3.23) and Borgone stations. This is caused by an underestimation of the initial temperature by around 2 °C. This temperature discrepanciy is

evident even in LHN runs prior to 1200 UTC. However, as the supercell develops and produces intense rainfall, the IC1M-LHN and IC2M-LHN models accurately capture the rapid decrease in the observed temperature profile. This is due to the combined effects of cloud shading and cooling caused by rain evaporation and hail melting. Overall, IC1M is hotter

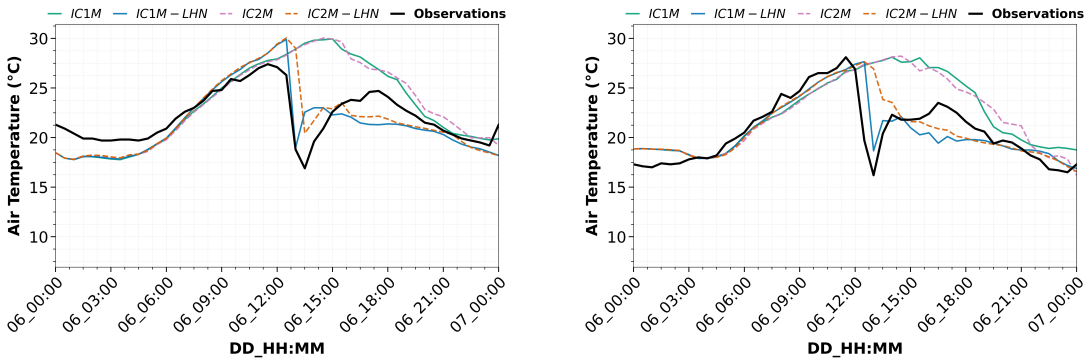

(a) Alba Tanaro **(b)** Baldissero

Figure 3.23: 24-hour temporal evolution of observed (bold line) and simulated (colored lines) air temperature at the surface measured at the (a) Alba Tanaro and (b) Baldissero, Piedmont (Italy) ground weather stations on 6 July, 2023.

by 0.6 °C at the surface, compared to a positive 0.8 °C bias for IC2M. However, the RMSE shows no substantial difference between the two, with values around 2.5 °C falling outside the generally accepted range of 1.5 °C to 2 °C observed when KENDA is operational [41]. This suggests significant discrepancies between the model results and the observations. The introduction of LHN notably impacts on the air temperature bias of the double-moment scheme, shifting it from a positive 0.8 °C to a negative 0.35 °C. The single-moment scheme exhibits a similar, albeit more confined, inversion tendency, with a bias reduction from +0.6 °C to −0.2 °C. Together with a reduced RMSE of 2, the LHN assimilated

simulation is in line with the predictive skills of ICON-2I.

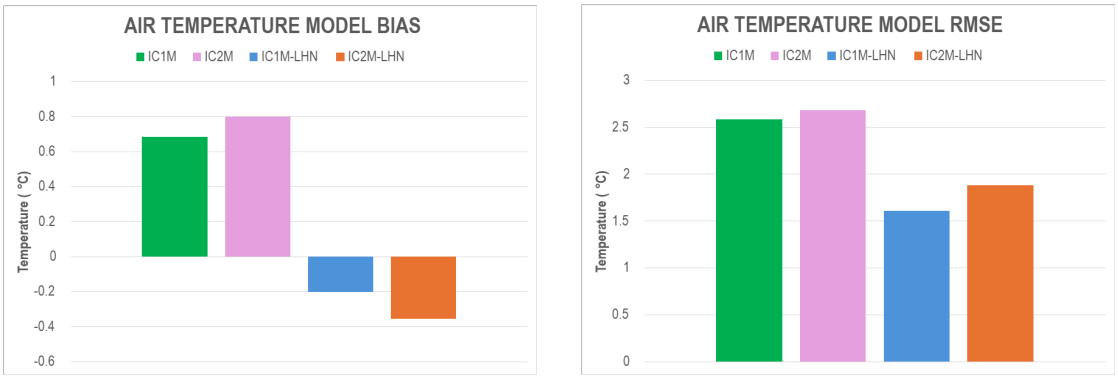

(a) Temperature bias

(b) Temperature RMSE

Figure 3.24: Statistical comparison of simulated and observed air temperature at the surface across all ground stations and hours: (a) systematic bias and (b) root mean square error (RMSE).

Precipitation

Precipitation data was collected from ground-based rain gauges and the model at 10-minutes interval. Temporal plots display the accumulated precipitation, which is computed by summing the incremental precipitation measurements. Due to the high spatial variability of precipitation fields, even minor discrepancies between simulated and observed rainfall patterns could result in false null values at station locations, which would artificially inflate model skill scores if included in the analysis. To avoid this bias, the comparison is restricted to cases where either the model or the observations reported a positive precipitation value. Fig. 3.25 shows that the IC1M-LHN simulation accurately reproduces both the correct accumulated precipitation value of 40 mm and the timing of the supercell's passage over the Alba Tanaro station at 1230 UTC. In contrast, the IC2M-LHN simulation underestimates the accumulated precipitation value by 30 mm

and shows the supercell passing 30 minutes later. Runs withoput LHN assimilation fail to capture any rainfall at all. Similar verification at

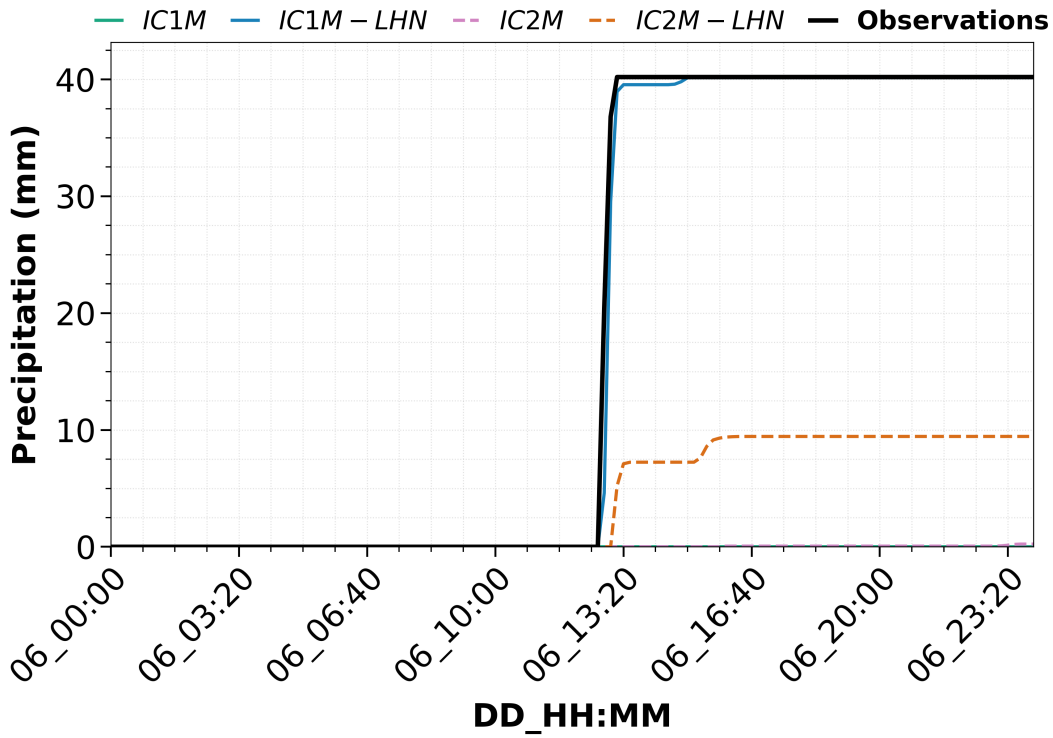

Figure 3.25: 24-hour temporal evolution of observed (bold line) and simulated (colored lines) profiles of accumulated precipitation at the surface measured at the Alba Tanaro, Piedmont (Italy) ground weather station on 6 July, 2023.

other stations (Pino Torinese and Buttigliera d'Asti, Fig. 3.26) confirms the superior performance of the IC1M-LHN run in replicating both precipitation intensity and event timing.

The spatial progression of these results aligns with the supercell's developmental stage. At Pino Torinese, the first station to be impacted, IC2M-LHN produced only light precipitation, as the simulated storm had not yet reached maturity during this early phase. Instead, the bulk of

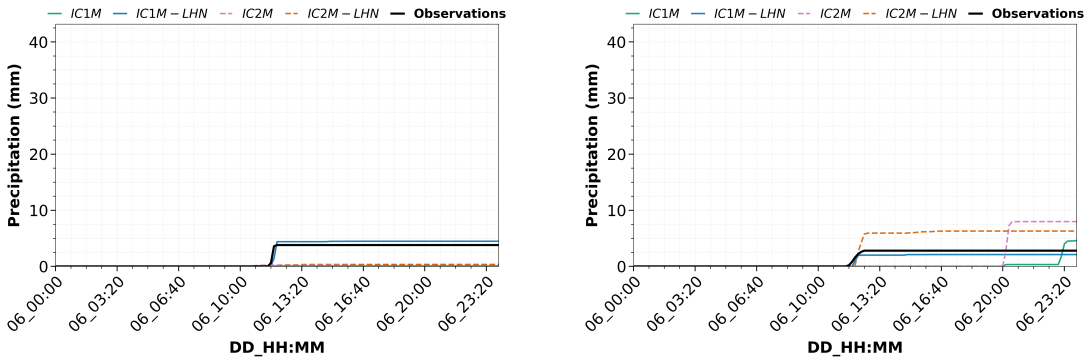

(a) Pino Torinese **(b)** Buttigliera Asti

Figure 3.26: 24-hour temporal evolution of observed (bold line) and simulated (colored lines) profiles of accumulated precipitation at the surface measured at the (a) Pino Torinese and (b) Buttigliera d'Asti, Piedmont (Italy) ground weather stations on 6 July, 2023.

precipitation from IC2M-LHN concentrates downstream at Buttigliera d'Asti, where simulated values exceed observations by 3 mm. After implementing LHN assimilation, we observe a reduction in model bias, with the best scores obtained by the single-moment scheme, while the RMSE remains on pre-assimilated values (Fig. 3.27).

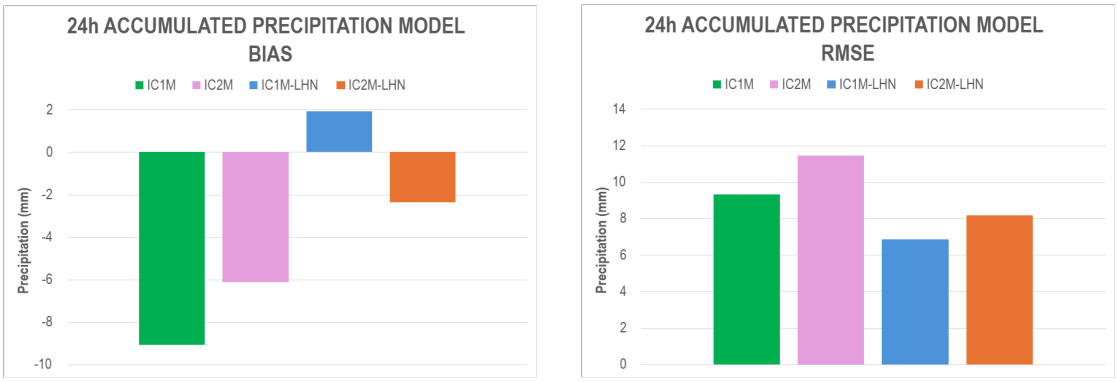

(a) Precipitation bias **(b)** Precipitation RMSE

Figure 3.27: Statistical comparison of simulated and observed accumulated precipitation at the surface across all ground stations and hours: (a) bias and (b) RMSE.

Relative humidity

Ground station observations of 24-hours relative humidity exhibit a characteristic U-shaped diurnal cycle, with morning and evening maxima bracketing an afternoon minimum. This typical pattern is disrupted by the passage of the supercell. Indeed, under high-pressure conditions, relative humidity would continue to decrease through the afternoon due to rising temperatures. However, the supercell downdraft is filled with water vapour saturated air. The resupply of nearby moist air advected by the gust front, which originates when the cold pool spreads out at the ground and the evaporation of precipitation at the surface contribute to produce the observed afternoon increase in relative humidity which is well captured at the Bauducchi, Buttigliera d'Asti, Pino Torinese and Alba Tanaro stations (Fig. 3.28).

Neither IC1M nor IC2M reproduce this reduction feature, both showing the highest bias, accompanied by an equally high RMSE, as seen in Fig. 3.29. LHN reduces the model bias but not the RMSE to the same degree, meaning that noise in the model is still very present. Overall, all simulations exhibit a negative bias, meaning the model is less humid, which could impact the strenght of the convective updraft.

Wind speed

As expecte, analysis of the observed wind speed and direction time series (black line in Fig. 3.30) reveals a marked increase in wind speed and greater angular change of wind direction during the passage of the supercell, as recorded by ground stations. A localized increase in wind speed accompanied by unsteady wind direction indicates the presence of a thunderstorm, particularly when its downdraft reaches the surface and

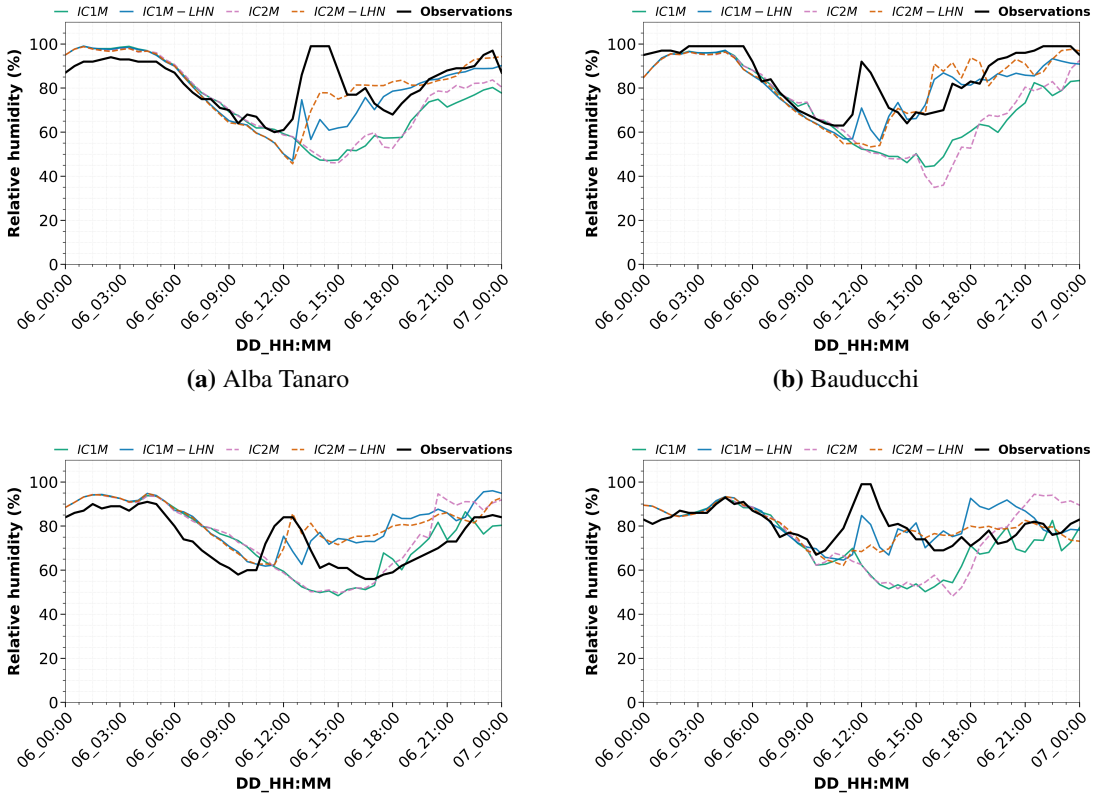

(a) Alba Tanaro **(b)** Bauducchi

(c) Buttigliera d'Asti **(d)** Pino Torinese

Figure 3.28: 24-hour temporal evolution of observed (bold line) and simulated (colored lines) surface relative humidity measured at the (a) Alba Tanro, (b) Bauducchi, (c) Buttigliera Asti and (d) Pino Torinese, Piedmont (Italy) ground weather stations on 6 July, 2023.

spreads radially. This feature is taken as the reference for the comparison with the simulations, which were performed only for the cases where at least one value, either simulated or observed, exceeded the dead-calm threshold. Given the sensitivity of the anemometers, this threshold was set to $1\,\mathrm{m\,s^{-1}}$. When evaluating the simulated wind speed time series against observations, only the IC1M-LHN and IC2M-LHN profiles exhibit a reasonable correlation. In contrast, IC1M and IC2M (runs without assimilation) show no discernible increase in wind speed attributable to

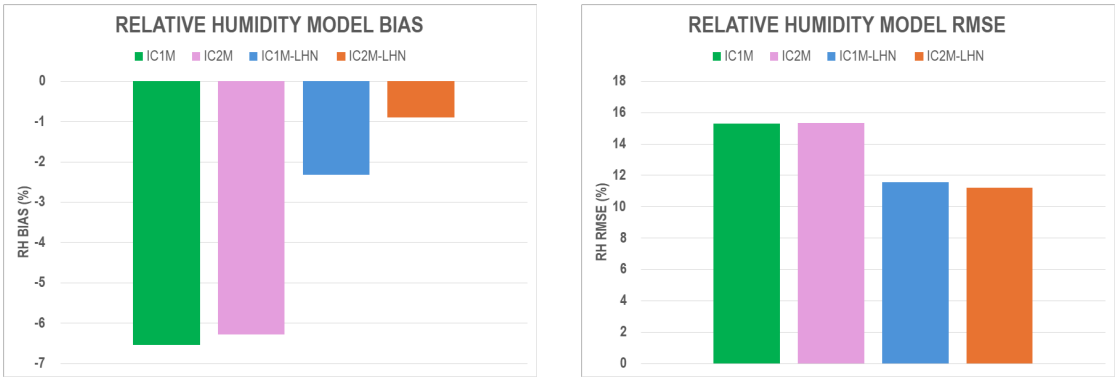

(a) Relative Humidity bias

(b) Relative Humidity RMSE

Figure 3.29: Statistical comparison of simulated and observed surface relative humidity across all ground stations and hours: (a) bias and (b) RMSE.

the supercell.

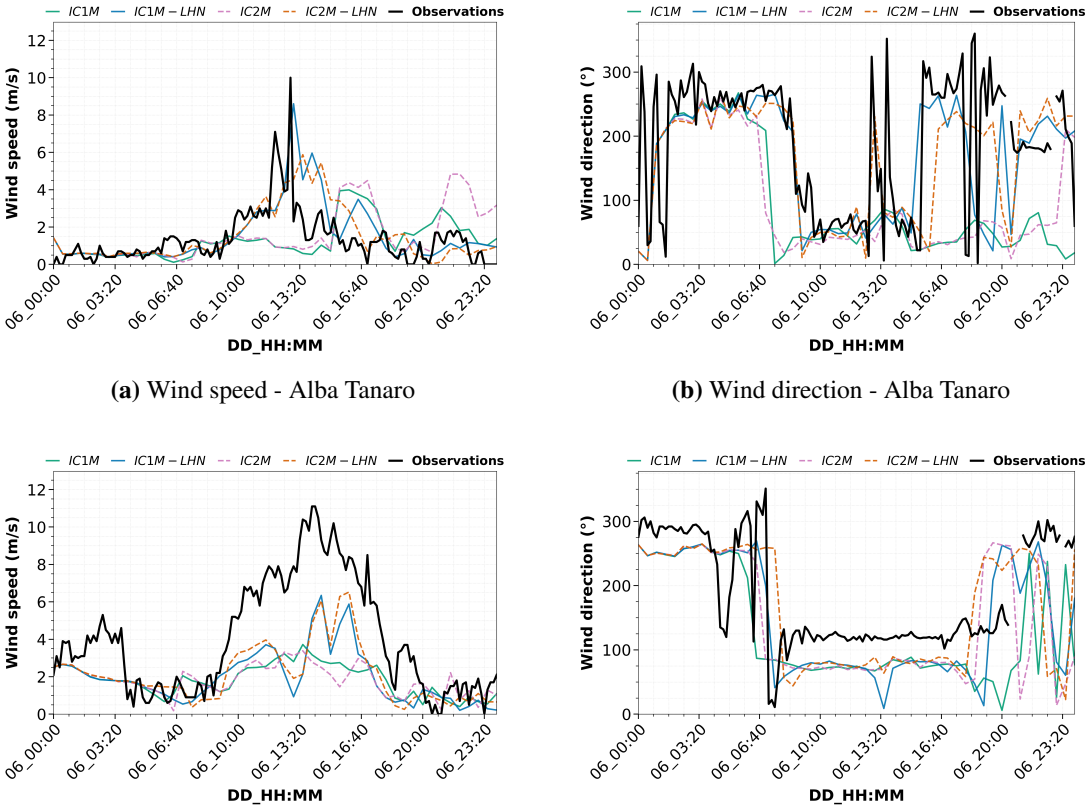

(a) Wind speed - Alba Tanaro

(b) Wind direction - Alba Tanaro

(c) Wind speed - Pietrastretta

(d) Wind direction - Pietrastretta

Figure 3.30: 24-hour temporal evolution of observed (bold line) and simulated (colored lines) surface wind speed (left panel) and direction (right panel) measured at the (top) Alba Tanaro and (bottom) Pietrastretta, Piedmont (Italy) ground weather stations on 6 July, 2023.

Further statistical analysis highlights significant noise in the data, as evidenced by the overall low (and, in the case of IC2M-LHN, extremely low) overall bias and high RMSE values (Fig. 3.31). This suggests the presence of large random errors in the simulation that compensate each other resulting in a low-biased model.

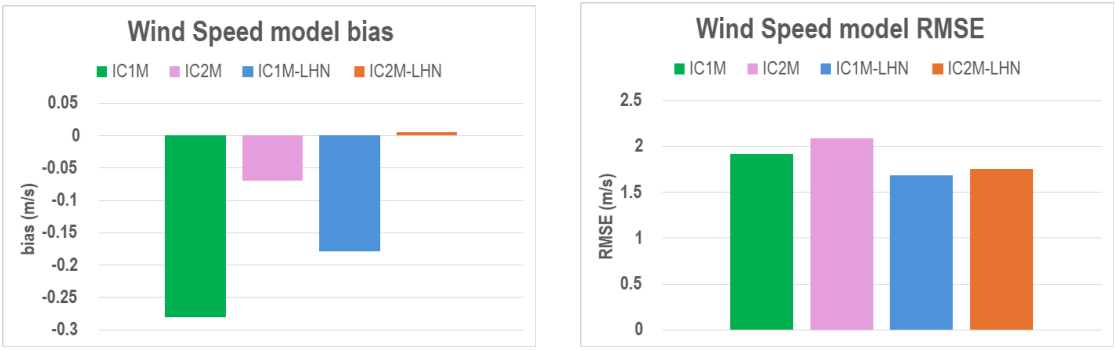

(a) Wind speed bias

(b) Wind speed RMSE

Figure 3.31: Statistical comparison of simulated and observed wind speed across all ground stations and hours: (a) bias and (b) RMSE.

3.2 Storm structure and microphysical analysis

The preceding analysis shows that the model alone, without data assimilation, fails to properly simulate the supercell, whereas LHN runs do it successfully. To evaluate the capability of ICON at high resolution in replicating the microphysical processes occurring inside a supercell under different parameterization schemes, only the LHN-assisted simulations are examined hereafter. For this investigation, we focus on the supercell observed at 1300 UTC to the southeast of Alba (CN), which captures the mature phase of the storm. Notably, the observed structure exhibits all the characteristic features of a supercell, providing a robust reference for model validation. The analysis begins with the identification of polarimetric signatures within the reflectivity field of the supercell. To this end, cross-sections of both the observed and corresponding simulated storm are evaluated, in both the horizontal and vertical planes. For the horizontal cross-sections the 2, 3 and 5 km CAPPI of reflectivity, obtained from the Monte Settepani (1386m Above Sea Level (ASL)) radar volume,

are compared with the reflectivity retrieved on model levels at equivalent height ASL. Given the location of the supercell at 1300 UTC and the height of the terrain-following model levels, the average region's height has been chosen with the aim to match the CAPPI's height ASL. This resulted in the selection of model levels 37, 32 and 25.

3.2.1 Hook echo signature

The hook echo signature is evident in Fig. 3.34a for IC1M-LHN but is nearly absent in IC2M-LHN, Fig. 3.35a, which exhibits a less defined supercell structure. Contrary to observations, where the high-reflectivity core remains confined within the FFD, reflectivity values above 56 dBZ in IC1M-LHN protrude inside the RFD region. In this regard, a partial improvement is observed for the IC2M-LHN simulation, which correctly spotlights the high refelctivity core in the FFD region although overestimating its values by producing peaks of reflectivity well above 70 dBZ, which could be correlated to the elevated hailstone surface density it produced.

3.2.2 The supercell's updraft

To georeferenciate the observed updraft, CAPPI products at multiple altitudes are analysed. With increasing heights above the LFC, the updraft exhibits progressive intensification as buoyancy forces are enhanced by the sustained temperature differential between the cooler ambient environment and the warmer ascending air parcel, the latter heated through latent heat release during condensation. This vertical acceleration is partially modulated by dry air entrainment from the surrounding environment, which

exerts a slight decelerating effect on updraft velocity while simultaneously contributing to horizontal broadening of the convective column. This process continues until the updraft encounters a temperature inversion and reaches the equilibrium level (tropopause), beyond which its velocity diminishes. By examining coordinated 2 km, 3 km and 5 km CAPPI cross-sections centered on the supercell, the updraft location ("X" in Fig. 3.32) is identified through diagnostically detecting a reflectivity transition. Indeed, the updraft core reveals itself through an absence of reflectivity at lower levels, indicating strong vertical air motion that inhibits hydrometeor growth, followed by a distinct onset of reflectivity aloft. This transition reflects updraft deceleration sufficient to permit water vapor condensation, thereby delineating the boundaries of the later-discussed *vault* region.

The geolocalization of the simulated updrafts is facilitated by the direct availability of three-dimensional velocity field data from the model. The region of interest is isolated by restricting the spatial domain to the atmospheric volume occupied by the supercell, as identified in the near-surface horizontal reflectivity field. Vertically, the model level corresponding to the peak updraft intensity is selected as representative of the entire ascending air column. The resulting relationship between updraft speed and height is illustrated in Fig. 3.33. The range of positive velocities reflects the first approximation value obtained when converting convective energy into kinetic energy while numerically adjusting for the entrainment, frictional drag and liquid-water loading effects on the rising air column [5], namely

$$w_{max} = \frac{\sqrt{2 \cdot CAPE}}{2} \tag{3.1}$$

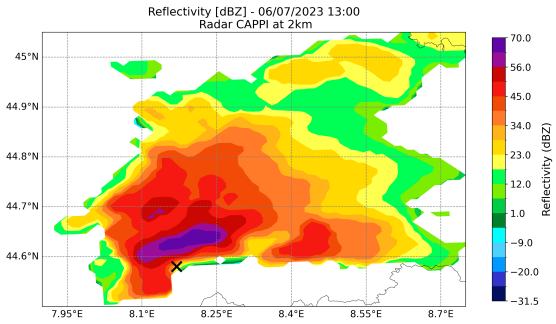

(a) 2 km CAPPI

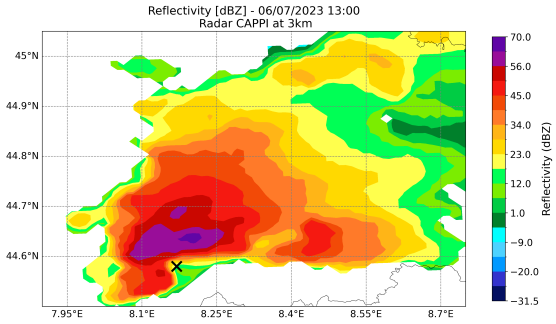

(b) 3 km CAPPI

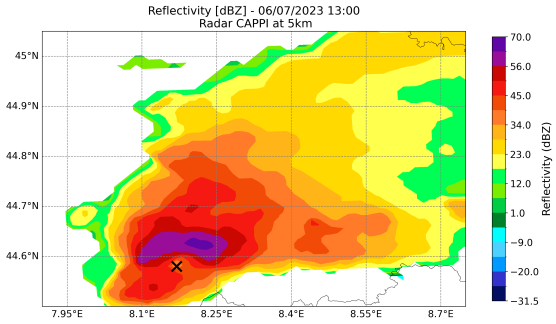

(c) 5 km CAPPI

Figure 3.32: Horizontal cross-sections of the reflectivity field produced by the supercell at 1300 UTC at (a) 2 km AGL, (b) 3 km AGL and (c) 5 km AGL as observed from the Monte Settepani weather radar (1386 m ASL). The "X" marks the updraft location.

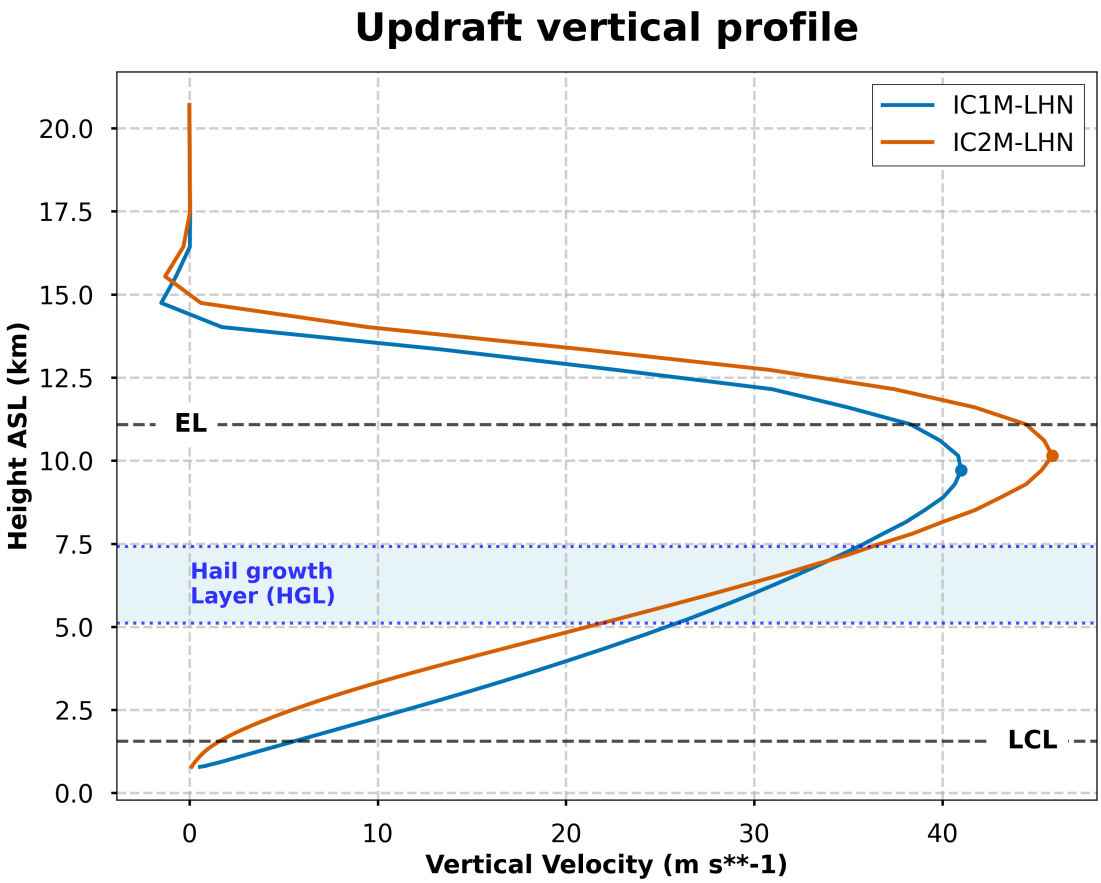

Figure 3.33: Vertical profile of supercell updraft as simulated by the single-(blu) and double-moment (orange) microphysics parametrisation schemes at 1300 UTC over Cortemilia (785m ASL). EL refers to the equilibrium level, or tropopause, retrieved from the SLE radiosounding at 1200 UTC

which produces, if substituting a $SBCAPE = 3044\,\mathrm{J\,kg^{-1}}$ (obtained from the SLE radiosounding at 1200 UTC), a maximum theoretical updraft speed of $w_{max} = 39\,\mathrm{m\,s^{-1}}$. The updraft in IC1M-LHN (blue curve) accelerates intensely in the first layers just above the plotted lifting condensation level (LCL) line, sympton of an overall quick response of the model to the production of hydrometeors. As a consequence, an immediate release of latent heat of condensation forces the air column to rise faster than

what is observed in the IC2M-LHN updraft. Although reacting slowlier, IC2M-LHN ultimately produces a more intense updraft than IC1M-LHN by 7.5 %, indicating the presence of microphysical processes with an higher potential of latent heat release. The production of large hail, as observed from the precipitated hail surface density field, suggests the presence in the updraft of an abundancy of supercooled liquid water droplets available for riming processes, thus supporting the wet growth regime, which eventually leads to the formation of large size hailstones. The intense riminig, characterizing the wet growth regime, allows for the releasing of abundant latent heat. In this region, shaded with light blue in the picture, we can indeed observe the closing of the vertical gap, in terms of updraft speed, between the hail predicting double-moment scheme and IC1M-LHN. The lack of observations prohibits a direct verification of the simulated updraft profile. The only reference is represented by the EL height which, although recorded an hour prior to the conducted updraft analysis and in a different location, should approach the height of updraft maximum intensity. Both IC1M-LHN and IC2M-LHN updrafts are correctly observed to start decelerating a few kilometers below the EL which, due to their inertia, are eventually able to cross with positive vertical velocity values, thus defining the characteristic overshooting top of severe thunderstorms. As done previously for the observations, we report an "X" mark, corresponding to the location of updraft maximum intensity, on the reflectivity fields at model levels 37, 32 and 25 in Fig. 3.34 for the single-moment scheme and in Fig. 3.35 for the double-moment scheme.

Neglecting the influence of the wind shear in tilting the updraft core, the horizontal distance between the simulated and observed updraft can

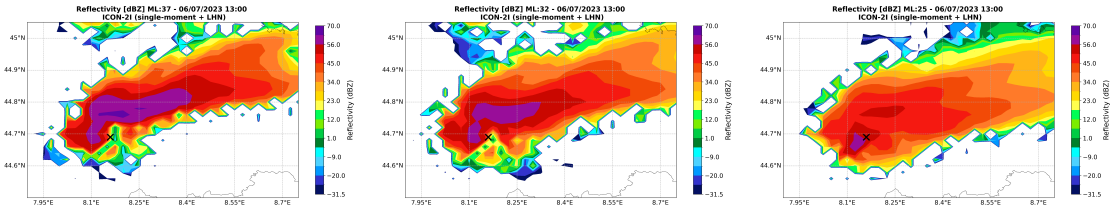

(a) IC1M-LHN at Model Level 37 **(b)** IC1M-LHN at Model Level 32 **(c)** IC1M-LHN at Model Level 25

Figure 3.34: Horizontal cross-sections of the reflectivity field produced by the supercell at 1300 UTC at model level (a) 37 (≈ 2 km AGL), (b) 32 (≈ 3 km AGL) and (c) 25 (≈ 5 km AGL) as simulated by IC1M-LHN. The "X" marks the updraft location.

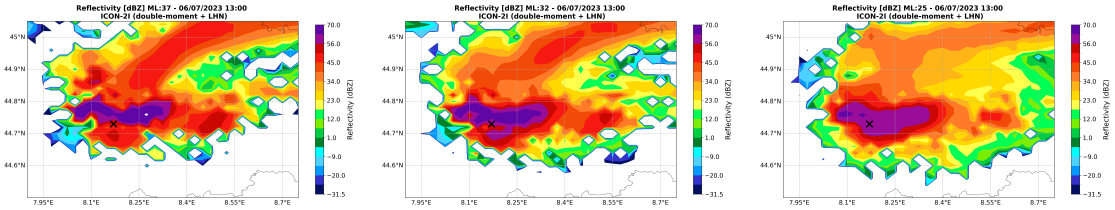

(a) IC2M-LHN at Model Level 37 **(b)** IC2M-LHN at Model Level 32 **(c)** IC2M-LHN at Model Level 25

Figure 3.35: Horizontal cross-sections of the reflectivity field produced by the supercell at 1300 UTC at model level (a) 37 (≈ 2 km AGL), (b) 32 (≈ 3 km AGL) and (c) 25 (≈ 5 km AGL) as simulated by IC2M-LHN. The "X" marks the updraft location.

be assessed applying the Haversine formula[2]. Both simulations exhibit a northward displacement of the updraft core compared to observations, with magnitudes of 12.25 km for IC1M-LHN and 16.66 km for IC2M-LHN. The greater offset of IC2M-LHN provides further evidence of the delayed response introduced by the double-moment scheme when assimilating latent heat data.

3.2.3 Weak Echo Region (WER) and Embryo curtain

The vertical cross-section of the observed supercell produced along its direction of travel (Fig. 3.36) clearly shows the embryo curtain and the BWER as distinct features in the reflectivity field. The vault is placed at 6 km ASL, far above the melting layer (4 km ASL), indirectly proving the presence of a strong updraft that locally inhibits hydrometeor formation. Following the vertical trajectory of the updraft, the overshooting top is encountered breaking out from the anvil clouds with the shape of a dome of reflectivity at 14 km ASL.

Fig. 3.37 shows the updraft horizontal cross-section of both simulations, evidenced by adopting a diverging colorbar for the scalar field of vertical velocity (W), superimposed on the vector field of horizontal velocity (U and V component). The model level here selected is that of maximum

[2]The Haversine formula calculates distances on a sphere using latitudes/longitudes. It employs the haversine function, $hav(\theta) = \sin^2(\frac{\theta}{2})$, and is numerically stable for small angles. For two points the distance d is:

$$d = 2R \arcsin\left(\sqrt{\text{hav}(\Delta\phi) + \cos\phi_1 \cos\phi_2 \,\text{hav}(\Delta\lambda)}\right), \tag{3.2}$$

where R is the Earth's radius, $\Delta\phi = \phi_2 - \phi_1$ is the latitude difference, and $\Delta\lambda = \lambda_2 - \lambda_1$ is the longitude difference.

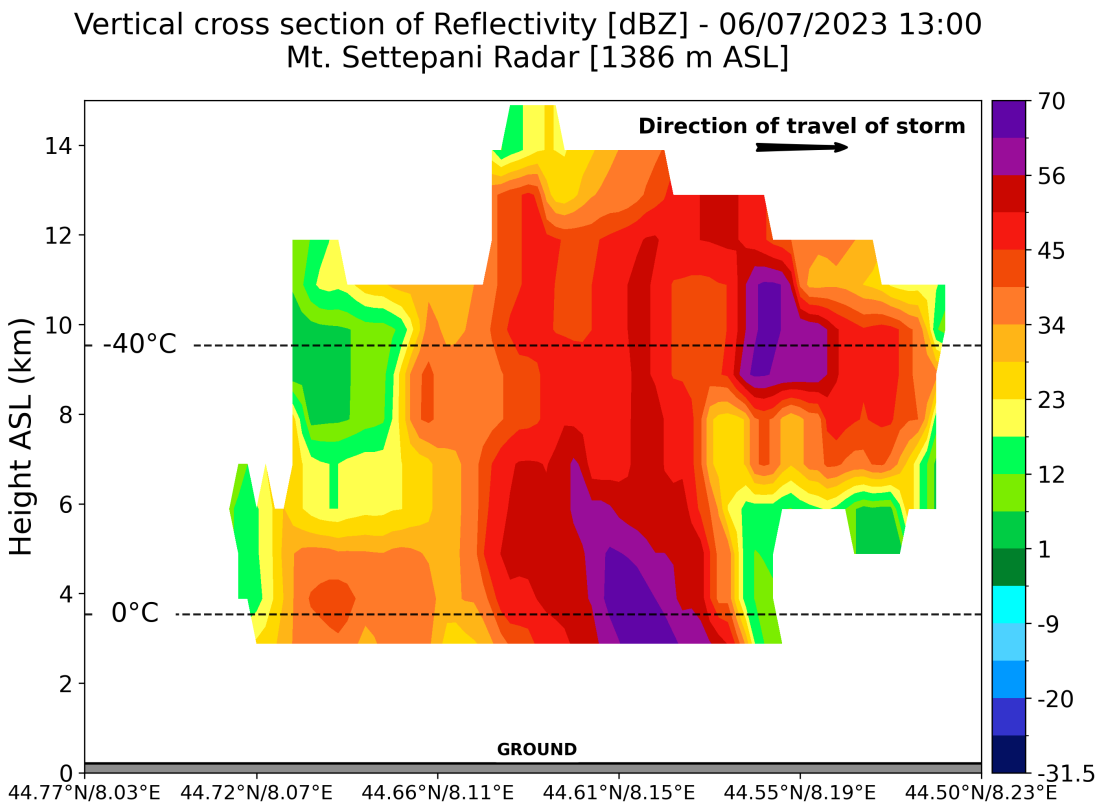

Figure 3.36: Vertical cross section of the reflectivity field produced by the supercell at 1300 UTC along the direction of travel of storm with mean ground level and 0°C and -40°C isotherms superimposed. The blank region between the ground and the first reflectivity radar echo is due to combination of radar height ASL (1386m) and first elevation angle available for the observations (2.1°) from a mountain terrain. Considering a distance of the storm of 40 km from the Monte Settepani weather radar, the first echo is signaled at 2.85 km ASL.

updraft intensity, retrieved from the preceding analysis. This cross-sections reveal the spatial extent and location of the updrafts, which are centered within the region bounded by maximum vertical velocity contours. A clear distinction emerges between the two models in terms of updraft core morphology relative to the ambient flow field. The updraft produced by IC1M-LHN has a leading edge resembling that of a blunt body, as proved by the significant deflection of the environmental flow field when

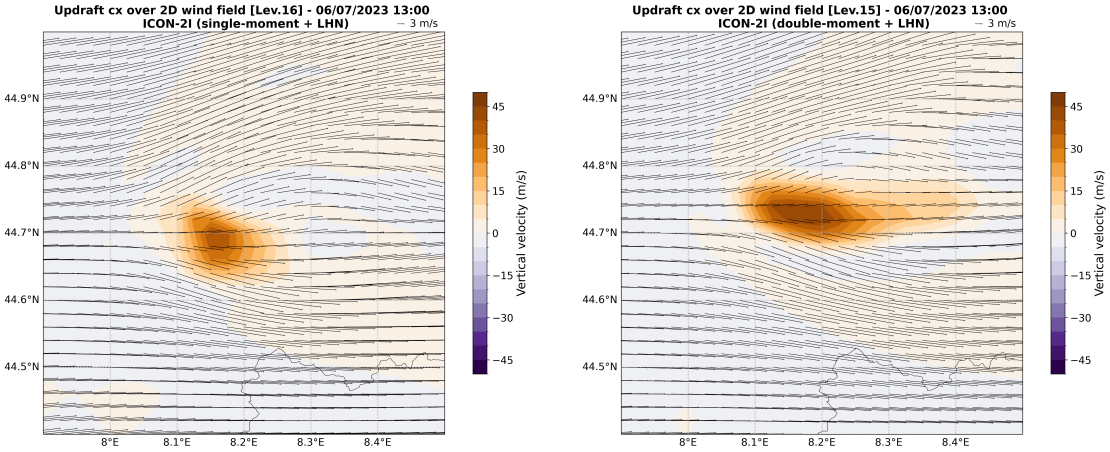

(a) IC1M-LHN **(b)** IC2M-LHN

Figure 3.37: Scalar fields of (left) IC1M-LHN at Model Level 16 and (right) IC2M-LHN at Model Level 15 simulated vertical velocity magnitude superimposed on the vector field of horizontal wind speed at 1300 UTC. Blue indicates downdrafts while red indicates updrafts.

getting around it. This pronounced deflection promotes the development of a long wake. In contrast, the IC2M-LHN simulation develops a more aerodynamically streamlined updraft that interacts more gently with the surrounding airflow.

The strong aerodynamic interaction between the mean level winds and the single-moment simulated supercell's updraft is better visualized with a North to South vertical cut as in Fig. 3.38b. Here, the overhang reflectivity pattern, to the mesocyclone's flank, is clearly evident although not directly attributable to the presence of hail embryo, since hail category is not predicted, but raher to graupel.

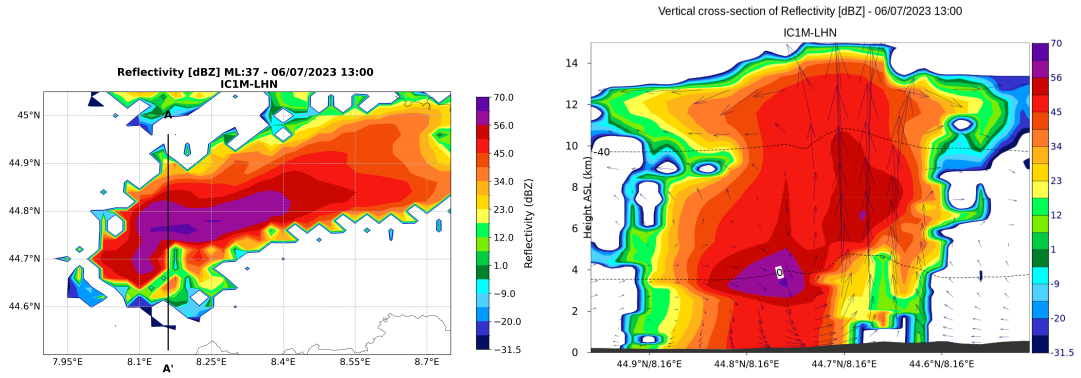

(a) **(b)**

Figure 3.38: (left) Horizontal cross section at Model Level 37 of the IC1M-LHN simulated reflectivity field at 1300 UTC. The black segment A'A is the reference cutting line for the vertical cross-section. (right) Vertical cross section along the A'A segment showing the reflectivity field inside the supercell.

To account for the delay in the reaction of the double-moment scheme to the LHN assimilation, a five minutes margin is given by considering the reflectivity field, which is therefore retrieved at 1305 UTC. The weaker aerodynamic interaction occurring between the double-moment simulated updraft and environmental airflow produces a less defined embryo curtain, as observed in Fig. 3.39b. Nonetheless, hail is produced in large amounts.

The elevated reflectivity horizontal gradient, ranging from above 60 dbZ down to radar echo devoid, marks the outside boundary between the weak echo region and the FFD.

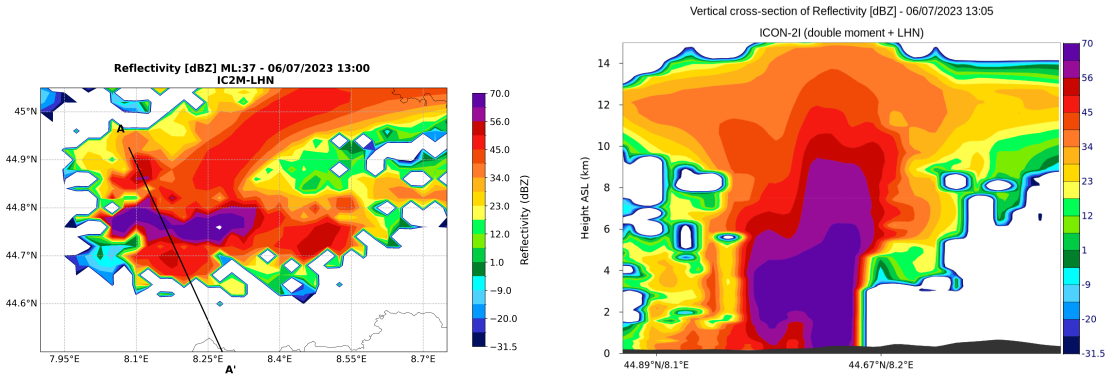

(a) **(b)**

Figure 3.39: (left) Horizontal cross section at Model Level 37 of the IC2M-LHN simulated reflectivity field at 1300 UTC. The black segment A'A is the reference cutting line for the vertical cross-section. (right) Vertical cross section along the A'A segment showing the reflectivity field inside the supercell.

In both simulations, the *vault*, highlighted by a defined arch structure, is recorded at an height of around 5km ASL, denoting a substantial difference with the observation. Analysing the wind field resulting from the cross-section, vectors pointing upwards and increasing in length denote the presence of a strong updraft that deflects the isotherms, as evidenced by the omega shape assumed by the 0°C and -40°C isotherms at the interesection with the updraft. The result is a localized upward shift of the 0°C isotherm layer by around 1 km, seemengly reproducing the upper vault bending. The strenght of the updraft is such that initiation of condensation within its core is delayed enough not to occur immediately in correspondence of the LCL but coincidently with the melting layer, where the updraft is still accelerating. Condensed particles, therefore, avoid a fast ejection from the updraft core into the anvil as crozen crystals but, have higher chances of

being horizontally advected across the updraft by mean winds.

3.2.4 The hail core

Large hail production by the supercell is confirmed by the distinct column of high reflectivity values (in purple in Fig. 3.36), constituting the hailfall region observed in the FFD. Its apparent tilted structure arises from the 5-minute temporal resolution of the Monte Settepani radar's full-volume scan, during which the supercell advances by a few kilometers, artificially displacing the observed position of hydrometeors between successive elevation angles.

A similar feature is observed when considering the vertical cross section of IC1M-LHN reflectivity field. The vertical trajectory of hydrometeors that produce the high reflectivity core, observed in Fig. 3.38b, tracks a cyclonical trajectory, instead of a straight vertical path to the ground, under the influence of the strong rotating updraft. For this reason the cutting section is not perfectly aligned with the direction of storm travel, along which we would expect to find the bulk of precipitation. Instead, it follows an almost easterly trajectory passing through the updraft nucleus in such a way that the rain shaft within the RFD is entirely captured, as Fig. 3.40b shows. Simulated values here don't exceed 60 dBZ.

The high-reflectivity core simulated by the double-moment scheme shows values exceeding 60 dBZ, which is a clear sign for the presence of hail. Fig. 3.41 presents the vertical distribution of maximum reflectivity, along with its 25th, 50 th (median) and 75th percentiles, derived from storm observations within the supercell development region. Tracking the maximum reflectivity across all altitudes allows for the characterization of the hail core evolution.

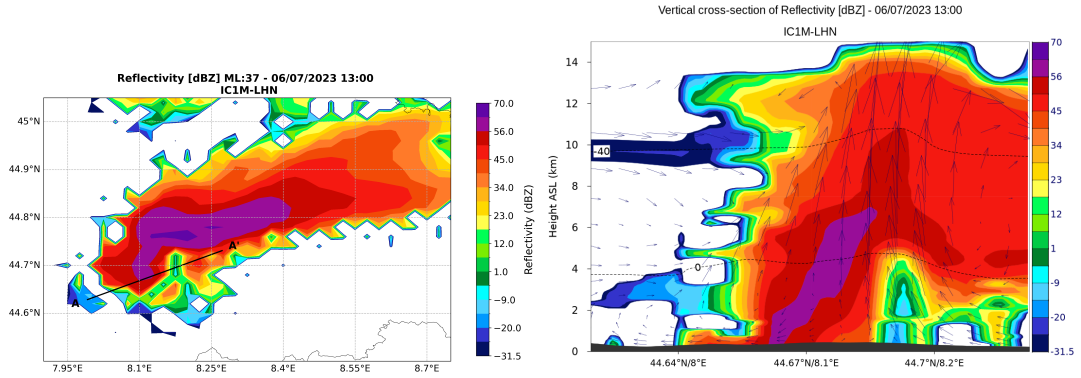

(a) **(b)**

Figure 3.40: (left) Horizontal cross section at Model Level 37 of the IC1M-LHN simulated reflectivity field at 1300 UTC. The black segment A'A is the reference cutting line for the vertical cross-section. (right) Vertical cross section along the A'A segment showing the reflectivity field inside the supercell. Here, the high-reflectivity core is captured in its entirety

A significant discrepancy is observed between the IC1M-LHN simulation and radar-derived maximum reflectivity values, across much of the storm depth, with an average offset of approximately 10 dBZ. This is primarily attributed to the absence of a hail category in the microphysical scheme. The implementation of IC2M-LHN substantially reduces this discrepancy, narrowing the gap to 5 dBZ and achieving nearly perfect agreement below 5 km ASL, where the high-reflectivity core develops. Analysis of median reflectivity profiles (dashed curves) reveals a persistent divergence between simulated and observed values, though with an inverted bias: the simulations now exhibit systematically higher reflectivities, suggesting excessive hydrometeor production in the model. A notable distinction emerges in the melting layer dynamics. The single-moment scheme (IC1M-LHN) exhibits an abrupt negative gradient in reflectivity, indicative of rapid graupel-to-rain conversion and subsequent raindrop evaporation. In contrast, IC2M-LHN produces a more gradual profile,

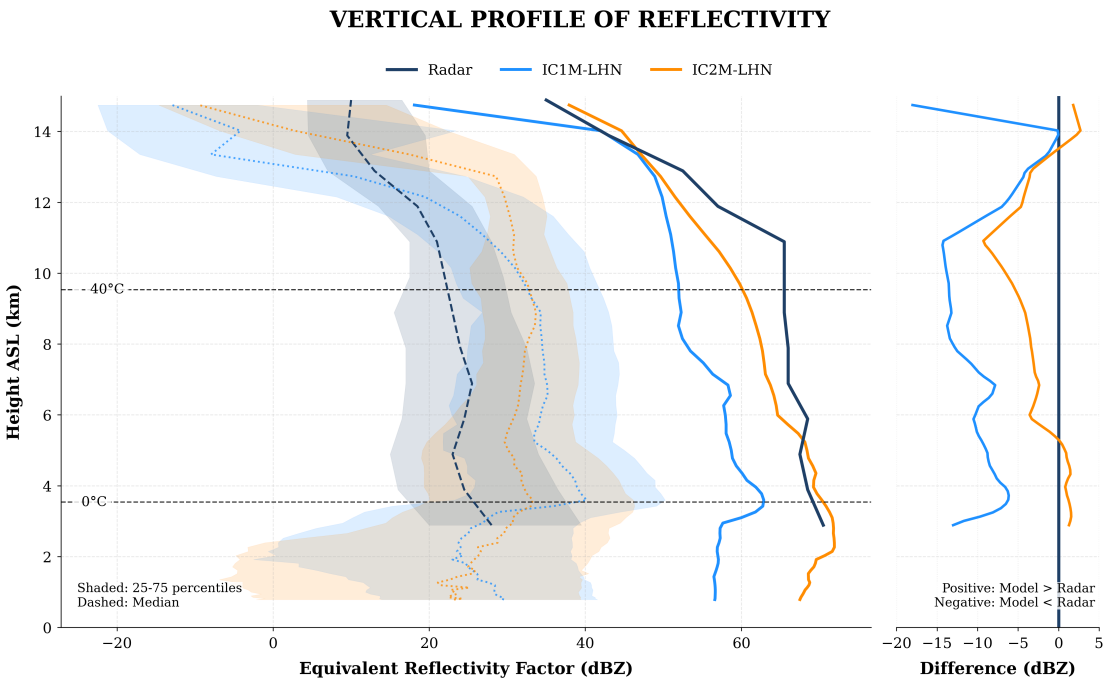

Figure 3.41: Vertical profiles of maximum reflectivity (dBZ) for (black) observation, (blue) IC1M-LHN and (orange) IC2M-LHN and difference between model and simulations on the secondary y axis. Respective shaded areas are comprised between the 25^{th} and 75^{th} percentiles of reflectivity with a dashed line in the middle to represent median values. 0°C and -40°C isotherms are taken from the 1200 UTC SLE radiosounding.

better aligned with observations. This discrepancy is linked to the steep decline in relative humidity from the freezing level to the surface within the RFD, as captured by the 75^{th} percentile of relative humidity in Fig. 3.42. IC1M-LHN simulates stronger downdrafts, which adiabatically compress mid-level air more intensely. Consequently, precipitation entering the RFD encounters a drier layer, leading to faster initial evaporation, greater mass loss, and a more pronounced reduction in reflectivity.

The double-moment microphysics scheme locates the reflectivity peak of the hail core approximately 2 km below the melting layer. As hydrometeors descend through the melting layer, their phase change from ice to liquid

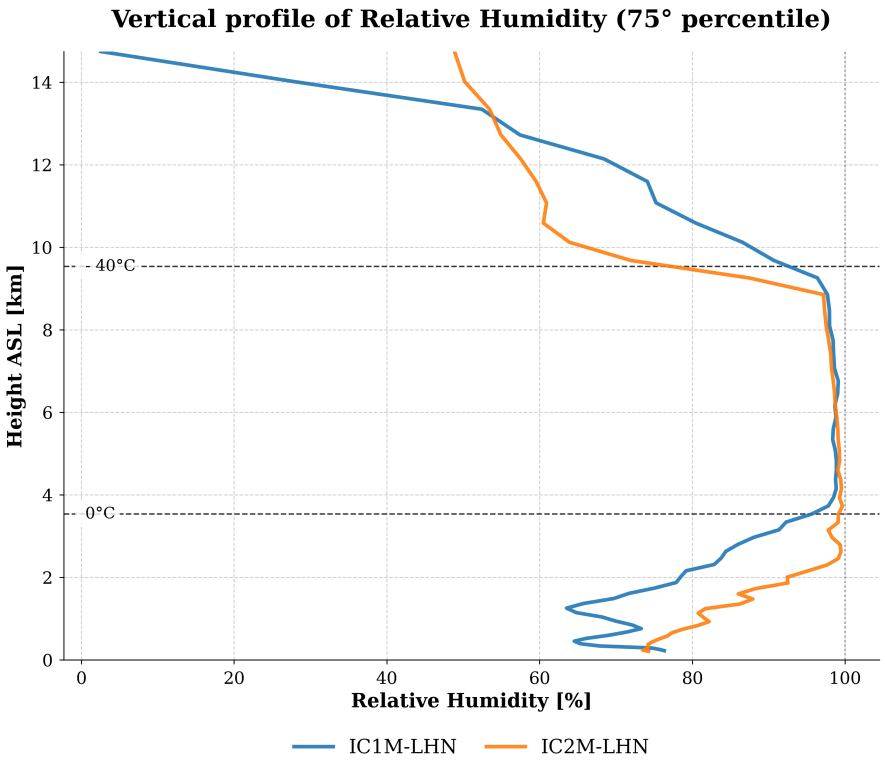

Figure 3.42: Vertical profiles of relative humidity (%) for (blue) IC1M-LHN and (orange) IC2M-LHN. 0°C and -40°C isotherms are taken from the 1200 UTC SLE radiosounding.

water produces a characteristic reflectivity enhancement, primarily due to the increased dielectric constant of liquid water ($\epsilon \approx 73$ at 20°C and C-band) compared to ice ($\epsilon = 3.17$). This results in a gradual reflectivity increase with decreasing altitude until ice shedding processes become dominant. Beyond this point, the reduction in hailstone size leads to decreasing reflectivity values. This behaviour is partially outlined in the observed reflectivity profile, although the lack of data recorded below 3 km ASL, due to radar constraints, prohibits a direct comparison up to ground level.

3.2.5 Hydrometeors composition

The following analysis investigates the supercell hydrometeor's composition of both IC1M-LHN and IC2M-LHN simulations and compares it to those derived by applying the PID algorithm to the reflectivity field produced by the Monte Settepani weather radar at 1300 UTC. The hydrometeors' distribution within the simulated supercell structure is investigated by retrieving vertical cross sections of the mixing ratio and associated area-averaged vertical profiles. The same concept is applied to the observations, with the difference that no information is available on the mixing ratio. This time we can only rely on the total count of hydrometeors detections inside the radar volume. For this reason, the comparison regarding hydrometeors can only be qualitative.

In continuity with the vertical cross-sections of reflectivity fields, the direction of storm travel is selected as preferential direction of analysis. This should allow for the visualization of hydrometeors' formation inside the supercell updraft as well as the composition of the downdraft regions. In order to visualize the different hydrometeors categories produced by the algorithm and the model, a unified color code is assigned to each, following the convention adopted by ARPA Piemonte, shown in Fig. 3.43 Only the categories of rain, graupel, wet snow, ice crystals and, additionally, hail for IC2M-LHN have a model predicted counterpart. The remaining observed categories, including drizzle, large drops, heavy rain, rain-hail mixtures, dry snow and non meteorological echoes are not forecasted by the model. With the aim of comparing the model with the radar, it is necessary to re-emphasize the technical and physical constraints of the weather radar affecting the reflectivity measurements with repercussions on the PID algorithm accuracy, which is already influenced

Figure 3.43: Color codes adopted by ARPA Piemonte to distinguish between hydrometeors categories when the PID algorithm is applied to the polarimetric radar variables.

by inherent approximations. Furthermore, the algorithm recognizes only one hydrometeor category inside the finite atmospheric volume analyzed whereas, in reality, different phases and classes overlap.

The image presented in Fig. 3.44 shows the hydrometeors' vertical cross-sections obtained from the PID algorithm (on the left) and the IC1M-LHN predicted hydrometeors mixing ratio fields (on the right). In compliance with the unfeasibility of the PID algorithm to characterize the intensity levels of each hydrometeor, also the cross-section of simulated fields does not discrimate between spatial variations in the mixing ratio. At least at this point in the analysis, no information on the hydrometeors's intensity distribution is provided, but a general information regarding

the type of hydrometeors predicted and their vertical extension. Above the level of homogeneous freezing (-40°C isotherm), inside the anvil, only crystals, dry snow and graupel are observed. This is consistent with the predictions of IC1M-LHN, which correctly simulates the same frozen hydrometeors categories. In both cross-sections, graupel grains are found inside the anvil plume up to an height of 14 km, coincident with the echo top, after being subjected to intense updrafts. Referring to IC1M-LHN, a few hundreds of meters below the freezing level, the entire precipitating graupel content melts completely producing a massive rain shaft, further proof of the presence of a dry layer of air at low levels that inhibits any ice derivatives to reach the ground without complete melting. Graupel melting into rain before precipitating to the ground characterizes part of the observed liquid precipitation field, the remaining being constituted by melting of dry snow, unobserved phenomenon in the IC1M-LHN simulation. Wet snow patterns are observed as an intermediate phase during melting of dry snow into rain, at far distances north of the FFD, and at the edge of the updraft which allows them to protrude higher above the mean melting layer height. The substantial difference between IC1M-LHN's and the observed supercell, though, is represented by the absence of the hail core, in yellow, whose category is not predicted at all by the single-moment scheme. Nonetheless, the other supercell features are mostly well simulated, starting from the BWER to the embryo curtain. The BWER, updraft signature in the reflectivity field, correcly translates into a devoid of hydrometeors, as proved by the white column in the observed cross-section extending up to almost 6 km ASL next to the hail shaft and surmounted by dry snow and graupel. A similar pattern is present in IC1M-LHN, which is located in correspondence of the ripple of the

freezing layer, topped by rain and graupel at about 4 km ASL. The embryo curtain overhanging on the western flank of the observed mesocyclone is composed mainly of graupel and, to a minor extent, of dry snow and ice crystals serving as hail embryo later injested by the updraft. Its simulated counterpart, showing a lesser defined structure, contains graupel and rain. From a first look, the single-moment scheme seems to predict liquid water above the melting layer, in the form of supercooled raindrops, at heights greater than those observed from the radar, namely 8 km ASL instead of 6 km ASL. This could be attributed to underestimations of the vertical distribution of active contact freezing nuclei, which is assumed to decrease linearly from a surface value to a background concentration in 500 hPa. This could affect the number of ice crystals at low subfreezing heights available to supercooled raindrops for contact freezing.

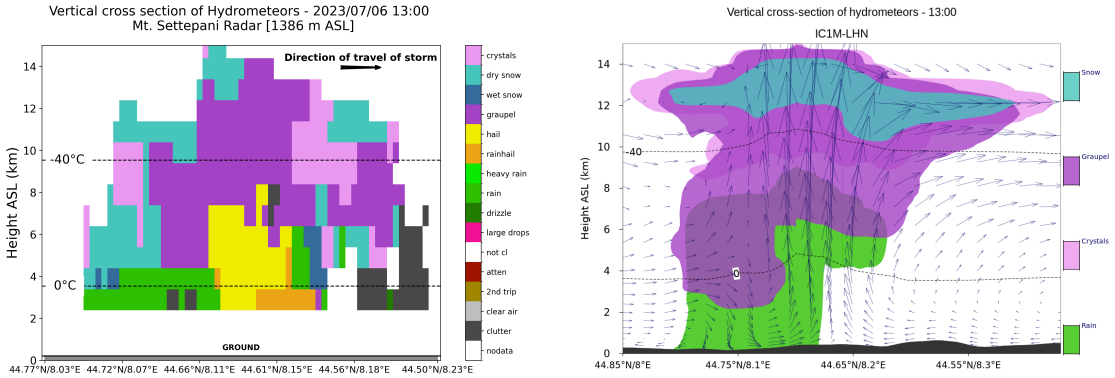

(a) Observations **(b)** IC1M-LHN

Figure 3.44: Hydrometeors vertical composition as obtained from the (left) PID algorithm (applied to Monte Settepani weather radar's derived polarimetric variables) and from the (right) EMVORADO operator on IC1M-LHN (processed with the MetView tool)

The IC2M-LHN model successfully reproduces the hail category, as demonstrated in Fig. 3.45. However, the simulated hail core (yellow region) exhibits an anomalously deep vertical extent, spanning the entire

storm depth. This contrasts sharply with radar observations, which confine hail to regions below the homogeneous freezing level. Such a discrepancy points to potential inaccuracies in the parameterization of hail formation processes. Given that the model's updraft velocities are consistent with observations (as established earlier), the overprediction of elevated hail likely stems from an overly aggressive riming rate in the microphysics scheme. Specifically, the parameterization permits rapid accretion of ice crystals onto hail, produced from freezing of raindrops belonging to the higher end of the particle size spectrum (as established in the revised double-moment scheme [42]), at rates comparable to their updraft-driven ascent velocities. This enables hail growth within the updraft core, a region typically dominated by ice crystals and graupel. The resulting small hailstones remain suspended, passively advected into the anvil region rather than sedimenting out. Supporting this hypothesis, the model simulates hail directly atop the vault region, near the 0°C isotherm where raindrop freezing is permitted, given the -3°C activation threshold for this process. To further improve the simulation of certain hail formation processes (e.g., melting, recirculation, refreezing), a more realistic treatment of melting and shedding is needed, likely feasible if including the prediction of the water fraction of melting particles instead of immediately transfer it to the rain category. The "rainhail" category, in orange, is not directly predicted by the microphysics scheme, although a region where hail and raindrops overlap is captured by IC2M-LHN. With respect to the single-moment scheme, a larger dry snow region is simulated, although its vertical extension remains confined within the anvil, having therefore a negligible influence on hail formation processes as instead happens in the observed supercell, where dry snow popolates the embryo curtain. From this perspective (North-West

South-East cut) it is clearly visible the deflection of the mean westerly upper winds, following their interaction with the updraft, which reproduces the embryo curtain in the IC2M-LHN simulated supercell. The vault is recognizable in that it hosts the intense updraft, as confirmed by long wind vectors pointing up, sustained by a low level wind convergence, and the upward ripple in the isolines of temperature.

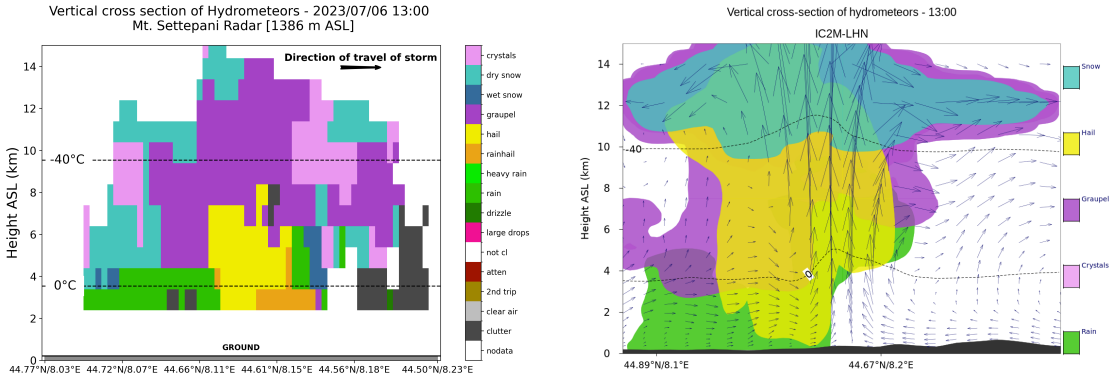

(a) Observations **(b)** IC2M-LHN

Figure 3.45: Hydrometeors vertical composition as obtained from the (left) PID algorithm (applied to Monte Settepani weather radar's derived polarimetric variables) and from the (right) EMVORADO operator on IC2M-LHN (processed with the MetView tool)

The simulated and observed hydrometeors' vertical normalized distributions are plotted altogether for each category common to both microphyics schemes and the PID algorithm (rain, snow, ice crystals, graupel and hail) with the aim of comparing their shapes. Informations on the prognosed mean hydrometeors vertical amounts are provided as area averages of their mixing ratios in a dedicated plot. For reasons of compatibility between model and observed data, the only feasible comparison is through a simple, yet effective, summation of the number of detections of each specific hydrometeor species inside the analysed volume. As a consequence, such profiles reflect the statistics of the hydrometeors' number density

distribution, which is mostly uncorrelated with respect to the total mass distribution. For every hydrometeors' category, a minimum detection threshold of $1 \cdot 10^{-6}$ is adopted. The model and observed profiles are further normalized with respect to the maximum number of detections. The densest population of the hydrometeor under investigation is indicated by peaks in the profiles, integrated with height and temperature information.

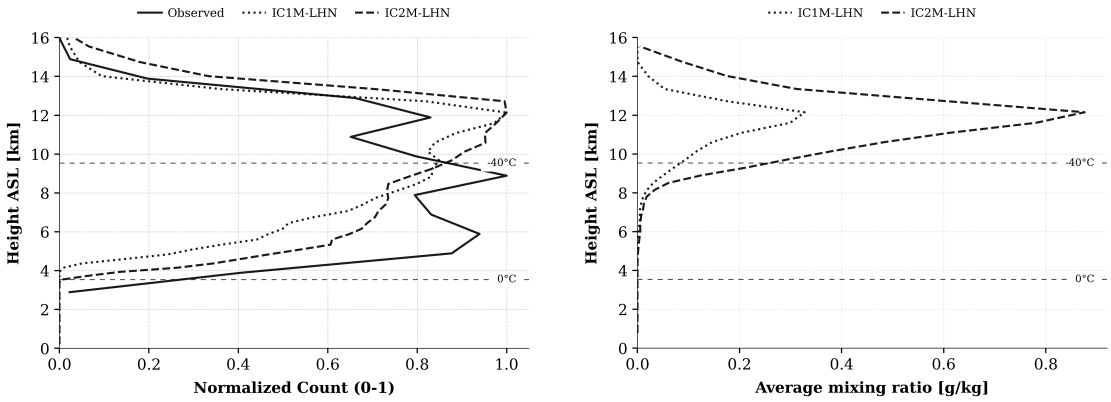

Figure 3.46: (left) Normalized vertical profiles (0-1 scale) of ice crystal detections per layer within the supercell at 1300 UTC, excluding concentrations below $1 \cdot 10^{-5}$. (right) Vertical profiles of simulated graupel mixing ratios averaged across the supercell domain at 1300 UTC.

The observed profile of the ice crystals exhibits a trimodal distribution, which suggests the presence of atmospheric layers in which ice grows and accumulates preferentially within the supercell. Following the categorisation scheme for ice crystals proposed in [43] and shown in Fig. 3.47, the first peak at around -17°C, temperature where the Dendritic Growth Regime (DGR) is most active, may indicate intense ice growth through the deposition of water vapour in the supersaturated environment of a convective updraft. This occurs rather than at the expense of drops inside the cloud (the Wegener-Bergeron-Findeisen process), which is observed

instead for very low updraft speeds in stratus clouds. This hypothesis, derived from recent cloud modelling calculations [44], is corroborated by analysing the vertical profiles of the simulated cloud water mixing ratios of the two microphysics schemes, which peak at the same altitude of 6 km ASL, although a similar local peak in the ice crystals profile is not captured.

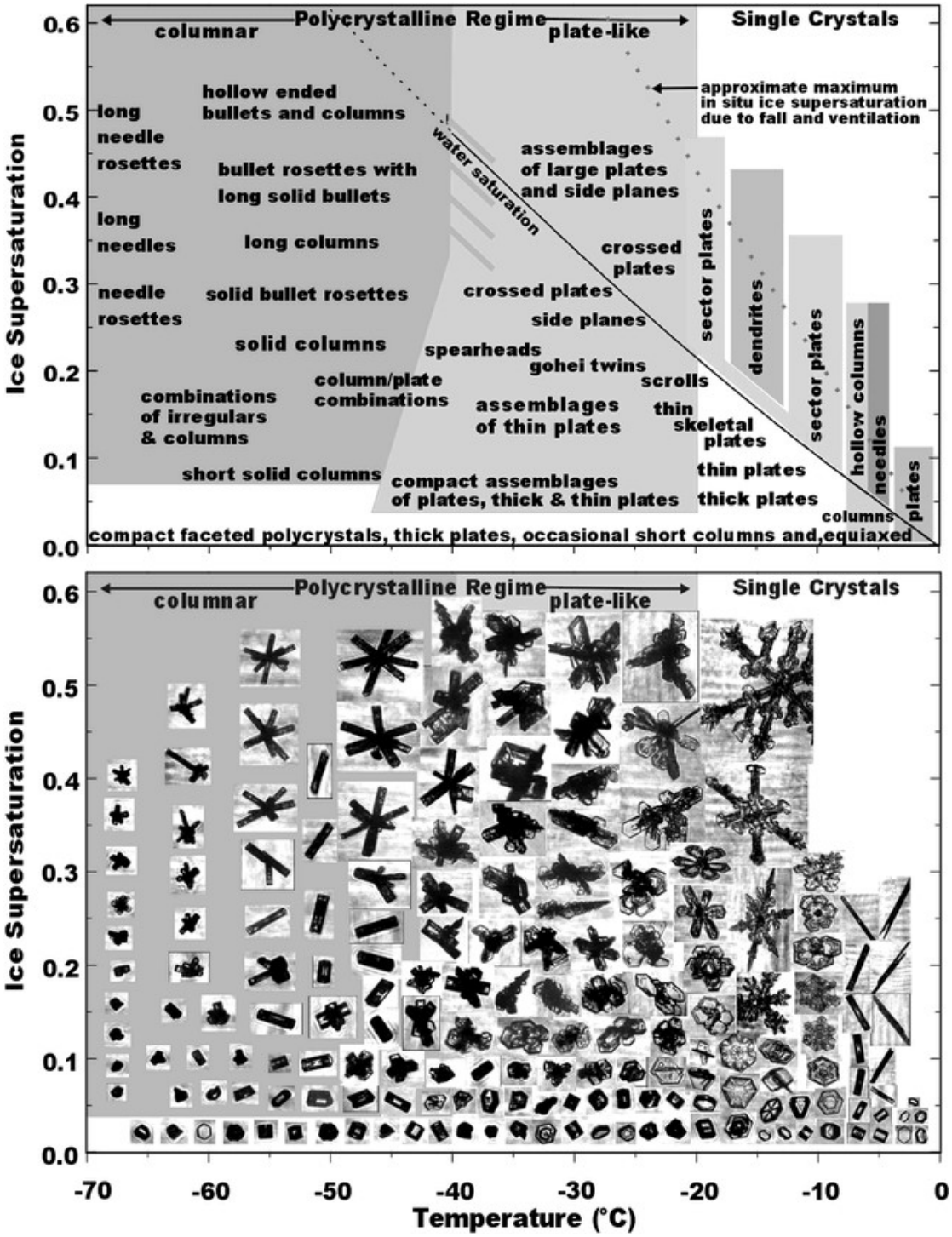

Figure 3.47: Diagram showing the morfology of ice crystals and ice aggregates as function of the temperature and of the supersaturation with respect to ice. Source: Bailey, Matthew P., and John Hallett. "A comprehensive habit diagram for atmospheric ice crystals: Confirmation from the laboratory, AIRS II, and other field studies." Journal of the Atmospheric Sciences 66.9 (2009): 2888-2899.

Polycrystalline ice habits are found at almost all levels of ice supersaturation above the DGR. A correlation between the intermediate ice crystals peak and that of the snow profile is suggested by considering the profiles in Fig. 3.48, which could indicate intense riming activity at the top of the updraft, resulting in the production of large quantities of dry snow aggregates. This correlation is also present in the simulated snow and ice crystal profiles of both microphysical schemes, although it shifts upwards to 12 km ASL where the temperature is -50°C. The third peak in the ice crystal vertical profile is encountered at this level. Based on the ice habits categorisation, this peak represents small columnar crystals formed by the homogeneous nucleation of cloud droplets, which appear to be the dominant source of ice crystals in the simulations, as observed in Fig. 3.46.

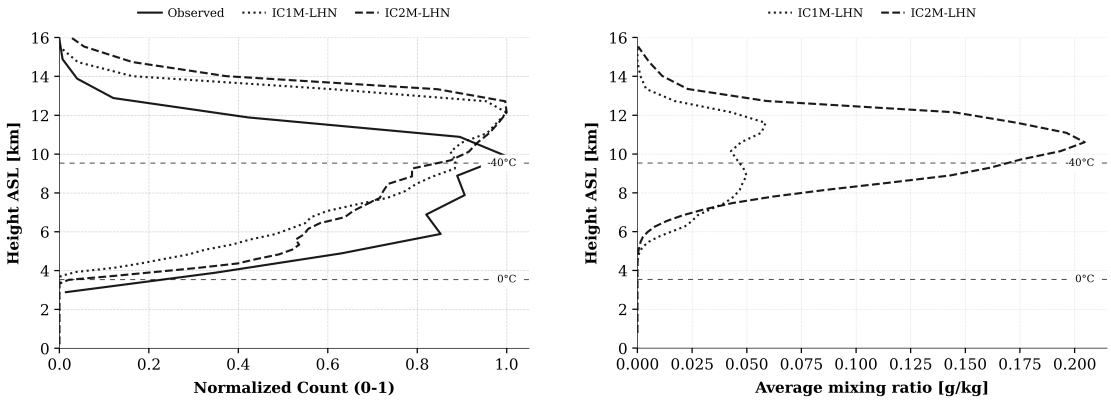

Figure 3.48: (left) Normalized vertical profiles (0-1 scale) of snow detections per layer within the supercell at 1300 UTC, excluding concentrations below $1 \cdot 10^{-5}$. (right) Vertical profiles of simulated snow mixing ratios averaged across the supercell domain at 1300 UTC.

It is generally accepted that at -20 °C the percentage of clouds consisting entirely of supercooled drops reduces to 10 %, which tells the temperature

where most of the supercooled drops have nucleated and grown into ice derivatives. In this context, the −20 °C isoline is found at 6.7 km ASL where, indeed, most of the supercooled water is frozen, as seen in Fig. 3.49 (left). This observed behaviour contrasts with the results of the microphysics schemes, which show an unusually high number of supercooled raindrop targets. The average mixing ratio profiles in Fig. 3.49 (right) confirm that this trend also occurs with the mass density variable. Referring to these curves again reveals two interesting facts: firstly, the single-moment scheme predicts an overall raindrop density that is four times greater. The gap between the two curves widens within the hail growth region, which is between 7.5 and 5 km ASL. Many large raindrops freeze into the hail category, as predicted by the revised IC2M scheme, thereby reducing the liquid content. This cannot occur in the single-moment scheme, where raindrop density increases slightly before reducing at low levels. Secondly, while the number density reduces correctly below the melting level — a symptom of drop evaporation — the mass density profiles exhibit an unexpected increase. A monotonic decrease would be expected as a result of evaporation and shedding. This behaviour could be explained by the suggestion that a large amount of graupel mass melts before reaching the ground, thereby increasing the mass of raindrops. This is particularly evident in the single-moment scheme, whereas it is less pronounced in the double-moment scheme, likely because graupel is involved in hail growth processes as an embryo.

The observed graupel vertical distribution is centered in the $-40\,°\mathrm{C} < T < 0\,°\mathrm{C}$ temperature range, where the most of hail production occurs as later confirmed by analysing the hail profile. Decrease of graupel particles outside this range is either due to melting processes or gravitational

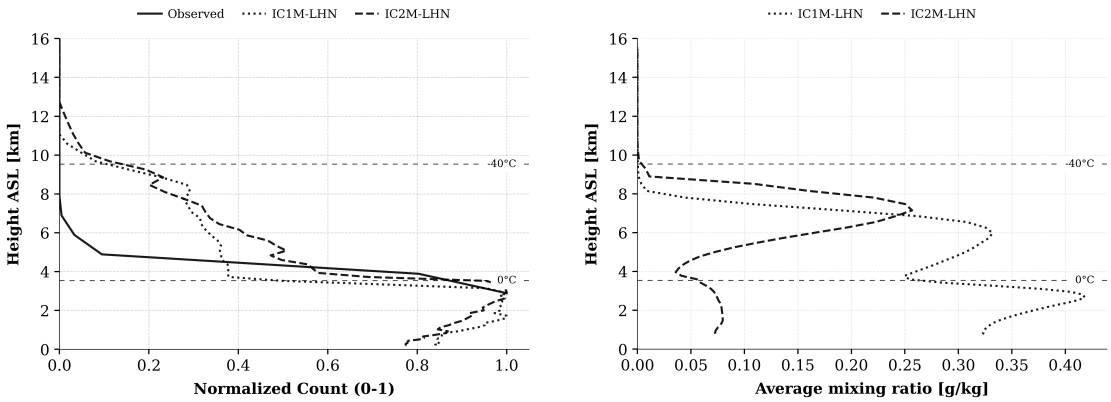

Figure 3.49: (left) Normalized vertical profiles (0-1 scale) of raindrop detections per layer within the supercell at 1300 UTC, excluding concentrations below $1 \cdot 10^{-5}$. (right) Vertical profiles of simulated raindrop mixing ratios averaged across the supercell domain at 1300 UTC.

settling. It results from Fig. 3.50 (left) that graupel particles produced in the IC1M-LHN simulation cannot survive the falling environment, their last detection being at 2 km ASL, and melt completely before reaching the ground. Instead, a non negligible amount of graupel particles produced by IC2M-LHN remains intact up to the surface after enduring a substantial reduction in mass and number during melting, as confirmed by the near zero average mixing ratio of the IC2M-LHN profile in Fig. 3.50 (right).

The IC2M-LHN model simulates the densest hail population above the homogeneous freezing level, as shown in Fig. 3.51 (left), suggesting the presence of a large number of small hailstones suspended aloft by the updraft. The majority of hail mass production, though, as observed in Fig. 3.51 (right), is coincident with the radar-derived profile. This peak lies between the -40°C and 0°C isolines drawn in the picture, which falls inside the region of most intense hail growth due to the presence of the majority of supercooled drops. The analysis of the temperature profile

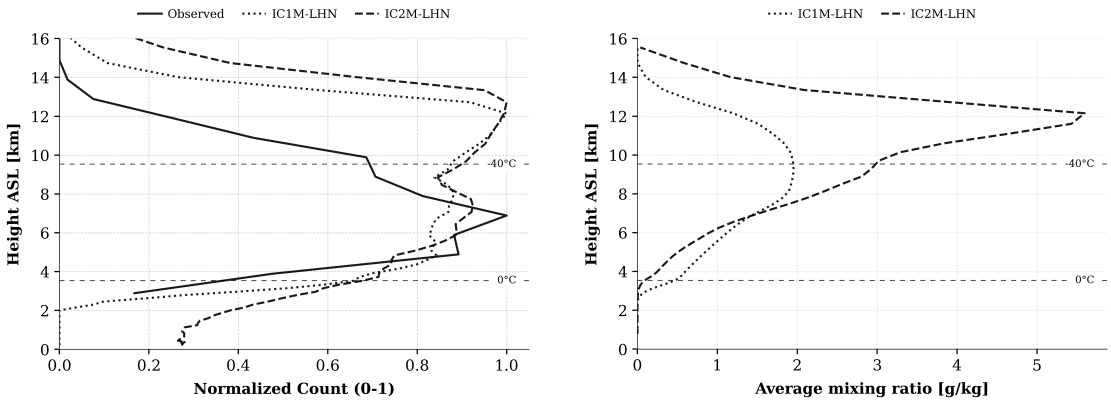

Figure 3.50: (left) Normalized vertical profiles (0-1 scale) of graupel detections per layer within the supercell at 1300 UTC, excluding concentrations below $1 \cdot 10^{-5}$. (right) Vertical profiles of simulated graupel mixing ratios averaged across the supercell domain at 1300 UTC.

below the freezing level, in Fig. 3.52, shows that the air cools much more in the IC1M-LHN simulation than in the IC2M-LHN one. Cooling of the air in presence of a precipitation loaded downdraft below the base of a cold cloud is due to the absorption from the environment of the latent heat of melting and of vaporisation. Precipitating ice particles of the single-moment scheme are mainly constituted by graupel, which is characterised by ice particles with a maximum allowed diameter of 5 mm, whereas the precipitating ice category of IC2M-LHN comprises hailstones, having a diameter spectrum ranging from 5 mm up to centimeters. Melting rate equations show that the smaller an ice particle is, the more effective it is in extracting heat from the environment during melting, due to the increased fraction of melted water per unit time. Based on this consideration and on the constant slope of the IC2M-LHN temperature profile opposed to the steeper IC1M-LHN's one, a conclusion could be drawn that the IC2M-LHN downdraft is composed primarily of large size hailstones. This

thesis is supported by the fact that larger hailstones have higher terminal fall speeds, which ultimately results in less time being available for heat exchange processes to cool the air temperature. In contrast, the IC1M-LHN profile shows substantial cooling of the air below the melting layer due to the melting of large amounts of graupel (small ice particles), which absorb greater heat from the surrounding atmosphere. A comparison with the pre-LHN simulations shows a reduction in temperature over the entire 0-4 km layer, due to absorption of latent heat of melting and vaporization by means of the precipitating processes and the cloud's blocking effect on the sun rays.

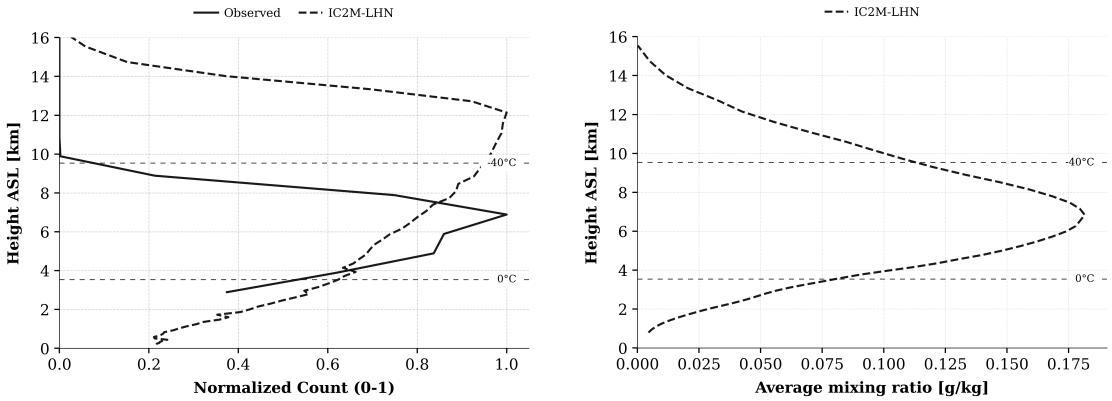

Figure 3.51: (left) Normalized vertical profiles (0-1 scale) of hailstones detections per layer within the supercell at 1300 UTC, excluding concentrations below $1 \cdot 10^{-5}$. (right) Vertical profiles of simulated hailstones mixing ratios averaged across the supercell domain at 1300 UTC.

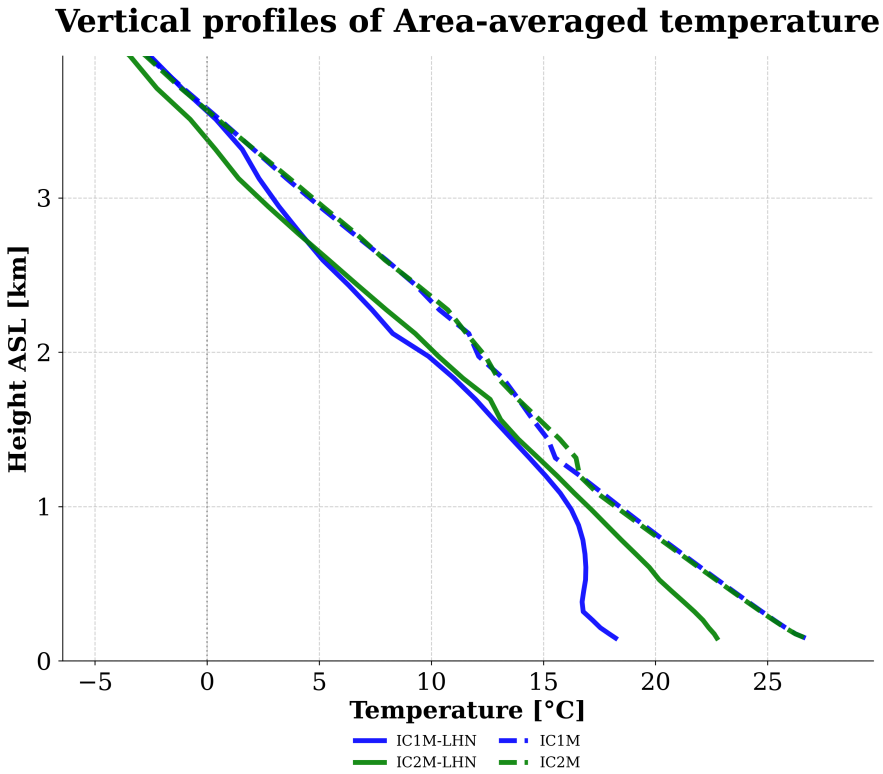

Figure 3.52: Vertical profiles of area-averaged temperature within the supercell region at 1300 UTC. Microphysics schemes compared: single-moment (blue), double-moment (green). Dashed lines represent baseline simulations while solid lines show LHN-assimilated runs

Chapter 4

Conclusions

Four forecasts were performed to test the high-resolution convection-permitting, limited-area version of the ICON model on a convective scenario over northern Italy on the 6th July, 2023. The definition of the four configurations involved the exploration of different microphysics parameterisation schemes, namely the single[21]- and double[24]- moment bulk schemes, as well as the impact of the LHN assimilation on the model output. The results were compared with weather radar observations,radiosoundings and ground weather station data. This was done firstly to evaluate the model's performance in forecasting thermodynamic and precipitation fields, and secondly to assess the accuracy of simulating microphysics processes occurring within the bi-phase, sheared, environment of a supercell thunderstorm.

The similarity of the vertical profiles of thermodynamic variables (air temperature and dew-point temperature) with radiosoundings products confirms the correct representation of the background atmospheric environment. But, in the absence of any type of data assimilation the model alone struggles to correctly predict the initiation of deep-convection phenomena

and, in particular, that of the supercell under investigation due to the small, mostly unresolved, scales at which these phenomena are triggered. This issue was addressed by applying the assimilation of instantaneous precipitation fields derived from the Italian radar composite using the LHN throughout the entire duration of the free forecast. This allows the correct forecast of the supercell and improvements are brought to the precipitation and reflectivity patterns across the simulation domain. This is confirmed by the correct localisation of the hailfall regions in the double-moment scheme. With this setup, both runs captured the distinguishing reflectivity-based features of supercells, including a well defined weak echo region, the embryo curtain and a high-reflectivity core. However, the features produced by the single-moment scheme are more similar to the observed ones. For example, IC1M-LHN run simulates a slightly higher 0-3 km SRH, resulting in a stronger mid-level mesocyclone rotation, which could be related to the presence of a more defined hook-echo signature. The IC2M-LHN run displaces the supercell to the north of its observed location. This displacement may be associated with a delay in the assimilation of latent heat data; this aspect should be investigated further to determine whether it is common behaviour or an inference drawn from this specific case. The echo top of 35 dBZ height, which marks the highest altitude of the 35 dBZ radar echo, serves as an indicator of updraft strength and thus reflects storm severity [45]. In both simulations and observations, this height reached approximately 14 km ASL, which further validates the accurate prediction of the thermodynamic environment and the realistic representation of microphysical processes within the updraft. However, the single-moment scheme produces maximum reflectivity values that are, on average, 10 dBZ lower than observed. This significant discrepancy

primarily arises from the absence of large scatterers, such as hailstones. In contrast, the double-moment scheme, which explicitly predicts hail, substantially improves the vertical structure of the high-reflectivity core. Near the melting layer, the difference with observations reduces to less than 5 dBZ, which is consistent with the scheme's ability to simulate large hailstones. Regarding the vertical distribution of hydrometeor mass, the double-moment scheme produces more graupel and snow particles, which actively contribute to hail growth through riming processes. In contrast, the single-moment scheme, results in most of the snow and graupel melting before reaching the surface, which increases the amopunt of rainwater. The ice-phase parameterizations of both schemes generate most of the ice crystals and graupel at higher elevations compared to observations. However, they correctly simulate the vertical distribution of snow and, in the double-moment scheme, hail, with production peaks that correlate well with observations from the supercell. This work focuses on a specific case study, therefore a more comprehensive analysis should be conducted using a larger dataset. Additionally, data assimilation has not been fully exploited. Where feasible, future efforts should focus on implementing the KENDA ensemble-based assimilation system. Sensitivity tests considering the influence of CCN concentration on cloud dynamics and the precipitation predicted by the double-moment scheme must be carried out understand the impact of the rapidly increasing concentration rates of atmospheric pollutants. Furthermore, future research should consider the integration of data deriving from distributed sensing systems within the PBL into existing NWP models. This synergistic approach could significantly advance our understanding of convective dynamics and address the limitations of current models in representing the effects of

subgrid-scale turbulence. Assimilating in-situ PBL measurements from mini-radiosonde clusters [46] into high-resolution NWP models could enhance severe weather prediction capabilities. Although computational constraints remain, such observational systems could be crucial for the next generation of high resolution NWP models, as they would provide valuable information on the state of the planetary boundary layer, which is crucial in triggering the convection process.

Bibliography

[1] P Gunturi and MK Tippett. «Managing severe thunderstorm risk: Impact of ENSO on US tornado and hail frequencies». In: *Willis Re Inc* (2017) (cit. on p. 1).

[2] RE Munich, Wolfgang Kron, and Andreas Schuck. *Topics geo: Natural catastrophes 2013: Analyses, assessments, positions*. Munchener Ruckversicherungs-Gesellschaft, 2014 (cit. on p. 1).

[3] Wuyin Lin, Minghua Zhang, and Jingbo Wu. «Simulation of low clouds from the CAM and the regional WRF with multiple nested resolutions». In: *Geophysical research letters* 36.8 (2009) (cit. on p. 2).

[4] J-I Yano. «Hot-tower hypothesis and mass-flux formulation». In: *Parameterization of Atmospheric Convection: Volume 1: Theoretical Background and Formulation*. World Scientific, 2016, pp. 175–193 (cit. on p. 2).

[5] Ronald B Stull. *Practical meteorology: an algebra-based survey of atmospheric science*. University of British Columbia, 2015 (cit. on pp. 11, 137).

[6] James R Holton and Gregory J Hakim. *An introduction to dynamic meteorology*. Vol. 88. Academic press, 2013 (cit. on p. 13).

[7] Stephan P Nelson. «The influence of storm flow structure on hail growth». In: *Journal of Atmospheric Sciences* 40.8 (1983), pp. 1965–1983 (cit. on p. 18).

[8] Keith A Browning and GB Foote. «Airflow and hail growth in supercell storms and some implications for hail suppression». In: *Quarterly Journal of the Royal Meteorological Society* 102.433 (1976), pp. 499–533 (cit. on p. 22).

[9] Shaomeng Li, Stanislaw Jaroszynski, Scott Pearse, Leigh Orf, and John Clyne. «VAPOR: A Visualization Package Tailored to Analyze Simulation Data in Earth System Science». In: *Atmosphere* 10.9 (2019). ISSN: 2073-4433. DOI: 10.3390/atmos10090488. URL: https://www.mdpi.com/2073-4433/10/9/488 (cit. on p. 22).

[10] Kenichi Matsuno. «Higher-order time-accurate scheme for unsteady, three-dimensional flows». In: *11th Computational Fluid Dynamics Conference*. 1993, p. 3362 (cit. on p. 26).

[11] R Ramos, A Aguilar, FM León Rodríguez, and O García. «EULER'S METHOD: AN APPROACH TO LEARNING AND DEVELOPMENT OF NUMERICAL MODELING». In: *EDULEARN12 Proceedings*. IATED. 2012, pp. 1670–1675 (cit. on p. 26).

[12] Lewis F Richardson. *Weather prediction by numerical process*. University Press, 1922 (cit. on p. 31).

[13] F Prill, D Reinert, D Rieger, and G Zängl. «ICON tutorial». In: *ICON* 1 (2022) (cit. on p. 32).

[14] Christoph Schraff, Hendrik Reich, Andreas Rhodin, Annika Schomburg, Klaus Stephan, Africa Perianez, and Roland Potthast. «Kilometre-scale ensemble data assimilation for the COSMO model

(KENDA)». In: *Quarterly Journal of the Royal Meteorological Society* 142.696 (2016), pp. 1453–1472.

[15] Klaus Stephan, S Klink, and C Schraff. «Assimilation of radar-derived rain rates into the convective-scale model COSMO-DE at DWD». In: *Quarterly Journal of the Royal Meteorological Society: A journal of the atmospheric sciences, applied meteorology and physical oceanography* 134.634 (2008), pp. 1315–1326 (cit. on p. 35).

[16] CD Jones and B Macpherson. «A latent heat nudging scheme for the assimilation of precipitation data into an operational mesoscale model». In: *Meteorological Applications: A journal of forecasting, practical applications, training techniques and modelling* 4.3 (1997), pp. 269–277 (cit. on p. 36).

[17] John S Marshall and W Mc K Palmer. «The distribution of raindrops with size». In: *Journal of Atmospheric Sciences* 5.4 (1948), pp. 165–166 (cit. on pp. 39, 73).

[18] Carlton W Ulbrich. «Natural variations in the analytical form of the raindrop size distribution». In: *Journal of climate and applied meteorology* (1983), pp. 1764–1775 (cit. on p. 39).

[19] Jacques Testud, Stéphane Oury, Robert A Black, Paul Amayenc, and Xiankang Dou. «The concept of "normalized" distribution to describe raindrop spectra: A tool for cloud physics and cloud remote sensing». In: *Journal of Applied Meteorology* 40.6 (2001), pp. 1118–1140 (cit. on p. 39).

[20] Anthony J Illingworth and T Mark Blackman. «The need to represent raindrop size spectra as normalized gamma distributions for the

interpretation of polarization radar observations». In: *Journal of Applied Meteorology* 41.3 (2002), pp. 286–297 (cit. on p. 39).

[21] Günther Doms et al. «A description of the nonhydrostatic regional COSMO model. Part II: Physical parameterization». In: *Deutscher Wetterdienst, Offenbach, Germany* (2011) (cit. on pp. 41, 166).

[22] Axel Seifert. «A revised cloud microphysical parameterization for COSMO-LME». In: *COSMO Newsletter* 7 (2008), pp. 25–28 (cit. on pp. 41, 46).

[23] Edwin Kessler. «On the distribution and continuity of water substance in atmospheric circulations». In: *On the distribution and continuity of water substance in atmospheric circulations*. Springer, 1969, pp. 1–84 (cit. on p. 42).

[24] A. Seifert and K. D. Beheng. «A two-moment cloud microphysics parameterization for mixed-phase clouds. Part 1: Model description». In: *Meteorology and atmospheric physics* 92 (Oct. 2006), pp. 45–66 (cit. on pp. 46, 55, 166).

[25] Michael P Meyers, Paul J DeMott, and William R Cotton. «New primary ice-nucleation parameterizations in an explicit cloud model». In: *Journal of Applied Meteorology and Climatology* 31.7 (1992), pp. 708–721 (cit. on p. 51).

[26] Andrew J Heymsfield and Masahiro Kajikawa. «An improved approach to calculating terminal velocities of plate-like crystals and graupel». In: *Journal of Atmospheric Sciences* 44.7 (1987), pp. 1088–1099 (cit. on p. 51).

[27] Günther Doms et al. *A description of the nonhydrostatic regional COSMO model. Part II: Physical parameterization*. Ed. by DWD Ulrich Schättler. Sixth. Frankfurter Straße 135 63067 Offenbach: Deutscher Wetterdienst Business Area "Research and Development", 2021 (cit. on p. 55).

[28] Eli J Mlawer, Steven J Taubman, Patrick D Brown, Michael J Iacono, and Shepard A Clough. «Radiative transfer for inhomogeneous atmospheres: RRTM, a validated correlated-k model for the longwave». In: *Journal of Geophysical Research: Atmospheres* 102.D14 (1997), pp. 16663–16682 (cit. on p. 55).

[29] Howard W Barker et al. «Assessing 1D atmospheric solar radiative transfer models: Interpretation and handling of unresolved clouds». In: *Journal of Climate* 16.16 (2003), pp. 2676–2699 (cit. on p. 55).

[30] MICHAEL Tiedtke. «A comprehensive mass flux scheme for cumulus parameterization in large-scale models». In: *Monthly weather review* 117.8 (1989), pp. 1779–1800 (cit. on p. 55).

[31] Richard L Thompson, Corey M Mead, and Roger Edwards. «Effective storm-relative helicity and bulk shear in supercell thunderstorm environments». In: *Weather and forecasting* 22.1 (2007), pp. 102–115 (cit. on p. 61).

[32] Kelvin K Droegemeier, Steven M Lazarus, and Robert Davies-Jones. «The influence of helicity on numerically simulated convective storms». In: *Monthly weather review* 121.7 (1993), pp. 2005–2029 (cit. on p. 63).

[33] Matthew J Bunkers, Matthew B Wilson, Matthew S Van Den Broeke, and Devon J Healey. «Scan-by-scan storm-motion deviations for

concurrent tornadic and nontornadic supercells». In: *Weather and Forecasting* 37.5 (2022), pp. 749–770 (cit. on p. 64).

[34] Richard L Thompson, Roger Edwards, and Corey M Mead. «An update to the supercell composite and significant tornado parameters». In: *Preprints, 22nd Conf. on Severe Local Storms, Hyannis, MA, Amer. Meteor. Soc. P*. Vol. 8. 2004 (cit. on p. 63).

[35] Alexander V. Ryzhkov and Dusan S. Zrnic. *Radar Polarimetry for Weather Observations*. First. Gewerbestrasse 11, 6330 Cham, Switzerland: Springer Cham, 2019 (cit. on p. 67).

[36] Nigel M Roberts and Humphrey W Lean. «Scale-selective verification of rainfall accumulations from high-resolution forecasts of convective events». In: *Monthly Weather Review* 136.1 (2008), pp. 78–97 (cit. on p. 75).

[37] Hongping Liu and V Chandrasekar. «Classification of hydrometeors based on polarimetric radar measurements: Development of fuzzy logic and neuro-fuzzy systems, and in situ verification». In: *Journal of Atmospheric and Oceanic Technology* 17.2 (2000), pp. 140–164 (cit. on pp. 80, 86).

[38] Paolo Davini, Renzo Bechini, Roberto Cremonini, and Claudio Cassardo. «Radar-based analysis of convective storms over northwestern Italy». In: *Atmosphere* 3.1 (2011), p. 33 (cit. on p. 81).

[39] Ulrich Blahak and Alberto de Lozar. «EMVORADO — Efficient Modular VOlume scan RADar Operator — A User's Guide —». In: (2020). URL: https://api.semanticscholar.org/CorpusID:221068406 (cit. on p. 83).

[40] Yuefei Zeng, Ulrich Blahak, and Dorit Jerger. «An efficient modular volume-scanning radar forward operator for NWP models: Description and coupling to the COSMO model». In: *Quarterly Journal of the Royal Meteorological Society* 142.701 (2016), pp. 3234–3256 (cit. on p. 83).

[41] D Rieger, M Milelli, D Boucouvala, F Gofa, A Iriza-Burca, P Khain, A Kirsanov, J Linkowska, and F Marcucci. «Verification of ICON in limited area mode at COSMO national meteorological services». In: *Reports on ICON* 6 (2021) (cit. on p. 127).

[42] Ulrich Blahak. «Towards a better representation of high density ice particles in a state-of-the-art two-moment bulk microphysical scheme». In: *Proc. 15th Int. Conf. Clouds and Precip., Cancun, Mexico*. Vol. 20208. 2008 (cit. on p. 155).

[43] Matthew P Bailey and John Hallett. «A comprehensive habit diagram for atmospheric ice crystals: Confirmation from the laboratory, AIRS II, and other field studies». In: *Journal of the Atmospheric Sciences* 66.9 (2009), pp. 2888–2899 (cit. on p. 157).

[44] Hans R Pruppacher, James D Klett, and Pao K Wang. *Microphysics of clouds and precipitation*. 1998 (cit. on p. 158).

[45] Tomeu Rigo and Carme Farnell Barqué. «Evaluation of the radar echo tops in Catalonia: Relationship with severe weather». In: *Remote Sensing* 14.24 (2022), p. 6265 (cit. on p. 167).

[46] Shahbozbek Abdunabiev, Chiara Musacchio, Andrea Merlone, Miryam Paredes, Eros Pasero, and Daniela Tordella. «Validation and traceability of miniaturized multi-parameter cluster radiosondes

used for atmospheric observations». In: *Measurement* 224 (2024), p. 113879 (cit. on p. 169).